Stony Brook University

Optoelectronics materials and heterostructures based on metamorphic grown InAsSb

A Dissertation Presented

by

Youxi Lin

to

The Graduate School

in Partial Fulfillment of the

Requirements

for the Degree of

Doctor of Philosophy

in

Electrical Engineering

Stony Brook University

May 2016

Stony Brook University

The Graduate School

Youxi Lin

We, the dissertation committee for the above candidate for the

Doctor of Philosophy degree, hereby recommend

acceptance of this dissertation.

Dmitri Donetski – Dissertation Advisor
Associate Professor, Department of Electrical and Computer Engineering

Gregory Belenky – Dissertation Advisor
Professor, Department of Electrical and Computer Engineering

Ridha Kamoua - Chairperson of Defense
Associate Professor, Department of Electrical and Computer Engineering

David Westerfel – Assistant Professor
Department of Electrical and Computer Engineering

David Hwang – Assistant Professor

Department of Mechanical Engineering

This dissertation is accepted by the Graduate School

Charles Taber
Dean of the Graduate School

Abstract

This work showed that InAsSb was one of the promising material systems for infrared applications in spectral region longer than 7 μm. InAsSb has the narrowest bandgap among group III-V bulk materials. Together with AlInAsSb and GaInSb, such Sb based alloys provide an interesting material system for fundamental research and optoelectronics applications.

The development of high quality InAsSb was based on the metamorphic growth on linearly compositionally graded buffer. The metamorphic growth allowed to characterize the properties of unrelaxed materials. Bandgap as narrow as 90 meV was demonstrated from InAsSb with 60% Sb composition at 77K, which was the narrowest bandgap ever reported for this material. Long lifetime and high hole mobility were also demonstrated in InAsSb with energy bandgap of 0.124 eV at 77K.

In order to suppress depletion region in p-n junction, the nBn heterostructures based on bulk InAsSb were designed and fabricated for long wavelength infrared (λ>7 μm) photo-detections. The background limited performance has been demonstrated in the devices operating at temperatures up to 100K.

Utilizing the virtual substrate technique, a new material system, the strain-balanced ultra-thin periodic structure $InAsSb_x/InAsSb_y$ was developed. It is free from the constraint of lattice constant in designing strain-balanced structures. Materials with short period demonstrated an optical bandgap as narrow as 0.06 eV at 20 K. Characterization showed that these materials preserve fundamental absorption and minority hole transport properties of bulk alloys challenged to achieve with alternative SLS material systems.

Table of contents

List of Figures

accomodated 1.4 % mismatch; (c) AlGaInSb with top Al, Ga and In contents of 75, 0 and 25 % - accomodated 1.4 % mismatch.

Figure 2.3. (a) Symmetric (004) RSM taken at the azimuth angle emphasizing the tilt in the epi-layers; (b) (004) RSM taken at the azimuth angle minimizing the tilt in the epi-layers; (c) dependence of the measured tilt angle as a function of the azimuth angle; (d) asymmetric (335) RSM taken at azimuth angle equal to 90˚. Solid line denotes the location of 335 reflexes corresponding to fully relaxed material with lattice parameter gradually increasing from that of GaSb. Dashed line denotes the location of 335 reflexes of the material with further increase of native lattice parameter but grown pseudomorphically to the top of fully relaxed section.

Figure 2.4. (a) The normalized PL spectra of bulk $InAs_{0.8}Sb_{0.2}$ and $InAs_{0.56}Sb_{0.44}$ alloys. (b) The normalized PL spectra of InAs and InSb epi-layers. The measurements were performed at T= 13 K with the excitation power of 100 mW.

Figure 2.5. The PL spectra of $InAs_{0.8}Sb_{0.2}$ alloys at T = 13 K measured with the excitation power levels of 20, 50 and 90 mW. The excitation area was $1.2x10^{-3}$ cm^{-2}. The shift of the energy maximum in the range of excitation power was below 2 meV.

Figure 2.6. Dependence of the energy gaps on Sb composition in the bulk InAsSb grown on AlInAsSb metamorphic buffers (blue symbols) and in Type-II InAsSb/InAs SLS grown on GaSb (red symbols). The data were obtained from PL maxima determined at T=13 K. The fit for the bulk InAsSb was obtained with the energy gap bowing parameter 0.87 eV.

Figure 2.7. The PL spectra of the bulk $InAs_{0.8}Sb_{0.2}$ (a) and $InAs_{0.56}Sb_{0.46}$ (b) at T=77 K (black lines) and fitting based on Eq 3 (blue lines). See the text for details on fitting.

Figure 2.8. The normalized PL spectra for InAsSb bulk with different Sb compositions at 77 K. (20% red line, 30% green line, 44% blue line, 55% black line); 2.9. The dependence of PL peak wavelength versus Sb composition for bulk InAsSb measured at T=77 K. The best fit was obtained with the bowing parameter of 0.87 eV.

Figure 2.9. The PL spectra of the bulk $InAs_{0.8}Sb_{0.2}$ (a) and $InAs_{0.54}Sb_{0.46}$ alloys(b) at T=13 K, 30 K, 77 K, and 150 K.. The excitation power was 100 mW.

Figure 2.10. The temperature dependence of the energy bandgaps. The fittings were obtained with the following Varshni parameters: Eg0= 0.226 eV, α=3.2 meV/K, b=100.4 K for $InAs_{0.8}Sb_{0.2}$ and Eg0= 0.119 eV, α=1.2 meV/K, b=33.3 K for $InAs_{0.56}Sb_{0.44}$.

Figure 2.11. The normalized PL spectra of type-II InAs/InAsSb SLS with Sb compositions of 22.5, 24.2, 25.1, 26.8 and 29.6 %, the PL spectrum of LWIR InAs/GaSb SLS from Ref. 20 is also shown. The measurements were performed at T= 13 K with the excitation power of 100 mW.

Figure2.12. PL spectra of $InAs_{0.77}5Sb_{0.225}$/InAs SLS (a) and $InAs_{0.704}Sb_{0.296}$/InAs SLS (b) under pulsed excitation with the pulse width of 100 ns, the repetition rate of 100 kHz, and the average power of 0.5 W.

Figure 2.13. The energy band profile of two-period InAs/$InAs_{0.775}Sb_{0.225}$. The black solid line represents the energy position of miniband. The black dot lines represent the energy position of heavy holes. The red lines represent the energy position of conduction band of freestanding $InAs_{0.775}Sb_{0.225}$. The red dot lines represent the energy position of valence band of freestanding $InAs_{0.775}Sb_{0.225}$. The energy position of the miniband was 12 meV above the conduction band of InAs. The energy position of heavy holes was 14 meV below the valence band of $InAs_{0.775}Sb_{0.225}$.

Figure 2.14. The PL spectra of Ga-free SLS at 13 K. (a) Undoped samples with Sb compositions of 23.5% with AlSb cap (blue line), and without AlSb cap (black line). The excitation power was 100 mW. (b) *p*-doped samples with Sb=24.6 % (green line) and 26.3 % (red line). The excitation power was 60 mW.

Figure 2.15. The time resolved photoluminescence (TRPL) spectra of Ga-free SLS at 13 K. Undoped samples with Sb compositions of 23.5% with AlSb cap (blue), and without AlSb cap, p-doped samples with Sb=24.6 % (green line) and 26.3 % (red line). The excitation energy per pulse was 15 nJ.

Figure 2.16. The dependences of TRPL peak intensity on the excess excitation carrier concentration at 77K for (a) the $p=6x10^{16}$ cm^{-3} structure, and (b) the $p=3x10^{17}$ cm^{-3} structure.

Figure 2.17. The optical modulation response (OMR) of InAs/InAsSb SLS. (a) Undoped samples with Sb composition of 23.5 % with AlSb barriers (blue line), without AlSb barriers (black line), and p-doped samples with 26.3% Sb (red line), and 24.6% Sb (green line), respectively. The excitation power density was 1.6 W/cm^2. (b) The OMR of InAs/InAsSb SLS with Sb composition of 26.3% at different excitation levels (black lines). The red lines show the theoretical response of the low-pass filter of the 1st order. The excitation power densities were 0.7, 0.9, 1.6 W/cm^2. (c) The dependence of the PL response time constant on carrier excitation rate.

Figure 2.18. (a) The OMR data for the Ga-free SLS with Sb composition of 23.5%, and without a AlSb barrier at different excitation levels (black lines). The red lines show the fit with the response of the 1st order low-pass filter. (b) The dependence

of the PL response time constant on carrier excitation rate. The excitation power densities were 0.02, 0.04, 0.08, 0.09, 0.19, 0.27, 0.53, 0.54, 0.75, 1.05, 1.6, 2.2 W/cm^2.

Figure 2.19. (a) The OMR data for InAs/InAsSb SLs with Sb composition of 23.5%, with AlSb cap at different excitation levels (black lines). The red lines show the fit with the response of the 1st order low-pass filter. (b) The dependence of the PL response time constant on carrier excitation rate. The excitation power densities were 0.02, 0.04, 0.14, 0.27, 0.38, 0.75, 1.6, 2.2, 2.8, 3.5, 6.8 W/cm^2.

Figure 3.1. The schematic band-diagram of nBn heterostructures. The conduction band is plotted in red, and valance band is plotted in blue. The flat band condition is shown by solid line, and the condition without bias is shown by dash line.

Figure 3.2 (a) The schematic band diagram for the heterostructure with a bulk InAsSb absorber with 44 % Sb composition. The AlInSb barrier was lattice-matched to the InAsSb absorber layer. The top contact layer was doped with Tellurium to a level of $n=1\times10^{18}$ cm^{-3}. (b) The schematic cross-section of the processed heterostructures for LWIR detector with top illumination.

Figure 3.3. The spectra of external quantum efficiency obtained for the heterostructures with a 1-µm-thick InAsSb layers with Sb composition of 40 % at the temperatures of 77 K, 100 K, 120 K, and 150 K, respectively. (b). The IV characteristics obtained for heterostructures with a 1-µm-thick InAsSb layers with Sb composition of 40 % at different temperatures ranging from 80 K to 200 K.

Figure 3.4. The spectra of external quantum efficiency obtained for the heterostructures of $InAsSb_{0.5}$ layers at 77 K with different active layer thickness. 1 µm (blue line), 2 µm (red line), 3 µm (green line).

Figure 3.5. (a) Dependences of the integrated QE on bias voltage for the nBn photodetectors with undoped and doped $InAsSb_{0.4}$ absorbers at T = 77 K; (b) The QE spectra for the nBn photodetectors with undoped absorber at T = 77 K and 150 K (solid and dotted lines, respectively) and for one with doped absorber at T = 77 K (dashed line). The spectra were measured at the bias voltage of - 0.4V.

Figure 3.6. The current-voltage characteristics of the nBn devices with undoped (a) and doped (b) $InAsSb_{0.4}$ absorbers at different temperatures. (c) The temperature dependences of the dark current densities taken at a bias voltage of -0.4 V and -0.5 V for undoped and doped devices respectively.

Figure 3.7. The specific detectivity spectra of the barrier detectors with 1-µm-thick InAsSb0.4 absorbers at T = 77 K Solid and dashed lines correspond to the devices

with doped and undoped absorbers, respectively. The dotted line shows the 300 K background limit in a 2π acceptance angle.

Figure 3.8. The specific detectivity spectra of n=1e16 cm^{-3} doped structure at different temperatures, and the comparison with the background limited performance (blue dotted line).

Figure 3.9. (a) The schematic presentation of the structure epi-side illuminated detectors. (b) The schematic presentation of the back-side illuminated detectors structure. DW and DM are the optical window and contact sizes, respectively. 1- top metal contact, 2- mesa contact layer, 3- barrier, 4- absorber, 5- substrate, 6- backside metal contact.

Figure 3.10. (a) The transient responses of the devices with different contact sizes (50x50, 200x200, and 500x500 μm^2) at T= 77 K at the bias voltage -0.4 V. F and S denote the fast and slow components of the response amplitude caused by vertical and lateral transport of by minority holes respectively. (b) The dependences of the amplitudes of the fast and slow components of the response on contact size DM.

Figure 3.11. The transient responses for the devices with the contact sizes of DM= 50 and 200 um.

Figure 3.12. The photoresponse of samples with different doping, undoped (black), $1x10^{16}$ cm-3(green), $2x10^{16}$ cm^{-3} (blue) and $4x10^{16}$ cm^{-3} (red), respectively.

Figure 3.13. (a). Dark current density-voltage characteristics measured at 77 K for samples with different doping, undoped (black), $1x10^{16}$ cm^{-3}(green), $2x10^{16}$ cm^{-3} (blue) and $4x10^{16}$ cm^{-3} (red), respectively. (b). The temperature dependence of dark current density at different bias for samples with different doping. Red dot undoped at -0.4 V, blue dot $1x10^{16}$ cm^{-3} at -0.4 V, and green dot $4x10^{16}$ cm^{-3} at -0.4 V, respectively. Red solid undoped at -0.5 V, blue solid $1x10^{16}$ cm^{-3} at -0.5 V, and green solid $4x10^{16}$ cm^{-3} at -0.5 V, respectively.

Figure 3.14. (a). Transient response of samples with different doping, $1x10^{16}$ cm^{-3}(red), $2x10^{16}$ cm^{-3} (yellow) and $4x10^{16}$ cm^{-3} (green). (b). Dependence of recombination rate on doping levels from experimental result (dot), dash line represents a linear dependence on carrier concentration. (c). Dependence of dark current density on doping levels from experimental result (black dot), and calculation of diffusion limited dark current from experimental lifetime (green dot).

Figure 3.15. The frequency response of 100 um^2 mesa (solid line). And the approximation of 1^{st} order low pass filter equation (dot line).

Acknowledgements

I would like to thank many people for their support in accomplishing my Ph.D. study.

I wish to express my deepest appreciation to my advisors, Prof. Gregory Belenky and Prof. Dmitry Donetsky. Thank you very much for your patient guidance. I really appreciate being trained and shaped under supervision of you in the most important time of my life.

I also would like to show my sincere appreciation to Prof. Leon Shterengas, Prof. Sergey Suchalkin, Dr. Gela Kipshidze, Dr. Stefan Svensson, and Dr. Wendy Sarney for their insightful suggestions and fruitful discussions.

I feel honored and pleasure to work with all the past and present members of Optoelectronics group for the past six years. Among them, I should thank to Dr. Takashi Hosoda especially. Thank you for the patience on my stubbornness when I joined in the group. And also thank you for all the help in those "seem-trivial" things. It means a lot to me and I really appreciate it.

The most important thanks goes to my family. Especially my wife, Shu Chen, it is you who accompany me for the six-years Ph.D. study abroad. It is also you who give me unconditional support and love to accomplish my work.

Publications

1. G. Belenky, **Y. Lin**, L. Shterengas, D. Donetsky, G. Kipshidze, S. Suchalkin, "Lattice parameter engineering for III-V long wave infrared photonics", Electron. Lett., 51, 1521 (2015).
2. **Y. Lin**, S. Suchalkin, G. Kipshidze, T. Hosoda, B. Laikhtman, D. Westerfeld, L. Shterengas, G. Belenky, "Effect of hole transport on performance of infrared type-II superlattice light emitting diodes", J. Appl. Phys., 117, 165701 (2015).
3. **Y. Lin**, D. Donetsky, D. Wang, D. Westerfeld, G. Kipshidze, L. Shterengas, W. L Sarney, S. P Svensson, G. Belenky, "Development of Bulk InAsSb Alloys and Barrier Heterostructures for Long-Wave Infrared Detectors", J. Electron. Mater., 44, 3360 (2015).
4. S. P. Svensson, F. J. Crowne, H. S. Hier, W. L. Sarney, W A. Beck, **Y. Lin**, D. Donetsky, S. Suchalkin and G. Belenky, "Background and interface electron populations in InAs0.58Sb0.42", Semicond. Sci. Technol, 30, 035018 (2015).
5. W.L. Sarney, S.P. Svensson, D. Wang, D. Donetsky, G. Kipshidze, L. Shterengas, **Y. Lin**, G. Belenky "AlInAsSb for M- LWIR detectors", J. Cryst. Growth, 425, 357 (2015).
6. **Y. Lin**, D. Wang, D. Donetsky, G. Kipshidze, L. Shterengas, G. Belenky, W. L. Sarney, S. P. Svensson, "Structural and Optical Characteristics of Metamorphic Bulk InAsSb," Int. J. High Speed Electron. Syst., 23, 1450021 (2014).
7. **Y. Lin**, D. Wang, D. Donetsky, G. Kipshidze, L. Shterengas, L. E. Vorobjev, G. Belenky, "Transport properties of holes in bulk InAsSb and performance of barrier long-wavelength infrared detectors," Semicond. Sci. Technol., 29, 112002 (2014).
8. **Y. Lin**, D. Wang, D. Donetsky, G. Belenky, H. Hier, W. L. Sarney, S. P. Svensson, "Minority Carrier Lifetime in Beryllium- Doped InAs/InAsSb Strained Layer Superlattices," J. Eletron. Mater., 43, 3184 (2014).
9. **Y. Lin**, D. Wang, D. Donetsky, L. Shterengas, G. Kipshidze, G. Belenky, S. P. Svensson, W. L. Sarney, H. S. Hier, "Conduction-and Valence-Band Energies in Bulk $InAs_{1-x}Sb_x$ and Type II $InAs_{1-x}Sb_x$/InAs Strained-Layer Superlattices," J. Electron. Mater., 42, 918 (2013).
10. D. Wang, D. Donetsky, G. Kipshidze, **Y. Lin**, L. Shterengas, G. Belenky, W. Sarney, S. P. Svensson, "Metamorphic InAsSb- based barrier photodetectors

for the long wave infrared region," Appl. Phys. Lett., 103, 051120 (2013).

11. G. Belenky, D. Wang, **Y. Lin**, D. Donetsky, G. Kipshidze, L. Shterengas, D. Westerfeld, W. L. Sarney, S. P. Svensson, "Metamorphic InAsSb/AlInAsSb heterostructures for optoelectronic applications," Appl. Phys. Lett., 102, 111108 (2013).

12. S. P. Svensson, W. L. Sarny, H. Hier, **Y. Lin**, D. Wang, D. Donetsky, L. Shterengas, G. Kipshidze, G. Belenky, "Band gap of $InAs_{1-x}Sb_x$ with native lattice constant," Phys. Rev. B, 86, 245205 (2012).

13. D. Wang, D. Donetsky, **Y. Lin**, G. Kipshidze, L. Shterengas, G. Belenky, W. L. Sarney, S. P. Svensson, "InAs1-xSbx alloys with native lattice parameters grown on compositionally graded buffers: structural and optical properties," Int. J. High Speed Electron. Syst., 21, 1250013 (2012).

Introduction

Infrared is invisible electromagnetic (EM) radiation with wavelength longer than those of visible light. It ranges from red edge of visible light (700 nm) to 1 mm. The infrared region is not as transparent as visible region on Earth. Due to existence of different types of molecules in atmosphere, EM waves are significantly absorbed by vibration of molecules, such as H_2O, CO_2, O_3. Given the transparency windows infrared spectrum is divided into several sub-regions, they are near infrared (0.7-2 μm), mid-wavelength infrared (MWIR) (2-5 μm), long-wavelength infrared (LWIR) (7-14 μm), and very long-wavelength infrared (VLWIR) (>14 μm), as shown in Figure 1.1. Meanwhile, thermal radiation spectrum of object at room temperature spans both MWIR and LWIR regions, making these regions unique from others. As consequences, optoelectronic devices operating in MWIR and LWIR region are of great interest for various applications, such as gas sensing, thermal imaging, space communication for civilian and military needs.

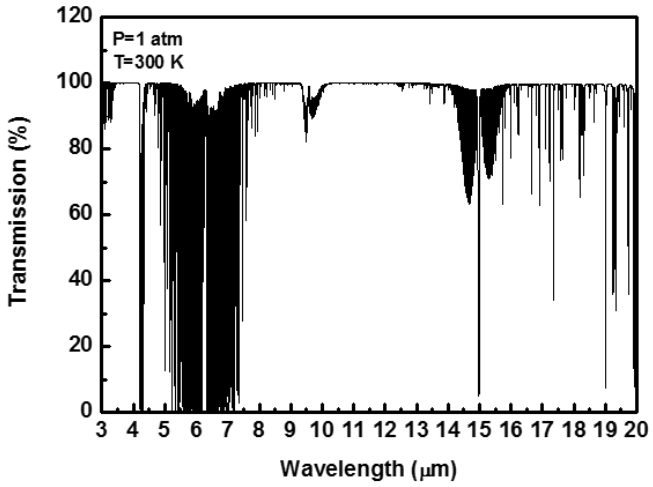

Figure 1.1. The transmission spectrum of atmosphere in the wavelength range of 3 to 20 μm. The spectra was calculated wit HITRAN data. The thickness of air was 1m. The molecules for spectrum calculation were H_2O, CO_2 and O_3 with volume mixture ratio of 1%, 0.025%, and 0.01%, respectively. [3]

Considering of high efficiency, low power consumption, stability, low cost, and compactness, semiconductor based devices stand out among others in optoelectronics design. The last decade has seen significant improvement of molecule beam epitaxy (MBE) growth technology, as a consequence, research on semiconductor materials with optical bandgap in both MWIR and LWIR regions attract increasing attention. Among various groups of semiconductors, III-V alloys cover a bandgap spectrum ranging from 0.235 eV (InSb) to more than 6 eV (AlN). Using bandgap engineering, heterostructures with quantum wells (QWs), strain balanced suplattices (SLs) based on III-V materials have demonstrated the ability to extend energy bandgaps and wavelengths to LWIR region, respectively [1, 2].

This work focuses on the development of heterostructures with InAsSb, the narrow bandgap ternary alloys. The selected topics on semiconductor background are introduced in Chapter 1, including properties of III-V materials, and material systems used for LIWR photo-detection. The optical properties are discussed in Chapter 2. The InAsSb based heterostructures for LWIR applications (photodetector) is presented in Chapter 3. Chapter 4 focuses on the work extending InAsSb based material to very long wavelength region. The summary of most important results is discussed in Chapter 5. In appendix, the relevant optical measurements used in this work are introduced.

Chapter 1

Properties of III-V semiconductors compounds

1.1 Structural properties

In a crystal, the atoms are arranged in a periodic manner. The Bravais lattices are the distinct lattice types, which can fill the whole space when they are repeated periodically. The lattice can therefore be generated by three unit vectors $\overrightarrow{a_1}$, $\overrightarrow{a_2}$, $\overrightarrow{a_3}$, and a set of integers k, l and m so that each lattice point, identified by a vector , can be obtained from:

$$\vec{r} = k\overrightarrow{a_1} + l\overrightarrow{a_2} + m\overrightarrow{a_3}\,, \tag{1.1}$$

There are two types of closed-packed structures in group III-V materials. One is zinc-blend structure as shown in Figure 1.2, the other is wurzite structure. Since the wurzite structure mainly exists in Nitride based semiconductors, which are wide bandgap materials, it is outside the discussion of this work. The zinc-blend structure resembles diamond structure, which consists of two interpenetrating face-center cubic, shift along body diagonal direction by quarter length of diagonal. The difference from diamond structure is that the FCC structures are occupied by alternating group III atoms and group V atoms. (Figure 1.2). As mentioned above, the FCC structure is one type of Braivis lattices, whose lattice could be expressed by Eq. 1.1. The smallest unit cell that contains only one lattice is called primitive cell. A primitive cell is built on the Braivis lattice, such that every lattice vector can be obtained from the unit vectors. However, for zinc-blende structures, there are two atoms in primitive cell, the cation and the anion, respectively.

In terms of crystallography, zinc-blende structure is generally described by cubic unit cell, with unit vectors shown in Figure 1.2. The length of the unit vector is defined as lattice constant, which is an important parameter for materials. For group III-V semiconductors, usually the lattice constant increases with elements numbers, ranging from GaP (5.45 A) to InSb (6.47 A).

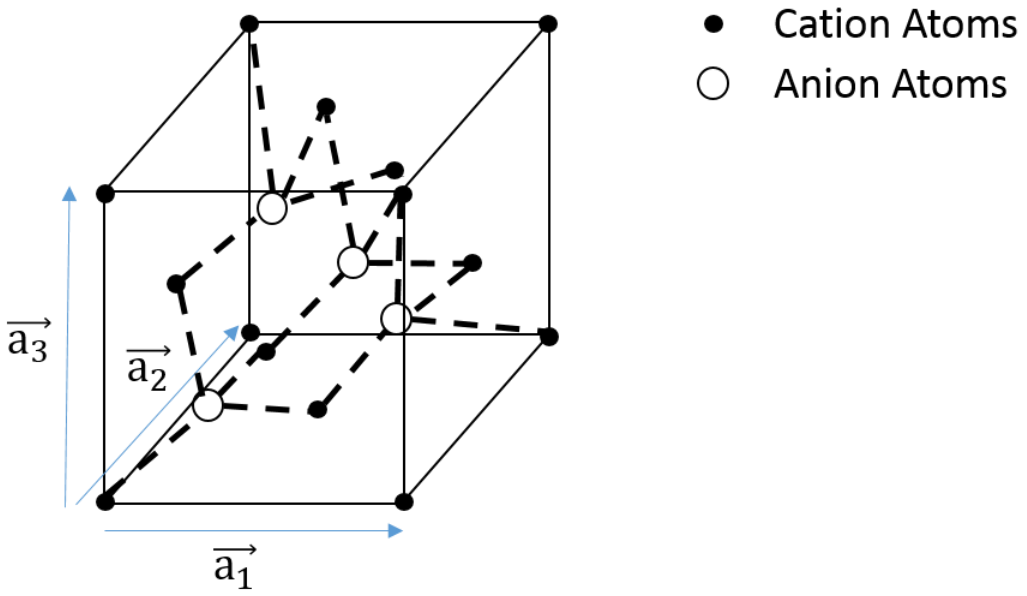

Figure 1.2. Zinc-Blende cubic unit cell. solid circles represent Cation Atoms, and hollow circles represent Anion Atoms.

The lattice constant of group III-V compound is usually defined by linear interpolation of binary materials. For Example, the lattice constant $InAs_xSb_{1-x}$ could be expressed as:

$$\mathrm{a(InAsSb)} = a(InAs)x + a(InSb)(1-x)\,, \qquad (1.2)$$

For modern semiconductor technology, most of epitaxial structures are based on growth on commercially available substrates. It means that the lattice constant of epitaxial layer should be very close to that of substrate, otherwise, materials quality will be deteriorated by dislocation, or even cracks due to strain relaxation [4]. As a

result, the lattice constants of epilayers becomes limited factor for a designer. In Chapter 2, the challenge will be discussed in details, and the way it was overcome.

Due to the long-term periodic property of crystal lattice, it is also very important to study its Fourier transform terms, the reciprocal space. Reciprocal space is important and useful in the x-ray based crystallography, and electronic energy band structures of materials. The reciprocal lattice is the Fourier transform of the real space, or direct space. It is represented by set of lattice vectors $\vec{K}$, which satisfied the condition expressed as follow:

$$\exp\left(\mathrm{i}\vec{K} * \vec{R}\right) = 1, \tag{1.3}$$

where $\vec{R}$ is lattice vector in real space. If $\vec{K}$ is expressed by the unit vectors in reciprocal space as:

$$\vec{K} = k\overrightarrow{b_1} + l\overrightarrow{b_2} + m\overrightarrow{b_3}, \tag{1.4}$$

where k, l, and m are integers. Unit vectors in reciprocal space could be expressed as:

$$\begin{aligned}
\overrightarrow{b_1} &= 2\pi \frac{\overrightarrow{a_2} \times \overrightarrow{a_3}}{\overrightarrow{a_1} * (\overrightarrow{a_2} \times \overrightarrow{a_3})} \\
\overrightarrow{b_2} &= 2\pi \frac{\overrightarrow{a_3} \times \overrightarrow{a_1}}{\overrightarrow{a_2} * (\overrightarrow{a_3} \times \overrightarrow{a_1})} \\
\overrightarrow{b_3} &= 2\pi \frac{\overrightarrow{a_1} \times \overrightarrow{a_2}}{\overrightarrow{a_3} * (\overrightarrow{a_1} \times \overrightarrow{a_2})}
\end{aligned} \tag{1.5}$$

From Eq. (1.5), the reciprocal lattice could be constructed by direct lattice. Figure 1.3 (a) shows a reciprocal unit cell of FCC, which is a BCC (body-centered cubic) structure. Correspondingly, a reciprocal unit cell of BCC is FCC. In terms of

primitive cell, there is a special way to determine the primitive cell in reciprocal space. The primitive cell is formed by sets of planes perpendicular bisected the nearest lattice. As shown in Figure 1.3 (b), the central square is a primitive cell of the reciprocal lattice, it is also called first Brillouin Zone. First Brillouin zone is of importance in solid state physics, due to the fact that all the reciprocal space outside could be expressed by vectors inside the zone and reciprocal lattice.

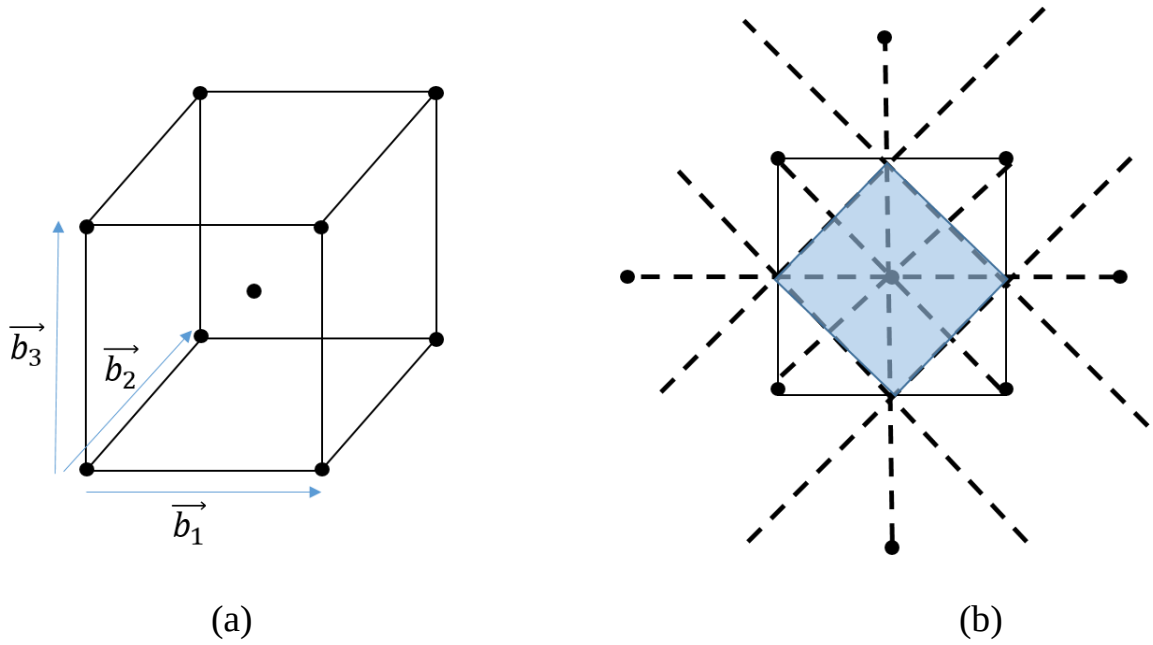

Figure 1.3. (a), The unit cell of a body center structure in Reciprocal Space. (b), Constructions of the Brillouin Zone in Reciprocal Space in 2D case. The blue region represents the first Brillouin Zone.

On the other hand, according the Eq. (1.5), the length of reciprocal lattice with index (k, l, m) is actually equal to 2π divided by the space between two parallel (k, l, m) plane. Therefore, another important function of reciprocal lattice in crystallography is to characterize the corresponding planes in direct space. For such a reason, the 2π is sometimes omitted for definition of reciprocal lattice in Eq. (1.5) for crystallography.

1.2 Electronic band structure of group III-V semiconductors

The property that distinguished semiconductors from other materials concerns the behavior of electrons in the existence of energy gaps in electronic excitation spectra. The microscopic behavior of electrons is specified in terms of electronic band structure. The properties of electrons in a solid containing 10^{23} atoms/cm^3 is very complicated. A detailed study of band structures of group III-V semiconductors could be found elsewhere [5-7], while the basic properties are introduced in this section.

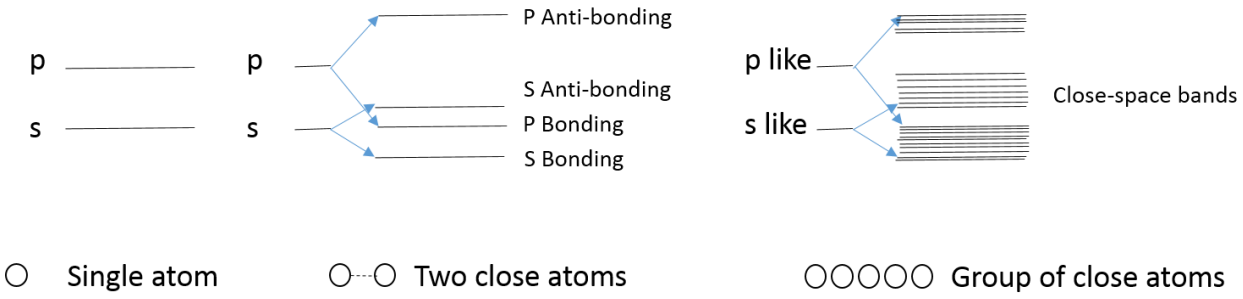

Figure 1.4. The schematic picture to show the construction of energy bands from single levels of atoms

As discussed above, semiconductors are comprised of atoms in periodic structures. The distance between atoms is in level of Angstrom. Electrons in the outer shell of an isolated atom are known to have discrete energy levels (s, p, d, etc.). When two atoms come close, the electrons in the outer shell start to interact with others in neighboring atoms, splitting energy levels due to Pauli exclusion law. Eventually, discrete energy levels with number in the order of 10^{23} generate series of energy bands. Figure 1.4 depicts this process schematically, where energy levels evolve gradually from discrete level to energy bands. Electrons are piled up from low energy to high energy according to Pauli exclusion law. At T=0 K, the top most energy level is defined as Fermi energy of a system. The energy difference between

the filled and empty band is called energy band gap. For group III-V semiconductors, there are two atoms per unit cell, corresponding to 8 valance electrons in outer shell. In such case, 8 electrons will just fill up the band 2 in symmetric s-like band, 6 in symmetric p-like degenerate bands, while there is no electron in higher energy band. In terms of semiconductor, the band that is filled by electrons are called valence band, the one that is empty at 0K is called conduction band. The energy bandgap between conduction and valance band depends on chemical bonding between anion and cation atoms. Since the bonding energy depends on the distance between these two atoms, in general, group III-V materials with larger lattice constant have a smaller bandgap. Figure 1.5 shows the relationship between bandgap energies and lattice constants of group III-V binary materials, except for III-nitrides. It shows that among group III-V binary materials, InSb has the narrowest bandgap with the largest lattice constant.

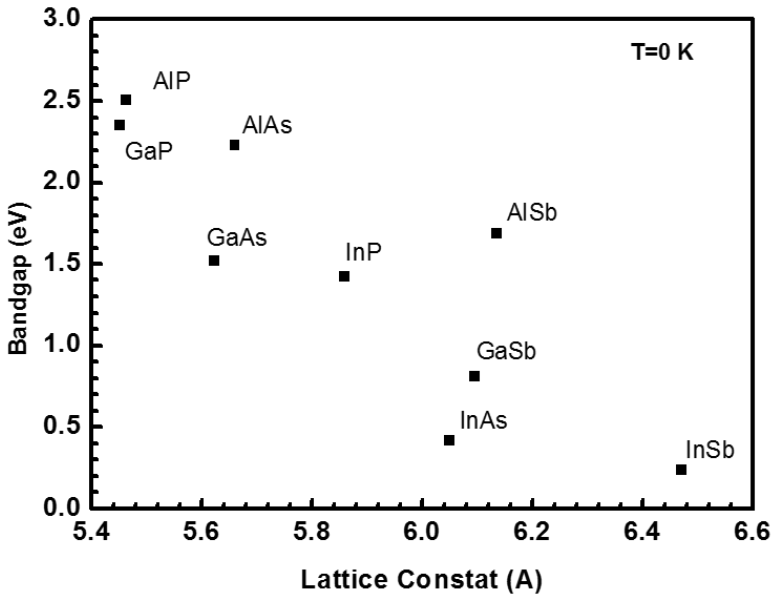

Figure 1.5. The energy bandgaps vs. lattice constant relation of III-V semiconductors alloys at T=0 K.

1.3 The effective mass of group III-V semiconductors

As discussed above, semiconductors are comprised of periodic arrangement of atoms. The electrons in such crystals experience a periodic potential energies. In a simplified one-electron model, the Schrodinger's equation could be expressed as:

$$\left(-\frac{\hbar^2}{m}\nabla^2 + \mathrm{V}(\vec{r})\right)\Phi = \mathrm{E}\Phi \ , \tag{1.6}$$

where the $\mathrm{V}(\vec{r})$ is the periodic potential energy, which satisfies the condition as follow:

$$\mathrm{V}(\vec{r}) = \mathrm{V}\left(\vec{r} + \vec{R}\right) , \tag{1.7}$$

According to periodic condition, the electron wavefunction in crystal could be expressed by Bloch function: [8]:

$$\Phi_{\vec{k}}(\vec{r}) = \exp\left(\mathrm{i}\vec{k}\vec{r}\right) u_{n\vec{k}}(\vec{r}) \ , \tag{1.8}$$

where $\vec{k}$ is the wave-vector in the reciprocal space. Since the wavefunction also satisfies the periodic condition. The wave-vector k_i (i=x,y,z) should be satisfied by the condition:

$$k_i = \frac{2\pi}{a}\frac{n}{N_i} \qquad with\ n = 1, 2, 3, \ldots\ldots, N_i - 1 \ , \tag{1.9}$$

where a is the lattice constant, and N_i is the number of lattices in i^{th} direction. Meanwhile $\mathrm{u}(\vec{r})$ also meets the periodic condition. The proof of Bloch function could be found elsewhere [8]. Bloch function is the basis of the solid state physics. It depicts the behavior of carriers in solids. According to Eq. (1.8), the exponential term shows that the electrons could move in the periodic structure, with wave amplitude equal to u(r) affected by the periodic potential energy. Since the wavefunction is periodic in direct space, it is also periodic in reciprocal space as well.

It implies that it is enough to use wave vectors in the first Brillouin zone to express wavefunction. Any wave function with wave vectors larger than $\frac{2\pi}{a}$ could be transferred to first Brillouin zone. Another application of Bloch function is to calculation of bandstructure of materials. The Bloch function at the band edge is sometimes approximated as: By substituting Eq. (9) into Eq. (5), we have:

$$\mathrm{H}(\vec{k}) = \mathrm{H} + H_{\vec{k}\vec{p}}$$

$$H_{\vec{k}\vec{p}} = \frac{\hbar}{m}\vec{k} * \vec{\pi}$$

$$\vec{\pi} = \vec{p} + \frac{\hbar}{4mc^2}(\vec{\sigma} \times \nabla V) \qquad (1.10)$$

$$\mathrm{E}(\vec{k}) = E_n(\vec{k}) - \frac{\hbar^2 k^2}{2m}$$

If the states $\mathrm{u}(\vec{r})$ form a complete set of periodic functions, a representations of H in this basis is exact (Liouville-Sturm theorem). So that diagonalization of the infinite matrix could lead to the dispersion relation throughout the whole Brillouin zone. It is almost impossible to calculate the cellular function with number of basis function equal to the level of 10^{23}. However, it is lucky that most of phenomena in semiconductors are only related with the behavior at the band edge, where k is small.

In this case, the term $\mathrm{H_{kp}}$ is much smaller than the Hamiltonian that is attributed to original atoms. Therefore, by applying nondegenerate perturbation theory to Eq. (1.10) for an isolated band, one can find solutions for smaller values of k around k=0 to second order as:

$$E_n(\vec{k}) = E_n(0) + \frac{\hbar^2 k^2}{2m} + \frac{\hbar^2}{m^2}\sum_l \frac{|<n0|\pi|l0>*k|^2}{E_n(0) - E_l(0)} \ , \qquad (1.11)$$

The first order term is zero due to the symmetric property of the crystal. Eq.(1.11) shows that bandstructure dispersion around k=0 could be approximated with finite matrix element between levels in isolated atoms. The method to estimate the band structure is also called kp method. Figure 1.6 shows the bandstructure dispersion of InAs calculated by kp method with 8x8 Hamiltonian.

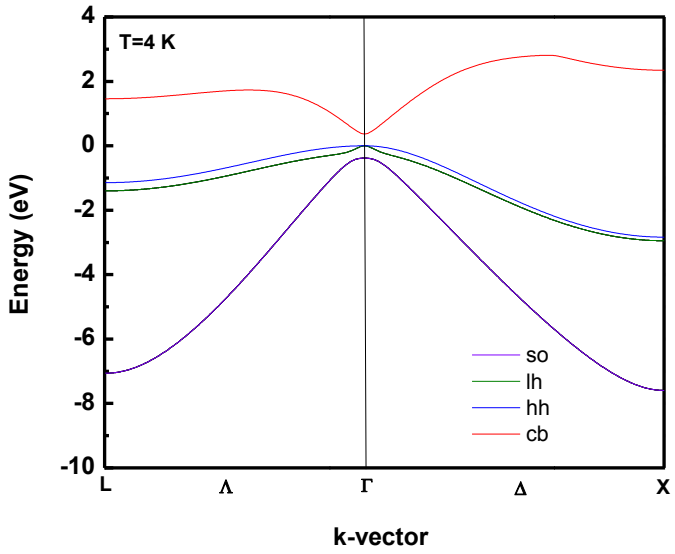

Figure 1.6. The band structure of InAs along two symmetric directions at T=4 K calculated using nextnano. [9]

If one treats behavior of carrier around the band edge as "almost-free" electrons, which could be described as:

$$E_n(\vec{k}) = E_n(0) + \frac{\hbar^2}{2m^*}k^2 \,, \tag{1.12}$$

where m^* is defined as effective mass of carriers. By equating Eq.(11) and Eq.(12), one can reach the important conclusion of effective mass as:

$$(\frac{1}{m^*})_{ij} = \frac{1}{m_0}\delta_{ij} + \frac{2}{m^2}\sum_l \frac{\pi^i_{nl}\pi^j_{nl}}{E_n(0)-E_l(0)} \,, \tag{1.13}$$

Eq.(1.13) shows the anisotropy of effective mass along different directions in reciprocal space. There are some qualitative analysis which are addressed here. First of all the matrix element π_{nl} depends on the symmetric properties of crystals described by the group theory. According to selection rules, there are only very limited numbers of matrix elements have non-zero values. Secondly, for valence band, Eq. (1.13) implies that contribution of effective mass from higher energy level band lead to a negative number. In such case, the effective mass of electrons in valance band is negative, and usually it is artificially described by another type of carriers, holes with possible charge and positive effective mass. Since the energy difference appears in denominator in Eq. (1.13), there is very little contribution to low lying energy band from very high energy band. As a consequences, for some group III-V materials with narrow bandgap (InAs, InSb), it is adequate to consider the effective mass of valance band only from conduction band, and vice versa (Kane model).[6]. For example, according to Eq. (1.13), the effective mass of electrons in conduction band could be further approximated as:

$$\frac{1}{m_e} = \frac{1}{m_0} + \frac{2}{m_0^2}\frac{|<S|p_x|X>|^2}{E_g} \equiv \frac{1}{m_0} + \frac{2}{m_0^2}\frac{P^2}{E_g}, \qquad (1.14)$$

where X is the one of representatives in valance band, S is that in conduction band. Eq. (1.14) implies that in narrow band gap materials, the smaller the bandgap, the smaller the effective mass. More important, the matrix element P and energy bandgap Eg could be determined from experiment (photoluminescence, absorption measurement).Therefore, based on kp method, the effective mass and band structure near the band edge, could be estimated accurately from the optical experiment. There are many other methods to calculate bandstructures of materials, such as tight-binding approach, pseudopotential method. [10-11].

For compound semiconductors, the calculation of bandstructure is very complicated. Usually, the potential energy of compound material is linearly interpolated by potential of binary materials, and the eigenvalue of compound at the band edge would be calculated. Eventually the bandstructure is approximated. However, there is an empirical way to estimate bandgap energy from binary materials. The energy bandgap of compound, i.e. $InAs_{1-x}Sb_x$, could be expressed to the second order of polynomial approximation:

$$E_g = (1-x)E_g(InAs) + xE_g(InSb) - Cx(1-x)\ , \qquad (1.15)$$

where C is called bowing parameter. By measuring the bandgap of ternary materials with different Sb compostion at low temperature, the bowing parameter could be obtained.

To sum up, energy bands are formed in solids due to closely packed atoms. The bandstructure of group III-V semiconductors are closely related to its crystal structures and chemical elements. As discussed above, the bandstructure of narrow bandgap group III-V materials could be approximated by Kane model. Based on sophisticated band engineering, group III-V semiconductors could be designed and used for long wavelength infrared (LWIR) photo-detection. In the next section, the material system for LWIR absorption will be introduced and discussed.

1.4 Absorption in semiconductors

The fundamental energy gaps of group III-V semiconductors span the energy range from 0.1 eV to about 4 eV. Photons of sufficient energy can excite electrons from the filled valence bands to the empty conduction bands. As a consequence, photons will be partially absorbed upon passing through a thin semiconductor film, if photon energy is larger than the bandgap. In the rest of this section, a semi-classical

approach will be used to describe the interaction between an external EM field and Bloch electrons inside a semiconductor.

The unperturbed one-electron Hamiltonian is shown in previous section in Eq. (1.5). To describe the EM fields, a vector potential $\vec{A}(\vec{r},t)$ and a scalar potential $\Phi(\vec{r},t)$ are used. In this specific case, the Coulomb gauge is chosen, in which

$$\Phi = 0 \text{ and } \nabla * \vec{A} = 0 \,, \tag{1.16}$$

In such case, electric field and magnetic fields are given by

$$\vec{E} = -\frac{1}{c}\frac{\partial \vec{A}}{\partial t} \text{ and } \vec{B} = \nabla \times \vec{A} \,, \tag{1.17}$$

By replacing the momentum $\vec{P}$ to $\vec{P} + \frac{e}{c}\frac{\partial \vec{A}}{\partial t}$, where P is the momentum conjugate to the position vector. By substituting $\vec{P} + \frac{e}{c}\frac{\partial \vec{A}}{\partial t}$ into Eq. (1.5), one can reach:

$$\mathrm{H} = -\frac{P^2}{2m} + \mathrm{V}(\vec{r}) + \frac{e}{mc}\vec{A} * \vec{P} \,, \tag{1.18}$$

Eq. (18) ignores the contribution from quadratic term. Comparing with unperturbed Hamiltonian, the extra term $\frac{e}{mc}\vec{A} * \vec{P}$ represents the interaction between the radiation and a Bloch electron. The simplest way to solve the Hamiltonian is to assume that the perturbed field is weak and then use the time dependent perturbation theory (in the form of Fermi Golden Rule) to calculate the transition probability per unit volume R for an electron in the valence band state $|\mathrm{v}>$ with energy $\mathrm{E_v}$ and wavevector $\overrightarrow{k_v}$ to the conduction band $|\mathrm{c}>$ with corresponding energy $\mathrm{E_c}$ and wavevector $\overrightarrow{k_c}$. The detailed process to calculate the transition rate can be found elsewhere. [12] Eventually, the power loss from the field can be expressed in terms of imaginary part of dielectric constant ε_i, in which:

$$\varepsilon_i(\omega) = \frac{1}{4\pi\varepsilon_0}\left(\frac{2\pi e}{m\omega}\right)^2 \sum_{\vec{k}} |P_{cv}|^2 \delta\left(E_c\left(\vec{k}\right) - E_v\left(\vec{k}\right) - \hbar\omega\right), \qquad (1.19)$$

where P_{cv} is the matrix element between edge of conduction band and valence band, respectively.

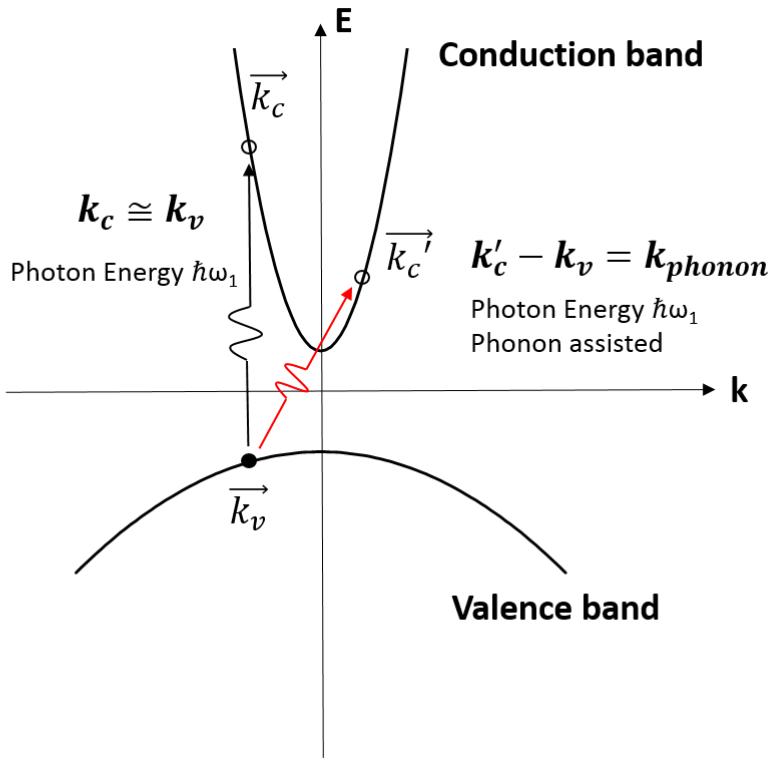

Figure 1.7. The schematic showing direct and indirect absorption in semiconductor. K_c , K_v and K_{photon} are the wave vector in conduction band, valance band, and that for phonon, respectively. Black circles represent the filled state in valence band, hollow circles represent the empty state in conduction band, respectively.

Eq. (1.19) describes the dispersion spectrum of absorption coefficient of semiconductors. First of all, the delta function shows the conservation of energy and momentum according to Fermi Golden rule, in which the energy difference between two levels should be equal to photon energy of incident light, and electron momentum of two state should be the same. It represent a process of "vertical" transition, as shown in Figure 1.7. However, in narrow bandgap materials, this is not

always the case. Wave-vectors of two states may not be equal due to the phonon assisted process, [13] in which the difference in wavevector would be compensated by emission, or absorption of phonons. Secondly, the absorption coefficient is proportional to the matrix element. For homogeneous III-V materials bulk materials, the matrix element is more or less constant. On the contrary, the matrix element is highly dependent on the overlap of wave function of two states in quantum confined structures, which will be described in the following section. Eq. (1.19) also shows that the magnitude of absorption coefficient is proportional to the joint density of states (DOS) in that has energy difference $E_c(\vec{k}) - E_v(\vec{k}) = \hbar\omega$. The joint density of state could be expressed as:

$$\mathrm{D(E)} = \sum_{\vec{k}} \delta(E_c(\vec{k}) - E_v(\vec{k}) - E)\ , \qquad (1.20)$$

For bulk materials, $\mathrm{D} \propto (m_e^* E)^{3/2}$, while $\mathrm{D} \propto m_e^*$ for 2D quantum well. Therefore, the smaller effective mass in conduction band, usually the smaller absorption will be. And it is common that bulk materials have a larger absorption coefficient compared with 2D quantum well structures. It is worthy to note that Eq.(1.19) simply described the absorption coefficient, assuming that all electrons stay in the valence band, and conduction band is empty, which is not always the case in real materials. For corrections, Eq. (1.19) should be modified by multiplying fermi distribution difference between electrons in valence band and conduction band, in which:

$$\mathrm{f} = f_v - f_c = \frac{1}{1+\exp\left((E_v(\vec{k}) - E_{fp})/kT\right)} - \frac{1}{1+\exp\left((E_c(\vec{k}) - E_{fn})/kT\right)}\ , \qquad (1.21)$$

where the E_{fp}, and E_{fn} is quasi-Fermi level for electrons and holes, respectively. In real case, when the materials is doped, the quasi fermi level will shift, resulting in the shift of optical transition energy. This phenomenon is called Burstein-Moss shift.

As discussed above, the fundamental absorption of materials depends mainly on its energy bandgap, wave-function overlapping, as well as the density of state. In the following sections, specific materials system of group III-V for LWIR absorption will be introduced.

1.5 Infrared Photodetectors based on quantum well

Quantum well based IR photodetectors or QWIP utilize the intersubband transitions of electrons (holes) in the QWs made out of wide bandgap materials to realize the effective narrow optical transition energy. The possibility of using GaAs/A1GaAs multiquantum wells for MWIR and LWIR photo-absorption was first suggested by Esaki and Sakaki [2], and experimentally investigated by Smith et al." and Chiu et aL [14]. The advantage of QW based photodetectors includes the mature GaAs growth and processing technologies. It results in high uniformity, excellent reproducibility, and thus large-area, low-cost staring arrays. In addition, the absorption spectrum lineshape could be accurately tailored by structure design, allowing monolithically integrated multispectral infrared detectors as well as the potential for monolithic integration with high-speed GaAs multiplexers and other electronics.

The intersubband absorption originates from transition between quantified energy levels within the same conduction or valance band, as shown in Figure 1.8. The levels result from the spatial localization of wavefunction in materials of narrower band gap in Type I quantum well configuration, where wide bandgap materials sandwich narrow bandgap materials. Assuming the valance band offset is infinite, the quantized energy levels E_n could be expressed as:

$$E_n = \frac{\hbar^2}{2m^*}\frac{\pi^2}{L}n^2 \ , \qquad (1.22)$$

where L is the width of QW, m^* is the effective mass in the QW, n is the quantized level. As a result, the transition energy between ground state and first quantized state is: $E_2 - E_1 = \frac{3\hbar^2}{2m^*}\frac{\pi^2}{L}$. By properly tuning the thickness of QW, one can reach desired transition energy. Due to the selection rule, the states involving in optical transition should have opposition parity, so that the matrix element $< 1|z|2 >$ wouldn't be nonzero, where x is coordinate in the growth direction. By considering the transition between the first two levels in infinite levels, the matrix element is:

$$X_{12} =< 1|x|2 >= \frac{1}{L}\int_{-\frac{L}{2}}^{\frac{L}{2}} dx sin\left(\frac{\pi}{L}x\right)\cos\left(\frac{3\pi}{L}x\right)x = \frac{16L}{9\pi^2}, \quad (1.23)$$

Therefore, according to Eq. (1.19), the absorption for interband transition could be expressed as: [15]

$$\alpha(\hbar\omega) = 2\left(\frac{e^2\omega}{cn\epsilon_0}\right)\frac{\left(\frac{\Gamma}{2}\right)X_{12}^2}{(E_2-E_1-\hbar\omega)^2+\frac{\Gamma^2}{2}} * \rho_{2D}N_w, \quad (1.24)$$

where ρ_{2D} is the 2D density of states is $\frac{m^*}{\pi^2\hbar L}$, and N_w is the number of QWs in the systems. In Eq. (1.24), the delta function is approximated by Lorentzain line shape. If one integrate the absorption spectrum for whole spectrum range, it will lead to [16]:

$$\int_0^\infty \alpha(\hbar\omega)d(\hbar\omega) = \frac{\rho_{2D}N_w e^2 h}{4cn\epsilon_0 m^*}f, \quad (1.25)$$

where $f = \frac{2m^*}{\hbar^2}(E_2 - E_1)X_{12}^2$ is the oscillation strength of levels of first excited state and ground state. According to Eq. (1.22) and (1.23), f turns out be a quantity independent of QW width. In terms of GaAs, f is 0.96, which implies a strong coupling between state 2 and 1.

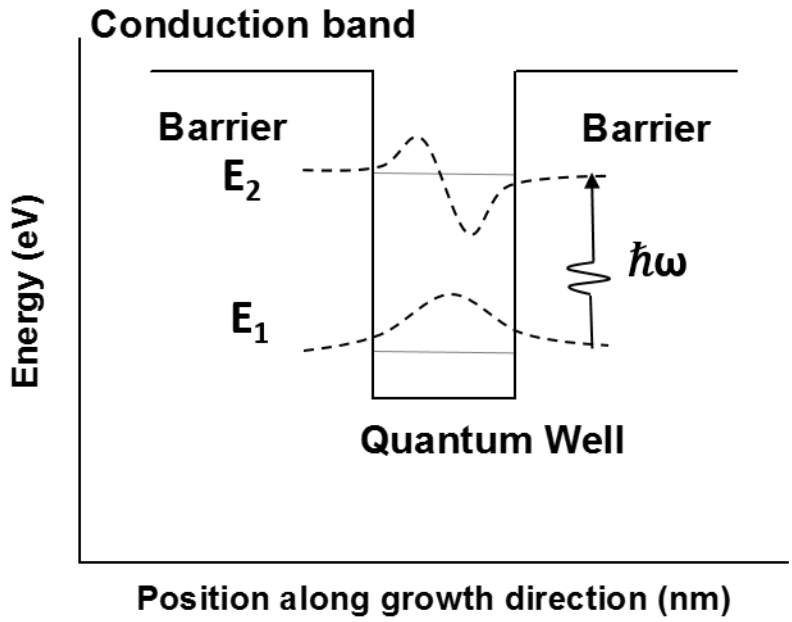

Figure 1.8. The schematic conduction band edge profile of a quantum well infrared photodetector (QWIP) and schematic of intersubband transition from ground state (E1) to excited state (E2).

Eq. (1.24) and Eq. (1.25) describe the main properties of intersubband absorption characteristics in quantum well systems. First of all, the absorption is highly polarized dependent. According to the selection rule, the incident light must have component in growth direction, otherwise normal incidence, for example, could be not absorbed by quantum well. As a consequence, for QWIP, incident light is usually coupled by waveguide or prism structure to change the polarization of incident light. Recently, surface polarization plasomon structure were used to enhance the absorption of quantum well [17]. Quantum efficieny larger than 10% were demonstrated in QWIP with a cutoff wavelength more than 10 μm. Secondary, the Lorentzian line shape in Eq. (1.24) implies that the spectrum range of intersubband transition is very narrow compared to those of superlattice and bulk materials. Such properties limit the performance of QWIP in the area of thermal

imaging, where broad response spectrum is required. This draw back was overcome by "multi-colored" design, where structures consist of several different active layers covering different spectral regions. Moreover, according to Eq. (1.25), the integration of absorption is almost constant, regardless of the transition energy levels involved in it. As a consequence, the transition between bound and continuum states usually has a low absorption compared with bound to bound states, due to broad line shape. [18] In some structure design which is aimed to facilitate transport of photo-generated carriers, there is a compromise between transient time and absorption coefficient.

Till now, intersubband transition in multiple QW still attracts the research interest in the area of MWIR and LWIR optoelectronics. There are numerous applications based on the tunneling properties of multiple quantum well, i.e. the development of quantum cascade laser [19]. Along with it, the QWIP for MWIR and LWIR photo-detection has been increasingly growing [18]. Even though the absorption coefficient is limited by its own natural characteristics, it has been partially compensated by engineering of optics coupling structures. Due to its mature technology, low cost and high uniformity, QWIP has become one of the main forces to replace Mercury-based photodetectors in LWIR region in industry.

1.6 Infrared Photodetector based on Ga(In)Sb/InAs type II superlattice

Since Esaki et al invented the repeated structures mimicking the long range properties in natural crystal, the superlattices (SLs) have demonstrated its astonishing optical and electrical properties. In the area of MWIR and LWIR photodetection, InAs/GaSb based type II SLs has recently shown significant development, and proven itself as a promising alternative material system to the state

of art MCT and QWIP. The advantage of InAs/GaSb lies in the fact that the optical transition energy could be widely tailored (from 3 μm to 30 μm) by tuning the period thickness In the type II band allignment, electrons and holes are localized in different layers. As a consequence, the Auger recombination is significantly suppressed, [20] which is extremely important for LWIR photodetector design. Due to the development of growth technology, thick and strained balanced Ga(In)Sb/InAs SLs has been grown on GaSb substrate with a good quality.

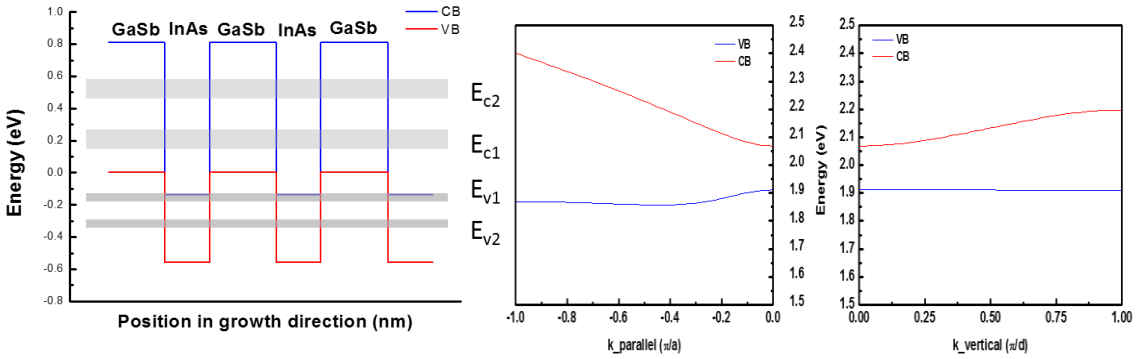

(a) (b)

Figure 1.9. (a), The band edge profile of GaSb/InAs type II strained balanced superlattice SLs, and the schematic mini-bands with the structures. CB and VB represent conduction and valence band edges, respectively. The energy dispersion spectrum of GaSb/InAs SLS (2.4/4.8 nm), in parallel directions and growth directions, respectively. The band diagram is calculated using nextnano. [9]

The GaSb/InAs band edge alignment is shown in Figure 1.9 (a). It shows that energy level at top of valance band of GaSb is higher than that of conduction band of InAs, which is called broken band situation. Different from multiple quantum well, the thickness of each layer is narrow (<10 nm), so that the state in each layer starts to interact with that of neighboring QW. Similar to what happens in natural crystal, the closely packed quantized states in SLs form minibands along this direction, as shown in Figure 1.9 (a). Due to the translational symmetry, the wave function in the growth direction could be expressed in the form of Bloch function as $u_{nq}(z) =$

exp(iqz)$u_n(z)$, where q is the wave vectors along the z direction, and should be equal to 2πi/(d*N), where d is the period of superlattice, N is the number of superlattice in growth direction, and i is the integer number. It implies that the phase difference between adjunct quantum well is exp(iqd). It also implies that compared with normal bulk materials the first Brillouin Zone in growth direction decreases from 2π/a to 2π/d, which is the main idea for observation of Bloch oscillation in SLs. [21]

The band structure could be calculated by kp method [22]. A simplified method would be introduced here to illustrate the general properties of absorption in SLs. Considering an isolated QWs with thickness of L, and sandwiched by two barriers with barrier potential V, and thickness h. As shown in Figure 1.9(a), the wave function of free electron in this two layers could be expressed as:

$$\varphi(z) = \begin{cases} aexp(ik_w z) + bexp(-ik_w z), & \left(-\frac{L}{2} < z < \frac{L}{2}\right) \\ cexp\left(k_b\left(z - \frac{L+h}{2}\right) + dexp\left(-k_b\left(z - \frac{L+h}{2}\right)\right), & \left(\frac{L}{2} < z < \frac{L}{2} + h\right) \end{cases}, \quad (1.26)$$

where $k_w = \sqrt{\frac{2mE}{\hbar^2}}$ is wave vector in quantum well, $k_b =$ is wave vector in the barrier, assuming 0<E<V. By applying the boundary condition of at φ(z) and φ′(z) z=L/2, one should have,

$$\begin{cases} aexp\left(\frac{ik_w L}{2}\right) + bexp\left(\frac{-ik_w L}{2}\right) = cexp(-k_b h/2) + dexp(k_b h/2) \\ ik_w\left(aexp\left(\frac{ik_w L}{2}\right) - bexp\left(\frac{-ik_w L}{2}\right)\right) = ck_b\left(exp\left(-\frac{k_b h}{2}\right) - dexp\left(\frac{k_b h}{2}\right)\right) \end{cases}, \quad (1.27)$$

In the next step, we consider repeating the single QW structure to make it a SLs. The Eq. (1.27) is still valid on the interface z=L. By applying the translation symmetry,

one has $\varphi(\frac{L+2h}{2})$ =exp(iqd) $\varphi(\frac{L+2h}{2}-d)$ =exp(iqd) $\varphi(-\frac{L}{2})$. The same goes to boundary condition for $\varphi'(z)$. Then we have :

$$\begin{cases} \exp(iqd)(aexp\left(\frac{ik_wL}{2}\right)+bexp\left(\frac{-ik_wL}{2}\right)) = cexp(k_bh/2)+dexp(-k_bh/2) \\ \exp(iqd)(ik_w\left(aexp\left(\frac{ik_wL}{2}\right)-bexp\left(\frac{-ik_wL}{2}\right)\right)) = ck_b(exp\left(\frac{k_bh}{2}\right)-dexp\left(-\frac{k_bh}{2}\right)) \end{cases}$$

, (1.28)

We finally end up with a 4 by 4 homogeneous system with 4 unknown parameters. The non-trivial solutions exist only when determinant of matrix is zero. We have the dispersion relation as:

$$\cos(qd) = \cos(k_wL)\cosh(k_bh) - 1/2(\frac{k_w}{k_b}-\frac{k_b}{k_w})\sin(k_wL)\sinh(k_bh), \quad (1.29)$$

If we denote $F(E) = \cos(k_wL)\cosh(k_bh) - 1/2(\frac{k_w}{k_b}-\frac{k_b}{k_w})\sin(k_wL)\sinh(k_bh)$, by using the Taylor expansion to the first order around the jth levels E_j in isolated quantum well, we can have:

$$E_j(q) = E_j - F(E_j) + \frac{\cos(qd)}{F'(E_j)}, \quad (1.30)$$

Eq. (1.30) is the simplified band structure near the band edge along the growth directions. It is equivalent to the tight-binding method. It shows that the single level in the QW evolves to a band. The band width depends on the potential of the barriers and thickness. In real case, the band width is sensitive to effective mass of the materials in SLs. Since Eq. (1.30) is equivalent to tight-binding method, the expression for wave function should be also similar as tight-binding wave function, which is:

$$\varphi(z) = \frac{1}{\sqrt{N}}\sum_n \exp(iqnd)\varphi_{loc}^{j}(z-nd),$$

where $\varphi_{loc}^{j}(z)$ represents the localized wavefunction in jth level. (1.31) Actually it is the solution of single quantum well for jth level, as shown in Eq. (1.26). Once the wavefunction along the growth direction is known, the global wave function of the SLs could be expressed as $\Phi(\mathbf{r}) = u(\mathbf{r})\varphi(z)$, where $u(\mathbf{r})$ is the bulk wavefunction of single materials. It implies that the wavefunction of SLs is modified by the periodic structures in growth directions. By substituting the modified wavefunction into Eq. (1.19), one can have the absorption coefficient for the SLs. The main difference lies in the matrix element. For SLs the matrix element could be expressed as:

$$P_{cv} = < u_c(\mathbf{r})\varphi_c(z)|P_i|u_v(\mathbf{r})\varphi_v(z) >, \text{ i=x,y,z} \qquad (1.32)$$

where $u_c(\mathbf{r})$, $u_v(\mathbf{r})$, $\varphi_c(z)$, $\varphi_v(z)$ is the wave function of bulk, and SLs for conduction band, and valence band, respectively. Since the Brillouin zone of bulk materials is much larger than that of the SLs, the matrix element could be approximated as [23]:

$$P_{cv} \cong < u_c(\mathbf{r})|P||u_v(\mathbf{r}) >< \varphi_c(z)|\varphi_v(z) >=< \varphi_c(z)|\varphi_v(z) > P_{bulk}, \qquad (1.33)$$

where P_{bulk} is the matrix element of the bulk. Eq. (1.33) shows that the absorption coefficient of SLs is modified by the wave function overlaps in SLs. Since the overlaps of wave function is usually smaller than unity in type II SLs, Eq. (1.33) implies that the oscillation strength of SLs is usually smaller than that of bulk materials with similar bandgap. Moreover, in order to narrow the optical transition energy, the period usually need to be increased, which results in the decrease overlaps of wavefunction between electrons and holes. As a consequence, the absorption coefficient of type II SLs is limited by its function overlaps. There were a lot of effort focused on optimization of the wave function overlaps, while keeping the optics transition energy constant. Generally speaking, the drawback of

absorption of SLs could be compensated by increasing the absorber layer thickness. Recently, high quantum efficiency (more than 40%) photodetectors with absorber more than 5 μm has been demonstrated [24], but this may induce some other issues, i.e. increase of dark current. Therefore, in design of photodetectors, there is always a compromise between quantum efficiency and dark current.

1.7 Summary

In this chapter, the basic background for the group III-V semiconductors is introduced. Due to the special periodic arrangement of lattices, the group III-V semiconductors have an optical bandgap ranging from LWIR to UV region. It is shown that materials should have a narrow optical bandgap, and a large absorption coefficient, in order to have high quantum efficiency of LWIR photodetection. It is also shown that due to natural characteristics, absorption coefficients of QWIP and type II SLs are limited and smaller than the bulk materials. Therefore, a bulk material with narrow bandgap is always desirable. However, there has been growth issues that impeded the development of bulk InAsSb narrow bandgap materials for the last decades. That is exactly the point of my work. In the following chapters, the way to overcome this problem will be shown. The optical and electrical characteristics of unrelaxed bulk InAsSb will be discussed.

Chapter 2

Pseudomorphically grown InAsSb alloys and heterostructures

2.1 Introduction

As stated in the previous chapter, growth of $InAs_{1-x}Sb_x$–based epitaxial materials for infrared photodetectors has a long development history [25-26]. A strong energy gap bowing in these materials suggests the smallest energy gaps available for III-V semiconductor compounds. (Figure 2.1). One the other hand, the InAsSb-based materials may have advantages over InAs/GaSb SLS due to different carrier recombination properties [27] associated with absence of Ga-related defect centers [28]. As consequences, InAsSb was considered as one of the promising candidate materials for LWIR optoelectronics. However the development of InAsSb alloys was challenged to accommodate the large lattice mismatch between InAsSb and commercial available substrates. The key issue in mismatched epitaxy is to minimize the dislocations that penetrate through the epi-structures. Earlier work reported the growth of relaxed InAsSb layers on various substrates [29-31], photoconductive detectors based on relaxed InAsSb grown on GaAs were demonstrated [32], and the relaxed InAsSb showed high dislocation densities and relatively broad photoluminescence spectra [33-34].

The bulk InAsSb materials were grown on various substrates: InSb [33], InAs, semi-insulating GaAs [34], most with various degrees of relaxation and residual strain. Various approaches to the growth of buffer layers on InSb [33], GaSb [34], and other substrates were employed for the reduction of density of threading dislocations but no sufficient details on methodology and material characterization

were presented. In our work, we increased the lattice parameter of the GaSb substrate by growing linearly compositionally graded Ga(Al)InSb buffers, following the approach in [4]. The graded strain in the buffer layers facilitates the glide of threading dislocations and reduces the densities of dislocations that propagate through the buffer layer into the active region [4]. High quality $InAs_{1-X}Sb_X$ layers having non-tetragonally distorted, strain-free lattice parameters were grown on top of the buffer layers.

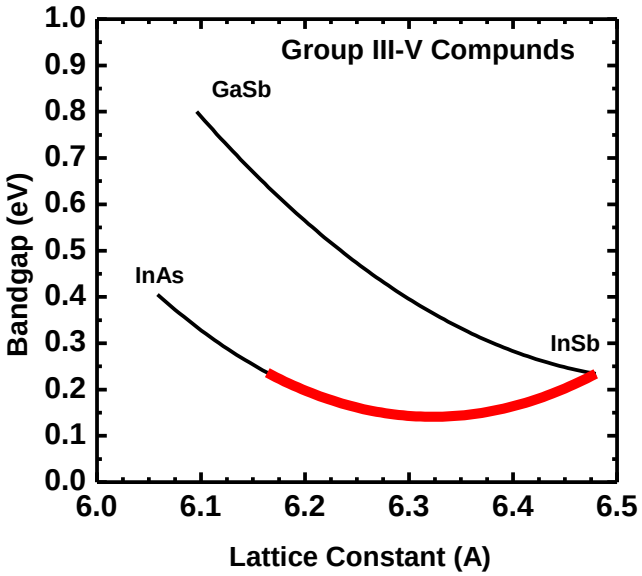

Figure 2.1. The relationship between bandgap and lattice constant for InAsSb and GaInSb alloys.

In the first section, the structural properties for both buffer and active layers are characterized by the transmission electron microscope (TEM) and high resolution x-ray diffraction (HRXRD). The behavior of threading dislocation is investigated. In the second section, the PL spectra are obtained from InAsSb bulk materials with different Sb composition at different temperatures. From the PL spectra, basic parameters, such as band bowing parameter, and Vashni's parameters are determined. In order to have a practical application in heterostructures, the band offset energies of conduction and valance bands are approximated by measuring the

PL from InAs/InAsSb superlattice. At last, the lifetime of Ga-Free SLs is investigated using transient PL measurement.

2.2 Structural Characterization

The heterostructures were grown on GaSb substrates by solid-source molecular beam epitaxy using a Veeco GEN-930 system equipped with As and Sb valved cracker sources. Molecular beam fluxes were measured by an ion gauge positioned in the beam path. The substrate temperature was controlled by a pyrometer, which was calibrated using references such as the III to V enriched surface reconstruction transition, oxide desorption and the melting point of InSb. The compositionally graded 2~3.5 μm thick Ga(Al)InSb buffer layers were grown at temperatures ranging from 460 to 520 ˚C. The growth temperature was maintained near 415 ˚C for the InAsSb layers. The Sb incorporation was controlled by the adjustment of the relative pressure of the As and Sb group V elements as measured by the beam-flux-monitor. The growth rate was about 1 μm per hour. $InAs_{1-x}Sb_x$ layers with x = 20, 30 and 44% were grown on GaInSb and AlGaInSb buffers.

The defect distribution in linearly compositionally graded GaInSb and AlGaInSb buffers were characterized by cross-sectional TEM images. Figure 2.2 shows the XTEM images of structures with either laser or absorber layers grown on top of three different linearly graded buffer layerss;including (a) GaInSb with top In content of 16%; (b) GaInSb with top In content of 30%; (c) AlGaInSb with top Al, Ga and In contents of 75, 0 and 25 %, respectively. The images were taken with a (220) bright field two-beam condition to emphasize the dislocations. In all three structures, the misfit dislocation network was confined in the bottom part (~1.5 μm) of the graded buffers; the topmost portion of the buffers as well as the epi-structures grown onto the buffers is free from misfit dislocations. TEM results did not show

any noticeable difference in the dislocation morphology of these two buffer layers or in the laser or absorber layer structures grown on top of them, both appear to be equally efficient in accommodating the misfit strain. From the images, we can estimate that the threading dislocation density is below 10^7 cm^{-2} in the $InAs_{1-X}Sb_X$ layers.

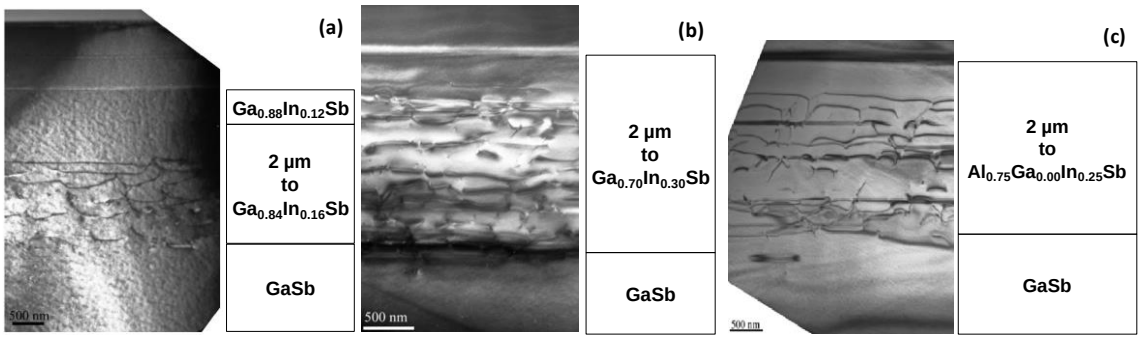

Figure 2.2. Cross-sectional TEM images of samples with 2 µm thick linearly graded buffers grown on GaSb substrates: (a) GaInSb with top In content of 16 % - accomodated 0.9 % mismatch; (b) GaInSb with top In content of 30 % - accomodated 1.4 % mismatch; (c) AlGaInSb with top Al, Ga and In contents of 75, 0 and 25 % - accomodated 1.4 % mismatch.

Strain relaxation of the structures was examined using high-resolution X-ray diffraction reciprocal-space mapping (RSM) at the symmetric (004) and asymmetric (335) Bragg reflections. Figure 2.3 presents a set of RSM measurements for a structure consisting of a 1 µm $InAs_{0.8}Sb_{0.2}$ layer grown on a 2 µm linearly compositionally graded AlGaInSb buffer layer. The native lattice constant of the $InAs_{0.8}Sb_{0.2}$ layers is about 0.8% larger than that of GaSb. The native lattice constant of the buffer layer changed from that of GaSb to that of $Al_{0.75}Ga_{0.13}In_{0.12}Sb$ with a strain ramp rate about 0.6% per µm. The topmost section of the graded buffer with $Al_{0.75}Ga_{0.13}In_{0.12}Sb$ composition had a native lattice constant about 1.3% larger than that of GaSb, but due to compressive strain, the in-plane lattice constant is equal to the native constant of the bulk $InAs_{0.8}Sb_{0.2}$. When the final structure was grown, the InAsSb layer was sandwiched between $Al_{0.75}Ga_{0.13}In_{0.12}Sb$ carrier confinement layers to assist photoluminescence experiments.

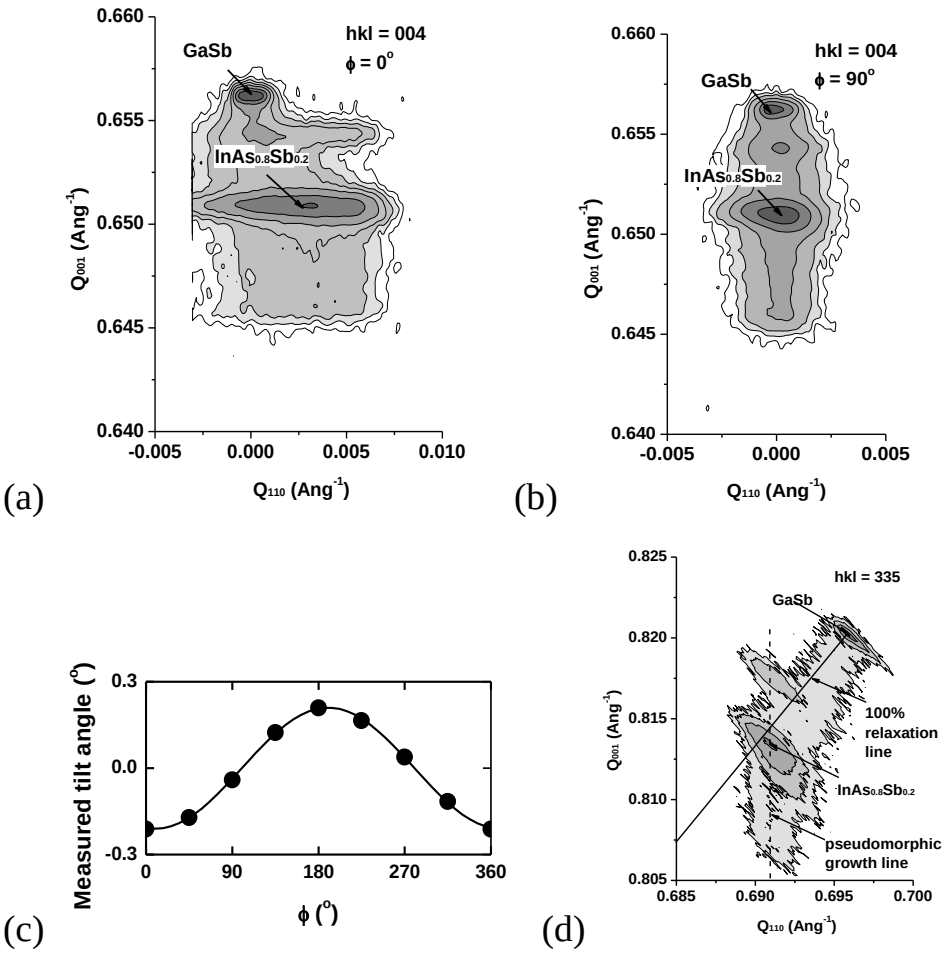

Figure 2.3. (a) Symmetric (004) RSM taken at the azimuth angle emphasizing the tilt in the epi-layers; (b) (004) RSM taken at the azimuth angle minimizing the tilt in the epi-layers; (c) dependence of the measured tilt angle as a function of the azimuth angle; (d) asymmetric (335) RSM taken at azimuth angle equal to 90˚. Solid line denotes the location of 335 reflexes corresponding to fully relaxed material with lattice parameter gradually increasing from that of GaSb. Dashed line denotes the location of 335 reflexes of the material with further increasing native lattice parameter but grown pseudomorphically to the top of fully relaxed section.

The symmetric reflection revealed the presence tilt present in the epi-structure. Figure 2.3 (a) and (b) shows the RSMs obtained near the symmetric (004) reflection at two azimuth angles, namely (a) φ = 0˚ and (b) φ = 90˚, corresponding to two perpendicular [110] crystallographic directions. The tilt angle projected to the measurement plane is determined from the horizontal peak separation between the GaSb substrate and the epi-layers. As shown in Figure 2.3 (a), the tilt angle increases

as the thickness increases in the bottom part of the graded buffer, and stops as increasing in the consequent layers. The bottom part of the buffer layers is near completely relaxed, as will be shown later, suggesting that tilting is associated with the process of strain relaxation. Figure 2.3 (c) plots the projected tilt angle as a function of several azimuth angle φ. We estimate the tilt angle to be 0.2˚ in the direction about 10˚ away from the [110] direction (φ = 90˚).

Asymmetric (335) RSM reflexes were measured at four different azimuth angles in order to characterize the degree of relaxation of the graded buffer layer and to confirm that the $InAs_{0.8}Sb_{0.2}$ layer is lattice-matched to the topmost part of the graded buffer. Figure 2.3 (d) shows one of the (335) RSMs measured at an azimuth angle equal to 90˚, i.e., with the minimum tilting effect. The shift visible in the (335) RSM corresponds to the transition from the strain relaxed to the pseudomorphic section of the graded buffer. For illustrative purposes, the solid line corresponds to a 100% relaxed square lattice. The observed relaxation is close to 100%. After the tilt angle is accounted for, the degree of relaxation in this section of the graded buffer can be estimated as 95%, i.e., nearly 100%, and within our experimental error. The pseudomorphic growth of the dislocation-free topmost section of the buffer layer is apparent from the (335) scan since the reflex from the buffer layer is nearly vertical (dashed line in figure 2.3 (d)). The reflection from the $InAs_{0.8}Sb_{0.2}$ layer is located at the turning point and on the same vertical line as the pseudomorphic section of the buffer, which confirms lattice matching to the in-plane lattice constant of the graded buffer layer. The amount of strain in the $InAs_{0.8}Sb_{0.2}$ layer is below 0.1%; therefore, no strain relaxation is expected. The reflection located above the InAsSb reflection in both the (004) and (335) RSM corresponds to a pseudomorphically strained auxiliary AlGaSb layer (~150 nm) that was grown on top of the InAsSb layer for calibration purposes.

2.3 Optical Characterization

For optical measurement structures, bulk InAsSb epilayers on the metamorphic buffers were grown on GaSb substrates by solid-source MBE. In the case of the bulk InAsSb materials the lattice mismatch with the substrate was accommodated with compositionally–graded AlInAsSb buffers. An unstrained 200-nm thick AlInAsSb carrier confinement layer (virtual substrate) with a lattice constant matched to the lateral lattice constant of the topmost part of the buffer was grown before the InAsSb layer. The composition of the $InAs_{1-x}Sb_x$ layer was selected to achieve lattice-matching of the confinement layer to the lattice constants of the free–standing (unstrained) InAsSb. The unintentionally doped InAsSb layers were 1-μm thick, with Sb compostion varying from 20% to 65%. The top AlInAsSb confinement layer was similar to the virtual substrate. The heterostructures were capped with a 200 nm thick InAsSb layer of the same composition as the bulk material to prevent exposure of the Al-containing barrier to the ambient.

The PL measurement setup is discussed in Appedix 1. The PL was excited with a Nd:YAG laser (λ=1064 nm) operating either in continuous–wave (CW) or Q-switched mode. The PL spectra were obtained with a FTIR spectrometer Nicolet Magna-860. The PL was detected with an external liquid-nitrogen cooled MCT photodetector with the spectral response extending up to 14 μm. The excitation source operating in CW mode with external modulation at the frequency of 1 kHz and the FTIR in the step-scan mode were used for PL measurements in the wavelength range longer than 8 μm. In the wavelength range below 8 μm the FTIR operated in the continuous-scan mode. With variation of the sample temperature from 13 K to 300 K, the CW power level ranged from 20 to 500 mW. The corresponding power densities were from 2 to 50 W/cm^2. The structures were cooled

with a close-cycle He cryohead M22 (Janis) with ZnSe window coating optimized for high transmission in the long wavelength infrared range. The PL was collected with the reflective objective. High excitation of SLS structures for population of high energy states was obtained with the excitation source operating in the Q-switched mode with a 100-ns pulse width and the repetition rate of 100 kHz. The excitation area was 0.5 mm in diameter. The laser emission scattered from the sample and window surfaces was rejected with a Ge filter. The PL spectra measured in several points of the wafers showed high homogeneity of the material composition.

The energy gaps were determined from low temperature PL spectra obtained under low excitation power. This simplified approach provided adequate accuracy for ternary materials. Figure 2.4 shows the normalized PL spectra of the bulk InAsSb alloys, and binary epilayers measured at T = 13 K. The bulk InAsSb materials showed narrow PL spectra with a Gaussian line-shape. The FWHM of 11 meV was measured for the bulk InAsSb layers of both 20 and 44 % Sb compositions. The FWHM of PL for InAs layers (11 meV) was similar to that for the bulk InAsSb while the PL spectra of InSb epilayers showed a lower FWHM of 5.5 meV. The FWHM for InAsSb-based materials measured in this work were comparable to those reported in the literature for LWIR InAs/GaSb SLS [35]. From low temperature PL spectra obtained in a range of excitation powers (Figure 2.5), results showed that a blue shift of the PL peak did not exceed 2 meV with increase of CW pumping power from 20 to 100 mW. Small values of FWHM of PL spectra at T =13 K confirmed good homogeneity of the studied materials. It was concluded that for measurements of PL spectra in these materials the pumping power level of 100 mW with the excitation area 10^{-3} cm^2 was adequate.

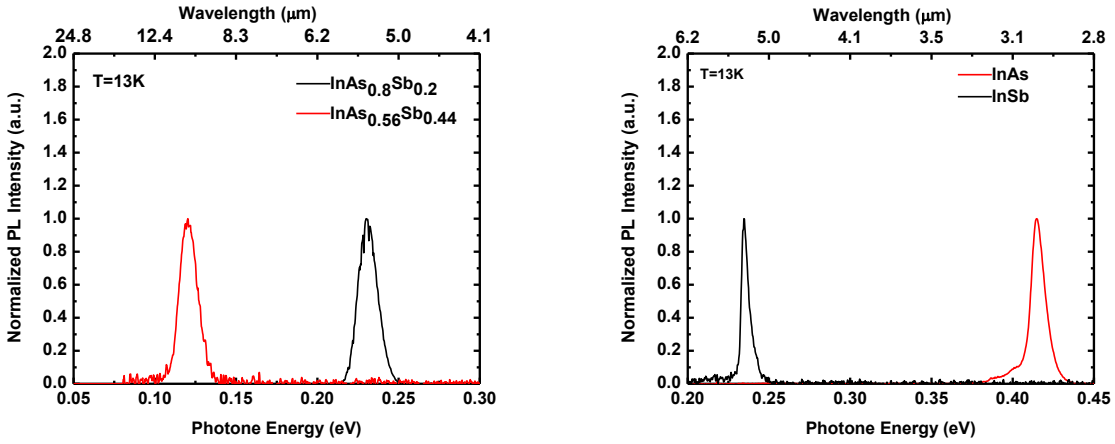

Figure 2.4. (a) The normalized PL spectra of bulk $InAs_{0.8}Sb_{0.2}$ and $InAs_{0.56}Sb_{0.44}$ alloys. (b) The normalized PL spectra of InAs and InSb layers. The measurements were performed at T= 13 K with the excitation power of 100 mW.

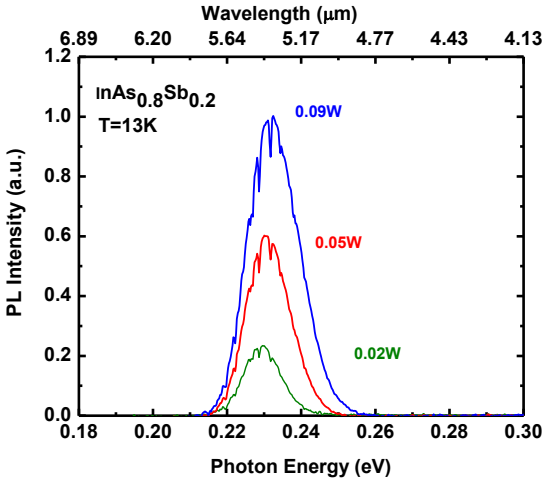

Figure 2.5. The PL spectra of $InAs_{0.8}Sb_{0.2}$ alloys at T = 13 K measured with the excitation power levels of 20, 50 and 90 mW. The excitation area was 1.2x10-3 cm-2. The shift of the energy maximum in the range of excitation power was below 2 meV.

The energy gaps of the materials were determined from the PL maxima at T=13 K. The bulk InAsSb layers with 20 and 44 % Sb showed the PL peak wavelengths of 5.2 μm (Eg = 0.24 eV) and 10.3 μm (Eg = 0.12 eV), respectively. The dependences of the energy gap on Sb composition are shown in Figure 2.6. The dependence was fit in accordance with the equation:

$$Eg(InAsSb) = (1-x)Eg(InAs) + x*Eg(InSb)-(1-x)*x*C \quad (2.1)$$

Here *Eg* (InAsSb), *Eg* (InAs), and *Eg* (InSb) are energy bandgaps of the materials, *C* is the bowing parameter for the energy gap. A good fit was obtained for *C* = 0.87 eV. The obtained value was greater than that reported in most experimental works and greater than the previously recommended value of 0.67 eV [37]. The variations in the reported data could be explained with differences in the growth conditions or the presence of residual strain of various degrees in the reported data, which can affect the energy band spectra and may lead to the possibility of the Cu-Pt ordering [36].

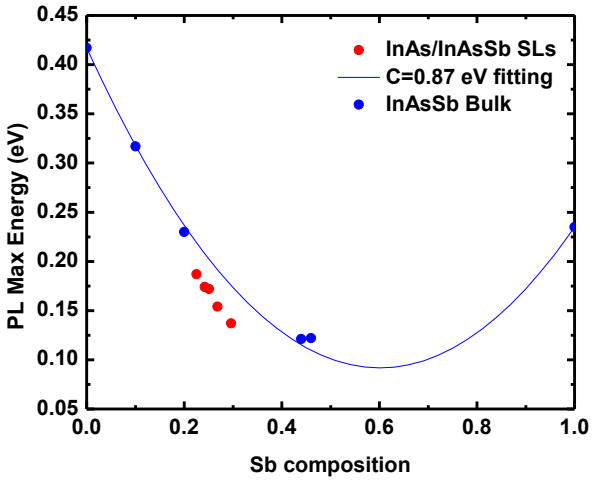

Figure 2.6. Dependence of the energy gaps on Sb composition in the bulk InAsSb grown on AlInAsSb metamorphic buffers (blue symbols) and in Type-II InAsSb/InAs SLS grown on GaSb (red symbols). The data were obtained from PL maxima determined at T=13 K. The fit for the bulk InAsSb was obtained with the energy gap bowing parameter 0.87 eV.

In order to determine the energy gap from the PL spectra at higher temperature, we must account for the broadening of PL with temperature. Assuming for conservation of the wave vector in the direct bandgap recombination with photon emission, one can expect the lineshape of the PL spectrum to be described by the expression below [38]:

$$I(h\omega) \propto (h\omega - Eg)^{1/2} \exp(-(h\omega - Eg)/k_B T) \qquad (2.2)$$

Here $h\omega$ is the photon energy, Eg is the energy bandgap of the material, k_B is the Boltzmann constant, and T is the temperature of carriers. By differentiation of Eq (2) one can show that the PL emission achieves its peak at the photon energy of $k_BT/2$ greater than the energy of the bandgap. Thus, with wave vector conservation in the PL process, the energy gap can be estimated by subtraction of a half of k_BT from the photon energy at the PL peak value.

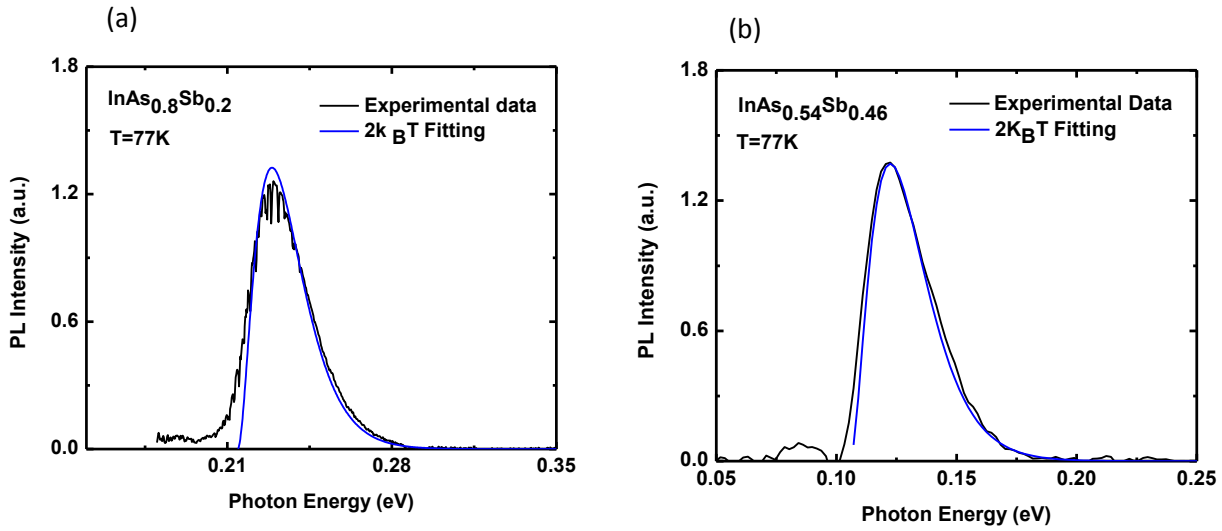

Figure 2.7. The PL spectra of the bulk $InAs_{0.8}Sb_{0.2}$ (a) and $InAs_{0.56}Sb_{0.46}$ (b) at T=77 K (black lines) and fitting based on Eq 2.3 (blue lines). See the text for details on fitting.

In the experiment, the high energy tail in the PL spectrum can be fit with an exponential term in Eq. 2.2 while in the range to the left of the PL maximum the line shape is broader than that predicted by Eq.2.2. Following the approach often used in literature [38], the expression for fitting of the experimental spectra was taken as shown below with term ($h\omega$ - Eg) in power n:

$$I(h\omega) \propto (h\omega - Eg)^{n} \exp(-(h\omega - Eg)/k_B T) \qquad (2.3)$$

Figure 2.7. shows the fits of PL spectra obtained with the use of Eq 2.3. A good fit of the experimental data was obtained with *n* close to 2. The value n=2 can be justified for the case of radiative recombination without the conservation of the wave vector [38]. Thus, the experimental results obtained in this work suggest the participation of phonons in the radiative recombination process. A deviation from the fit at low energies could be explained with the contribution of weaker two-phonon processes. With n=2 the energy gap can be obtained by subtraction of $2k_BT$ from the PL maxima. Note, that for the InAsSb with a 44 % Sb composition, the value of $2k_BT$ is about 10 % of the energy bandgap at 77 K. Thus for spectra at higher temperature, the band gap of bulk materials was approximated by subtracting $2k_BT$ from the PL maxima. In Figure 2.8 (a), the normalized PL spectra are shown for InAsSb with different Sb compostion from 20% to 55% at 77 K. The longest wavelength (12.4 μm) was demonstrated from the sample with Sb composition 55 %. It was the longest peak wavelength ever reported from group III-V bulk alloys. The PL data obtained for recently grown InAsSb layers with large Sb compositions were used for updating the value of the bowing parameter reported in the earlier publication [37]. Fitting the dependence of the band gap energies subtracted by $2k_BT$ from PL maxima on Sb composition with the data for previously and recently grown bulk InAsSb (Figure 2.9) is consistent with the energy gap bowing parameter of 0.87 eV.

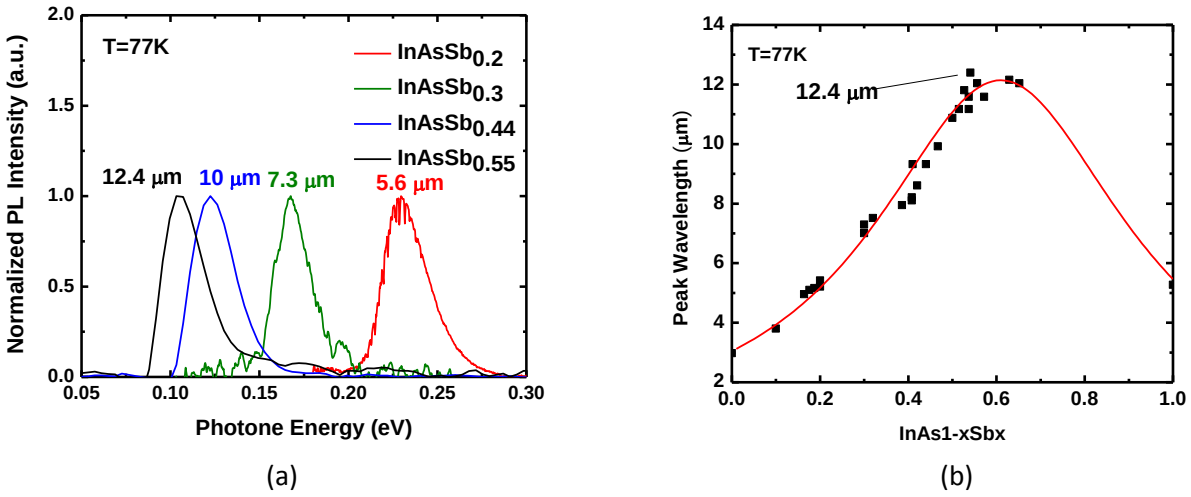

Figure 2.8. The normalized PL spectra for InAsSb bulk with different Sb compositions at 77 K. (20% red line, 30% green line, 44% blue line, 55% black line); 2.9. The dependence of PL peak wavelength versus Sb composition for bulk InAsSb measured at T=77 K. The best fit was obtained with the bowing parameter of 0.87 eV.

The temperature dependences of the energy gaps were determined with the help of PL spectra. The PL spectra of the bulk InAsSb for both Sb compositions in the temperature range up to 150 K were measured under a constant excitation level of 100 mW (Figure 2.9). In this range the bulk $InAs_{0.8}Sb_{0.2}$ showed a 30 meV shift of the PL peak while for $InAs_{0.54}Sb_{0.46}$ the energy was nearly constant. Figure 2.10 shows the temperature dependence of the energy gap obtained from the PL maxkum by subtraction of a $2k_BT$. The dependences were fit with Varshni parameters as shown below [40]

$$Eg = Eg0 - \alpha T^2/(T+\beta) \tag{2.4}$$

Here *Eg0* represents the energy gap of material at T = 0 K. The best fits were obtained with α=0.32 meV/K, β=100.4 K and α=0.12 meV/K, β=33.3 K for the bulk $InAs_{0.80}Sb_{0.20}$ and $InAs_{0.56}Sb_{0.44}$, respectively. The empirical parameter β is often attributed to the Debye temperature [39]. A smaller β value for $InAs_{0.54}Sb_{0.46}$ implies a greater role of lattice vibrations in narrow gap materials. This may explain a greater

role of radiative recombination without conservation of wave vector in PL of narrow gap materials.

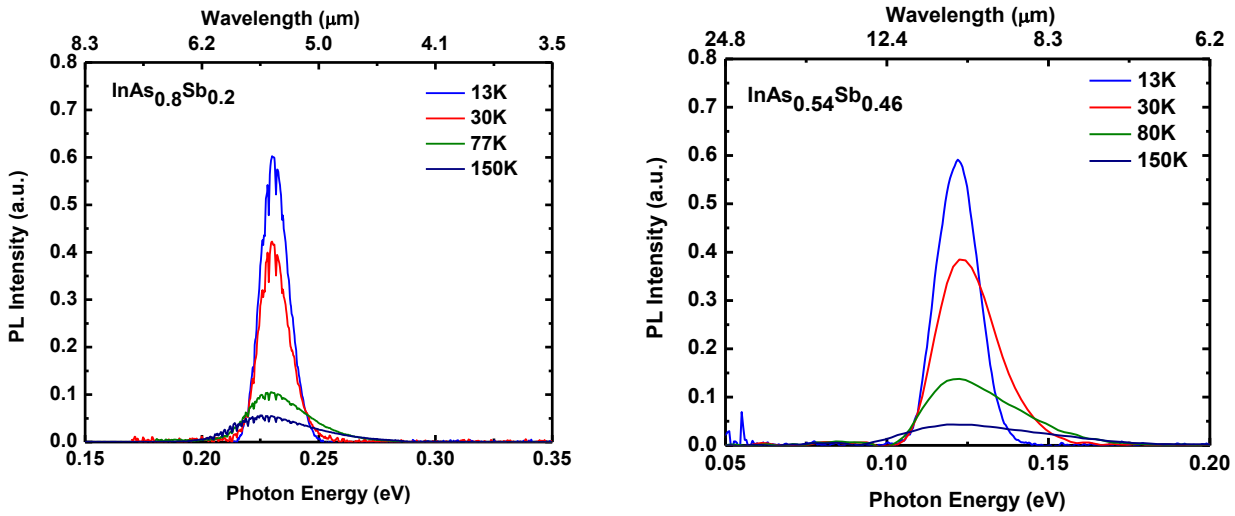

(a) (b)

Figure 2.9. The PL spectra of the bulk $InAs_{0.8}Sb_{0.2}$ (a) and $InAs_{0.54}Sb_{0.46}$ (b) at T=13 K, 30 K, 77 K, and 150 K.. The excitation power was 100 mW.

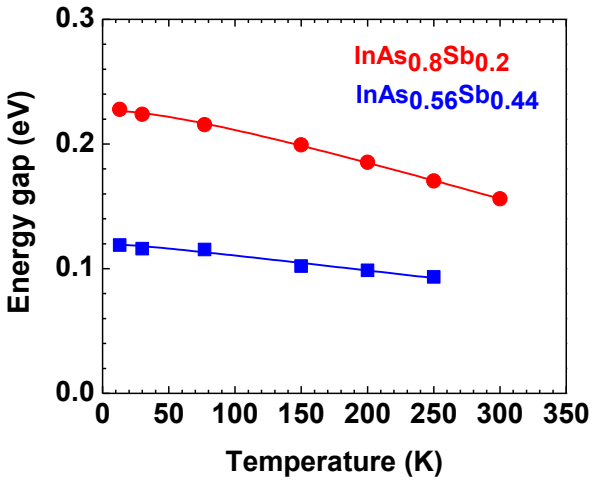

Figure 2.10. The temperature dependence of energy bandgaps. The fittings were obtained with the following Varshni parameters: Eg0= 0.226 eV, α=3.2 meV/K, b=100.4 K for $InAs_{0.8}Sb_{0.2}$ and Eg0= 0.119 eV, α=1.2 meV/K, b=33.3 K for $InAs_{0.56}Sb_{0.44}$.

To sum up, it was demonstrated that the bulk InAsSb materials free of group-V ordering grown on metamorphic buffers are capable of encompassing the long

wave infrared range at low temperatures. The longest PL peak wavelength of group III-V alloys (12.4 μm) at 77 K was shown. Temperature dependences of PL spectra were obtained for unrelaxed bulk InAsSb corresponding to energy gaps in mid-wave and long-wave IR spectral ranges. The bowing parameter for bulk InAsSb was found to be 0.87 eV which is considerably greater than the previously recommended value of 0.67 eV. Broadening of PL spectra with temperature was attributed to phonon-assisted radiative recombination without wave-vector conservation.

2.4 Band offset in heterostructures

The conduction and valance band energies in bulk InAsSb were estimated by measuring the PL peak position of InAs/InAsSb SLs. The design of Type-II SLs $InAs_{1-x}Sb_x$/InAs cells was similar to that published in Ref.41. The InAsSb portions of the SLs period had Sb compositions varied in the range from 22.5 to 29.6 %. All SLs structures had the target thicknesses of InAsSb and InAs layers of 173 A and 72 A, respectively. The relatively wide cells were chosen to minimize the energies of the electrons and holes in the SLs. This approach resulted in longer wavelength for the given range of Sb compositions and allowed for the more accurate determination of the energy offset at the InAsSb/InAs heterointerface. No AlSb confinement layers were used in contrast to the design in Ref. 41. The overall thickness of the SLS was 1 μm. The Sb composition was determined with XRD fitting. The actual thicknesses of the layers are shown in Table 2.1. Sharp XRD peaks and relatively narrow PL peaks of the samples indicated that the SLs structures were grown under strain without relaxation. The Type-II InAsSb/InAs SLs were grown at a substrate temperature of 490 C.

Figure 2.11 shows the normalized PL spectra of the bulk InAsSb alloys, type-II InAsSb/InAs SLs and binary epilayers measured at T = 13 K. Type-II SLs showed narrow PL spectra with a Gaussian line-shape. The FWHM of about 16 meV was

measured for all Type-II InAsSb/InAs SLs. The energy gaps for InAsSb/InAs SLs are lower than those for bulk InAsSb with similar Sb compositions due to the Type-II-c band-line-up [42]. In Figure 2.6 one can see a trend of more rapid decrease bandgaps for the SLs than the bulk material as Sb composition increases. This implies that the band offsets, ΔEc, must be increasing with the Sb composition at a faster rate than the InAsSb bandgap itself.

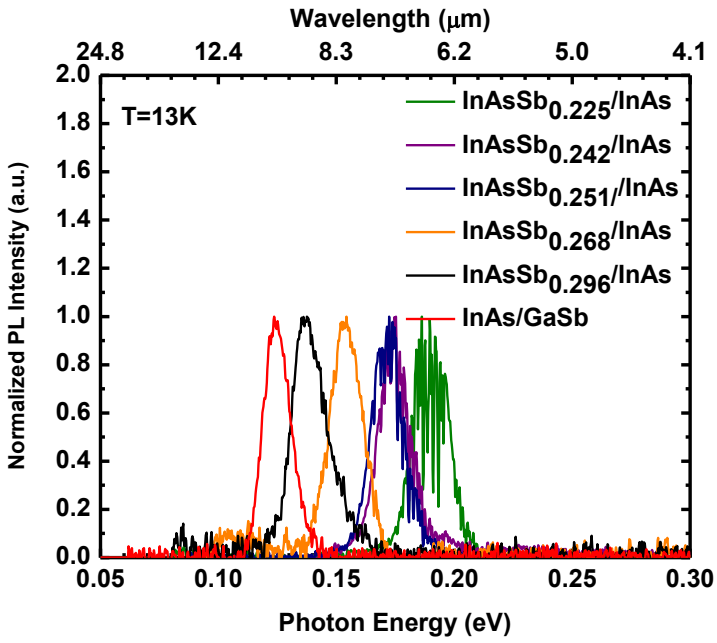

Figure 2.11. The normalized PL spectra of type-II InAsSb/InAs SLS with Sb compositions of 22.5, 24.2, 25.1, 26.8 and 29.6 %, the PL spectrum of LWIR InAs/GaSb SLS from Ref. 20 is also shown. The measurements were performed at T= 13 K with the excitation power of 100 mW.

We can quantify the relative band positions as follows. Considering the relatively low conduction band offsets in InAsSb/InAs SLS structures, high energy states in the conduction band of InAs can be populated with electrons revealing details of the energy structure of the SLS from PL spectra. Experimentally the approach was implemented with higher energy pulsed excitation using the solid-state laser operating in the Q-switched mode. Population of high energy states under pulsed excitation of carriers in $InAs_{1-x}Sb_x$/InAs SLs resulted in broadening of the PL

spectra. Under low excitation, only a single PL peak was observed (Figure 2.12). For InAsSb/InAs SLS structure with 22.5 % Sb the main peak was centered at the photon energy of 0.19 eV and the second peak was observed at 0.25 eV (Figure 2.13a). We associated the second PL peaks with the transitions of electrons from the 3D continuum to quasi 2D hole states in the InAsSb portion of the SLS period. The peak energy differences of 60 meV can be interpreted as the distance from the bottom of the SLS miniband to the bottom of the conduction band in the $InAs_{0.775}Sb_{0.225}$ barriers.

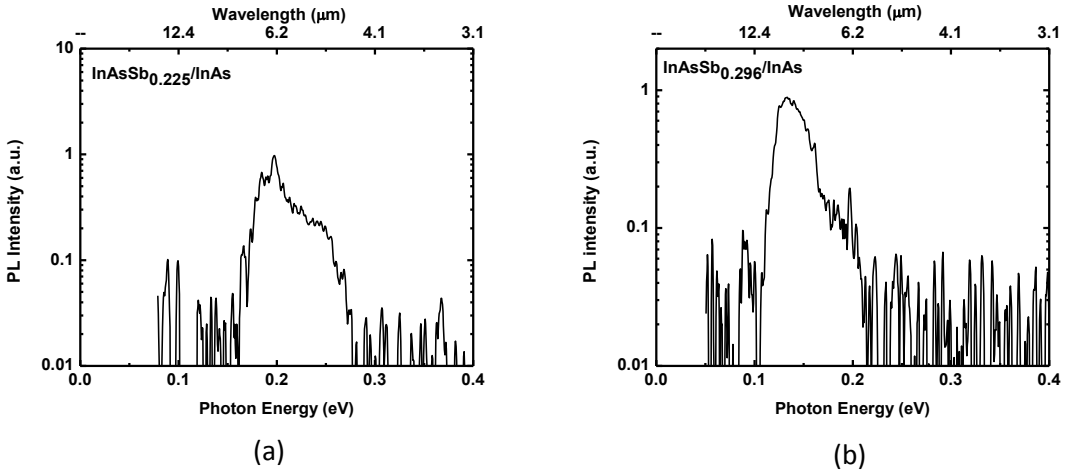

Figure2.12. PL spectra of $InAs_{0.775}Sb_{0.225}$/InAs SLS (a) and $InAs_{0.704}Sb_{0.296}$/InAs SLS (b) under pulsed excitation with the pulse width of 100 ns, the repetition rate of 100 kHz, and the average power of 0.5 W.

The calculation of low-temperature energies was performed with the material parameters recommended in Ref. 37. The energy gap bowing parameter was taken to be 0.87 eV obtained in this work. The stiffness coefficients C11 and C12 as well as the deformation coefficients for the conduction band (ac) and valence band (av and b) for binaries were taken from Ref. 16 for InSb: ac =-6.94 eV, av=-0.36 eV, b=-2.0 eV, C11=684.7 GPa, C12 =373.5 GPa; for InAs: ac=-5.08 eV, av=-1.0 eV, b= -1.8 eV, C11 = 832.9 GPa, C12=452.6 GPa. For a free standing $InAsSb_{0.225}$ with the lattice constant of 6.147 A the following coefficients were obtained by linear interpolation of the data for binaries: ac=-5.5 eV, av=-0.856 eV; b=-1.845 eV,

C11=800 GPa, C12=435 GPa, The in-plane strain in $InAsSb_{0.225}$ grown on GaSb was calculated to be ε=-1.05%.

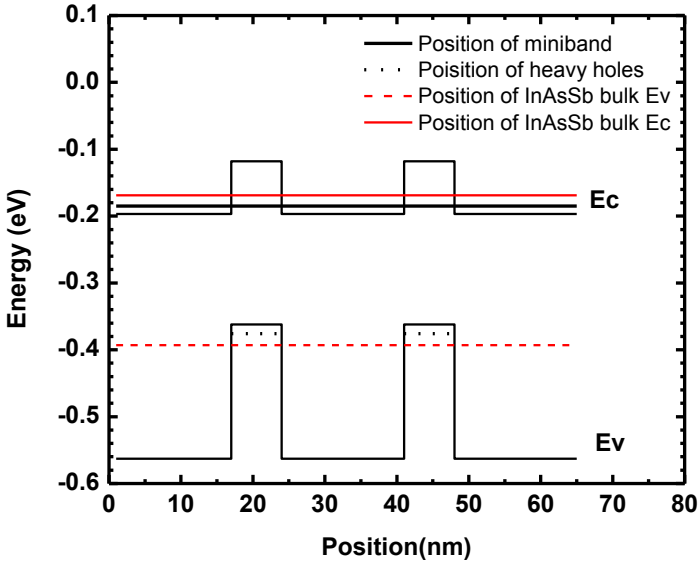

Figure 2.13. The energy band profile of two-period InAs/$InAs_{0.775}Sb_{0.225}$, The black solid line represents the energy position of miniband. The black dot lines represent the energy position of heavy holes. The red lines represent the energy position of conduction band of freestanding $InAs_{0.775}Sb_{0.225}$. The red dot lines represent the energy position of valence band of freestanding $InAs_{0.775}Sb_{0.225}$. The energy position of the miniband was 12 meV above the conduction band of InAs. The energy position of heavy holes was 14 meV below the valence band of $InAs_{0.775}Sb_{0.225}$.

In accordance with Ref. 29, the shifts of the conduction and valence band energies due to hydrostatic strain were calculated as $\delta Hc = 2ac(1-C12/C11)\varepsilon = 51$ meV, $\delta Hv = -2av(1-C12/C11)\varepsilon = -8$ meV, respectively. The split of hole energy into subbands due to the shear strain was found to be $\delta S = b(1+2C12/C11)\varepsilon = 39$ meV. The overall shifts of the heavy and light hole energies were found to be $\delta Ehh = 31$ meV. $\delta Elh = -47$ meV, respectively. The miniband energies in SLs estimated by the 8-band kp method were relatively small playing minor role compared to the effects of strain. First, the valence band energy for InAsSb of a given Sb composition was obtained from a linear interpolation between Ev = -590 meV in InAs and Ev = 0 meV in InSb.

For InAsSb with 22.5 % Sb grown on GaSb， the unstrained valence band energy of Ev =-457 meV was obtained. For the 1.1 % compressive strain in the growth direction calculated for $InAs_{0.775}Sb_{0.225}$ on GaSb, the hole splitting and energy shift would result in the heavy holes energy of Ehh = -426 meV. The hole miniband energy with respect to the edge was estimated to be 14 meV. This resulted in the maximum hole energy in $InAs_{0.775}Sb_{0.225}$ to be Eh = -440 meV. For a free standing InAs the conduction band energy was taken to be Ec = -173 meV. For InAs on GaSb substrate at T=13 K the tensile strain of -0.57 % was obtained. Accounting for strain, it resulted in the electron energy of Ec = -197 meV. The energy of the bottom of the electron miniband was estimated to be 12 meV. The minimum electron energy in InAsSb/InAs SLS was estimated to be Ee = - 185 meV. Thus, the linear interpolation of the valence band energy predicted the SLs energy gap of 255 meV while the experiment suggested Eg of 191 meV. In order to obtain matching with the experiment, a 64 meV difference was added to the valence band energy of $InAs_{0.775}Sb_{0.225}$.

The conduction band energy in $InAs_{0.775}Sb_{0.225}$ was corrected respectively resulting in increase of the conduction band offset. For a free standing material, Ec = -169 meV was obtained. Accounting for strain, it resulted in Ec = -118 meV. Thus, the energy of barrier for electrons was estimated to be 67 meV which is reasonably close to 60 meV obtained from interpretation of the experiment. .

For InAsSb with 29.6 % Sb the electron barrier of 88 meV was predicted. Due to the large value of the barrier, for this structure the second peak in the broadened PL spectra was not observed (Figure 2.12b). For SLs sample with Sb compositions of 25.1 % the shape of broadened PL spectra was influenced by the absorption of vapors in the atmosphere.

The energy estimations summarized above are based on several assumptions which contain uncertainties, such as the position of the InAs Ev relative to that of InSb and the effect of strain. Note for example that the strain effect is entirely responsible for moving the InAsSb bands from a Type I to a Type II-c-line-up with the InAs. In calculations, accumulation of strain in the SLS structures due to strain imbalance was not taken into account.

The obtained results suggest a negative bowing for the valence band energy of InAsSb. Adopting the constant bowing parameter results in the value of -0.3 eV for the valence band for the Sb composition in the range of 20-30 % which is in agreement with the results of Ref. 41. With extrapolation of the dependence to lower Sb compositions a larger bowing parameter would be expected. This observation is in agreement with the results presented in Ref. 43. Extrapolation to larger Sb composition would result in smaller bowing parameters. The latter was confirmed in Ref. 44 in study of the SLS with larger Sb compositions. Assumption of a -0.3 eV valence band bowing leaves the value of +0.57 eV for the bowing parameters in the conduction band.

2.5 Excess carrier lifetime in InAs/InAsSb superlattices

As shown in the previous section, Ga-free SLs has a narrower optical transition energy compared to InAsSb bulk materials. Moreover, the renewed interest in this material system is due to the observation of an order of magnitude greater minority carrier lifetime in undoped InAs/InAsSb SLS compared to that in InAs/GaSb SLs [45,46]. Using this material system a LWIR nBn photodectector was fabricated, with a detectivity D*~10^{10} cm$Hz^{1/2}$/W and a quantum efficiency (QE) of 2.5 % at 77 K with a 13.2 μm cut-off wavelength [47]. The modest QE was attributed to the impeded minority hole transport, which is in turn due to the wide InAs layers and

therefore narrow hole bands. By changing the conductivity type from the natural n-type background doping to moderate p-doping, the photodetector QE should not be limited by minority carrier transport since the electron miniband, unlike the hole band, is sufficiently large. In other words, the origin of low QE in nBn structure in general is due to the low mobility of holes due to its large effective mass.

In this section, carrier recombination in InAs/InAsSb SLS, p-doped to $p=6x10^{16}$ cm^{-3-} and $p=3x10^{17}$ cm^{-3}, is studied. The product of the electron lifetime and background hole concentration at both doping levels was found to be nearly constant. This indicates the minor (if any) contribution of Auger recombination to the electron lifetime at 77K in the studied InAsSb/InAs SLS with mid 10^{17} cm^{-3} doping levels.

All SLS structures were grown in Gen-II MBE system equipped with As and Sb crackers. The growth was performed at substrate temperature of 490C. The growth rate was 1 μm/hour. The InAsSb and InAs layers had the target thicknesses of 173 A˚ and 72 A˚, respectively. The ratio of Sb/As beam equivalent pressures was in the range from 0.13 to 0.16. The InAsSb portions of the SLS period had Sb compositions that were varied in the range from 23.5% to 26.6% by adjusting beam equivalent pressures The SLs region was 1-μm thick. The other characteristics of the samples are summarized in Table 2.1.

The concentrations of free carriers in the p-doped SLS structures were confirmed by time-resolved photoluminescence (TRPL) measurements. The layer thicknesses and Sb-mole fractions were determined from high-resolution x-ray diffraction data. Although the intent was to produce samples with the same bandgap, there were variations in the Sb-mole fraction that correlated approximately linearly with the PL wavelength, as seen in Table 2.1. As and Sb beam equivalent pressure ratios were carefully set before each growth. However, data logging of the chamber

background pressure, which is dominated by As, showed some unintended variations between growths, which correlated linearly with the resulting Sb-mole fraction.

Table 2.1. Summary of sample designs and resulting wavelengths and lifetimes.

Sample	Barriers	P-doping	Sb-x	Lambda (micron)	Tau (ns)	Notation
K1048	No	No	0.235	6.5	450	U1
K1058	Yes	No	0.235	6.5	450	U2
K1225	Yes	6.E+16	0.266	7.7	45	P1
K1226	Yes	3.E+17	0.246	6.9	8	P2

For spectral measurements the photoluminescence (PL) was excited at 1064 nm by a Nd:YAG laser operating in the continuous–wave mode. The excitation area was 0.785 mm^2. The PL spectra were measured with a Nicolet Magna-860 Fourier transform infrared (FTIR) spectrometer, operating in either continuous-scan or step-scan mode with a 14-μm cut-off wavelength external HgCdTe photodetector. The PL kinetics were measured in both time and frequency domains. In the time domain the lifetime was determined from PL decay after a short pulse excitation. In the frequency domain the lifetime was determined from the bandwidth of PL response to a sine-wave modulated continuous-wave excitation. These approaches are referred to as TRPL and optical modulation response (OMR), respectively.`

The TRPL measurements were conducted with excess carriers that were excited by a Q-switched Nd:YAG laser operating at 1064 nm with a repetition rate of 6 kHz and a pulse width of 0.7 ns. The OMR measurements were conducted with excess carriers that were excited with a fiber-coupled diode laser operating at 1.5 μm. In both approaches the PL was collected by reflective optics and detected with a Vigo 10-μm cut-off, HgCdTe detector with a 3 ns time constant. The laser emission

scattered from the sample surface was rejected by a 4.5 μm cut-off wavelength long-pass Ge filter. The sample temperature was stabilized with a closed-cycle He cryostat system from Janis with a M22 cryohead. A ZnSe window was used, which had a coating optimized for high transmission in the LWIR range. Description of the setup for OMR lifetime measurements can be found elsewhere [48].

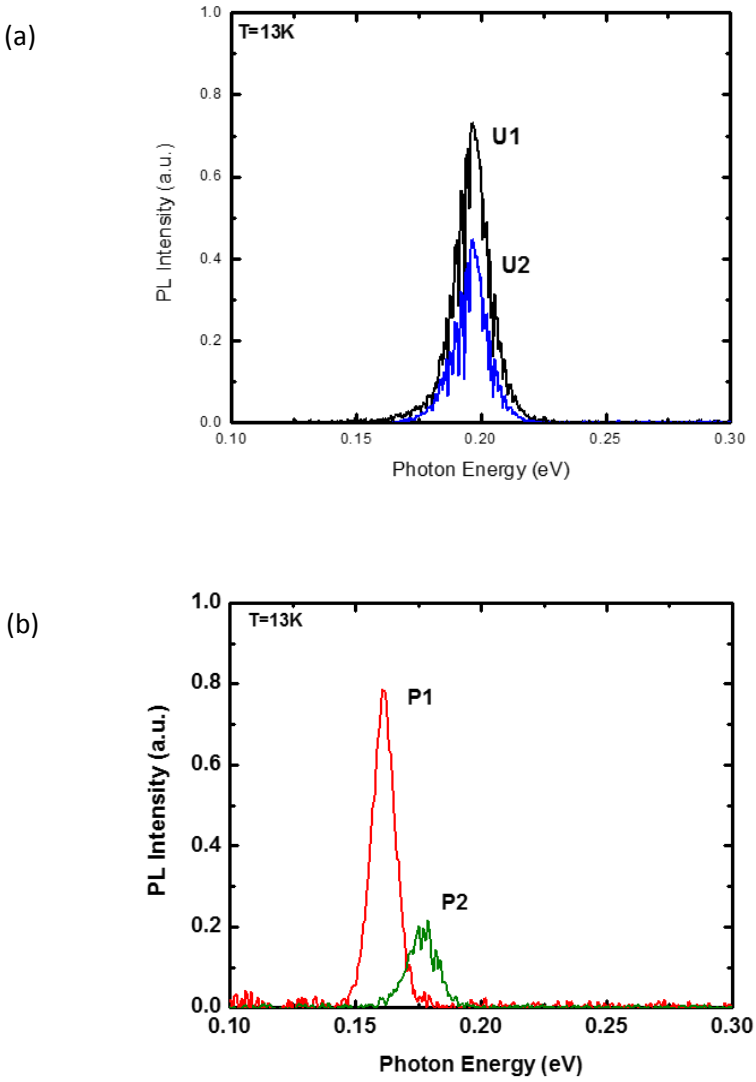

Figure 2.14. The PL spectra of Ga-free SLs at 13 K. (a) Undoped samples with Sb compositions of 23.5% with AlSb cap (blue line), and without AlSb cap (black line). The excitation power was 100 mW. (b) *p*-doped samples with Sb=24.6 % (green line) and 26.3 % (red line). The excitation power was 60 mW.

The PL spectra of the structures with undoped SLs regions measured at T=13 K are shown in Figure 2.14a. The excitation power was 100 mW, which resulted in a power density of 12.7 W/cm^2. This was found to be adequate in previous experiments for determining the energy gap from low temperature PL maxima. The PL intensities were similar, in spite of the lack of AlSb confinement layers for U1. The PL peak energies correspond to a wavelength of 6.5 μm with a full-width at half-maximum of 14 meV, indicating high material quality. The undoped structures have n-type background doping and minority holes are well confined within the InAsSb portions of the SLs cell, which had sufficiently high barriers to impede hole transport. The slightly greater PL intensity for the structure without AlSb confinement layers could be due to different external quantum efficiencies since the carrier lifetimes were found to be identical. The PL spectra for the Be-doped SLS structures are shown in Figure 2.14 (b). The structures were measured with an excitation power of 60 mW and its excitation power density at 7.64 W/cm^2. The PL maxima at T =13 K were found to be at 7.7 and 6.9 μm for structures P1 (Sb composition of 26.3%) and P2 (Sb composition of 24.6%), respectively. The structure with higher Sb composition had a correspondingly longer PL peak wavelength. The FWHM of 11 meV for P1 and 14 meV for P2 are very similar to that for the undoped material shown in Figure 1a. The PL intensity was stronger for the sample with the lower doping level, as expected. The ratio of PL intensities for P1 and P2 was about 5 times, consistent with the ratio of the background doping as expected at low excitation levels.

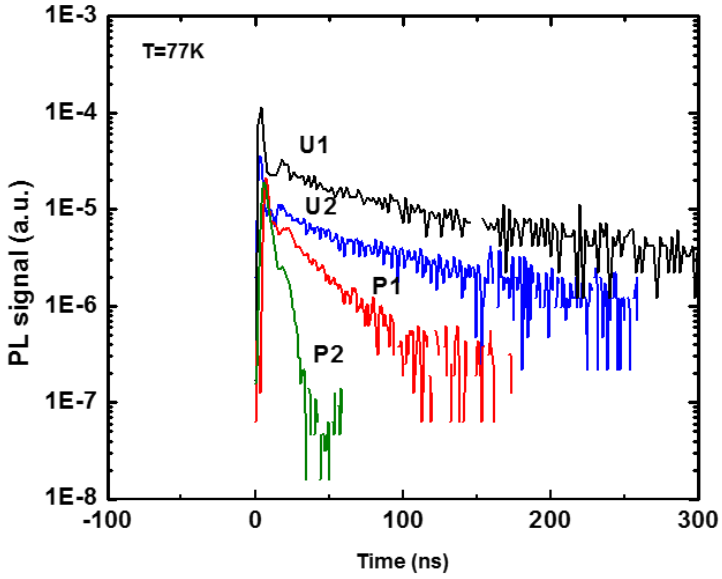

Figure 2.15. The TRPL spectra of Ga-free SLS at 13 K. Undoped samples with Sb compositions of 23.5% with AlSb cap (blue), and without AlSb cap, p-doped samples with Sb=24.6 % (green line) and 26.3 % (red line). The excitation energy per pulse was 15 nJ.

The time-resolved PL decays are shown in Figure 2.15 for all four samples measured at an excitation energy of 15 nJ. For U2, P1, and P2, the initial PL intensities were similar. The PL intensity for U1 was stronger than that for U2 which correlates with spectral measurements shown in Figure 3.21. All PL decays show a rapid response for several ns followed by longer decays which can be fit with by exponential dependence with a time constant. The initial rapid response was attributed to the diffusion of excess carriers over the SLs region, followed by a longer period when the PL intensity is controlled by carrier recombination. The TRPL peak intensity (I_{PLmax}) taken at the beginning of the exponential recombination period was measured in a broad range of pulse excitation energies (Figure 2.16). The dependence of I_{PLmax} versus the pulse excitation energy in double log scale showed an expected change of slope. The PL intensity, I_{PL}, is proportional to the product of the sum of the equilibrium and non-equilibrium hole concentrations ($p+\Delta p$) and the

electron concentrations (Δn), $I_{PL} \propto (p+\Delta p)\,\Delta n$. The region at low excitation energies corresponds to a low injection recombination mode where the concentration of excess electrons is small compared to the background hole concentration ($\Delta n << p$). The region with high excitation energies is attributed to a high injection ($\Delta n >> p$) recombination mode. The transition region between the two recombination modes allowed us to verify the background hole concentration (p) determined from growth calibrations. After accounting for reflection from the sample surface, all photons were considered to be absorbed. The initial excess carrier concentration was calculated from the pulse energy divided by the volume of the excited SLS region. For p-doped samples a homogenous distribution of excess electrons over the recombination period was assumed. The lines approximating low and high recombination modes intersect at (8-9)x10^{16} cm^{-3} for P1 and at (2-3)x10^{17} cm^{-3} for P2 which were fairly close to the design data.

For the TRPL decays shown in Figure 2.15, time constants of 25 and 4.5 ns for structures P1 and P2 were determined from exponential decay, respectively. For sample p1 the PL decay constant was determined to be of 25 ns for excitation level of 15 nJ (λ=1064 nm) per excitation area of 8x10^{-3} cm^2. The initial excess carrier concentration estimated to be above 6x10^{16} cm^{-3}. The experimental PL decays showed the trend of increasing the PL decay time constant with decrease of the excitation. It is reasonable to expect continuing increase of the PL decay constant with further decrease of the excitation. While the peak PL intensities were measured in the excitation range down to 4 nJ, the PL decay constants for excitation energies lower than 15 nJ were not determined because of noise level. In general, the dependence of PL intensity on excess carrier concentration in non-linear, $I(PL) \propto (\Delta n)^k$, with TRPL approach the minority carrier lifetime should be obtained by multiplication of the PL decay constant by coefficient k. Thus, accuracy of

determination of coefficient k limits the accuracy of carrier lifetime measurements by TRPL. The measurements with considerably lower excess carrier concentrations were performed by OMR. Due to considerably lower excitation levels the lifetime data obtained by OMR are considered to be more accurate than data obtained by TRPL

(a)

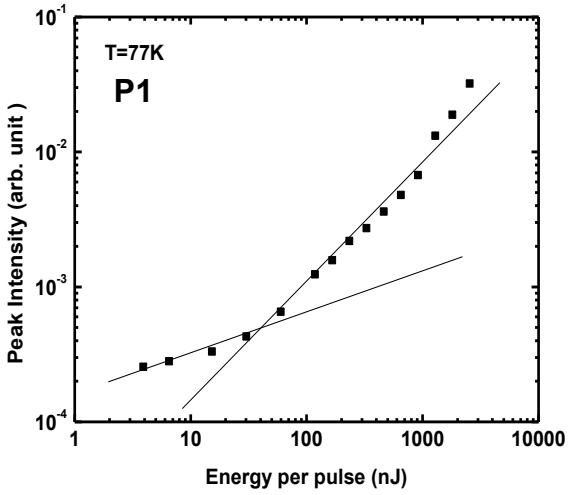

(b)

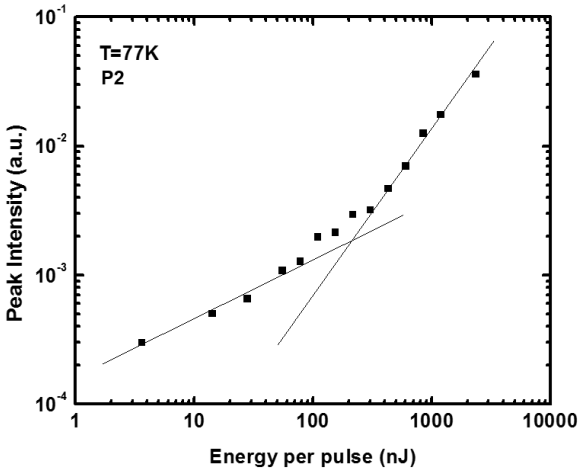

Figure 2.16. The dependences of the TRPL peak intensity on the excess excitation carrier concentration at 77K for (a) the $p=6x10^{16}$ cm^{-3} structure, and (b) the $p=3x10^{17}$ cm^{-3} structure.

The PL responses in the frequency domain measured for the four samples at the same carrier generation rate of $1.27x10^{23}\ s^{-1}cm^{-3}$ at $\lambda = 1.5\ \mu m$ are shown in Figure 2.17 (a). The fitting in Figure 2.17 (a) with a response of a low-pass filter of first order resulted in the carrier lifetime constants of 45 ns and 8 ns, for samples doped at $p=6x10^{16}\ cm^{-3-}$ and $p=3x10^{17}\ cm^{-3}$, respectively. The excess carrier concentration at this excitation level was estimated to be $5.7x10^{15}\ cm^{-3}$. As shown in Figure 2.17 (b) and (c), the PL bandwidth for P1 was found to be independent of excitation at lower excitation power densities. It was concluded that the lowest power density was adequate for determining the minority carrier lifetime in both p-doped samples.

(a)

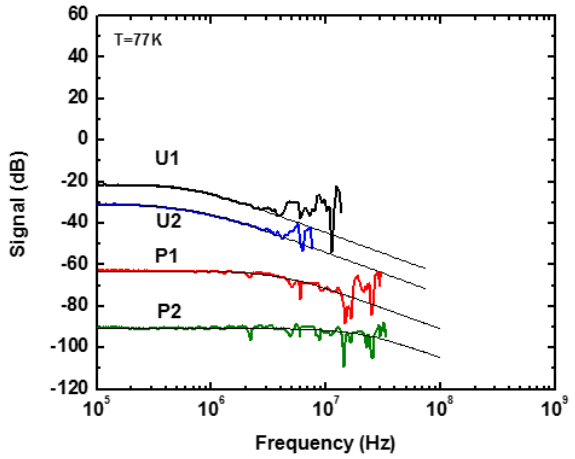

(b)

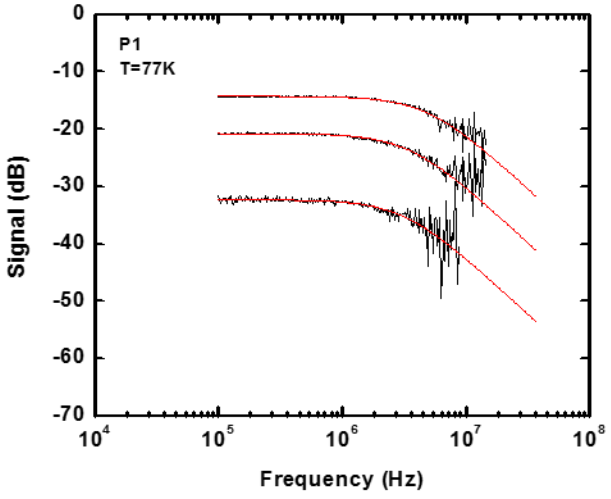

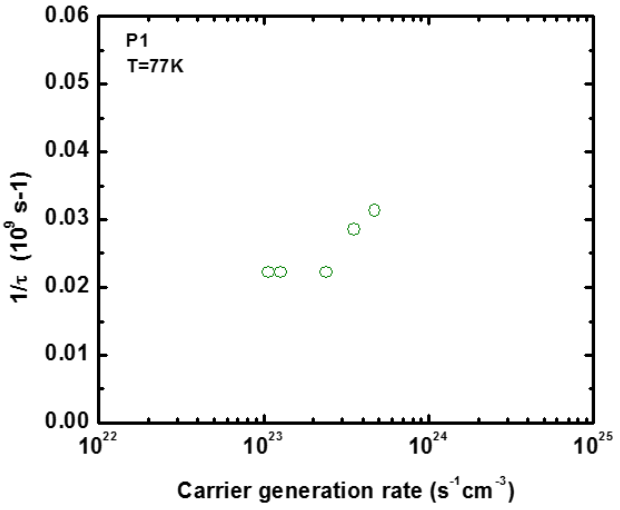

Figure 2.17. The OMR of InAs/InAsSb SLS. (a) Undoped samples with Sb composition of 23.5 % with AlSb barriers (blue line), without AlSb barriers (black line), and p-doped samples with 26.3% Sb (red line), and 24.6% Sb (green line), respectively. The excitation power density was 1.6 W/cm2. (b) The OMR of InAs/InAsSb SLS with Sb composition of 26.3% at different excitation levels (black lines). The red lines show the theoretical response of the low-pass filter of the 1st order. The excitation power densities were 0.7, 0.9, 1.6 W/cm2. (c) The dependence of the PL response time constant on carrier excitation rate.

Due to the use of a lock-in-amplifier with the bandwidth of 1 Hz the noise was considerably reduced, the direct measurements were performed under the excitation power density as low as 1.6 W/cm^2 (λ=1.5 μm) corresponding to the excess carrier concentration about 6x10^{15} cm^{-3}. With OMR approach the PL response signal is proportional to the first power of excess carrier concentration since the harmonics are filtered out by the lock-in-amplifier. Because of the linear relation between the PL response signal and the excess carrier concentration in OMR method, to obtain the carrier lifetime no multiplication of the measured PL time constant by a coefficient is necessary. At the lower end of excess carrier concentration the OMR cut-off frequency was not dependent on excitation. The carrier lifetime was taken as a reciprocal cut-off frequency of modulation response. The accuracy of determination of the PL time constant by modulation technique was limited by the

noise level. For sample p1 with τ =45 ns the fitting accuracy is estimated to be within +/- 1 ns which results in the accuracy of +/- 2%. For sample p2 with τ = 8 ns the fitting becomes non-adequate for 7 and 9 ns, therefore the accuracy of measurements for sample p2 was estimated to be within +/-15 %.

In contrast, for the undoped samples U1 and U2, this power level resulted in underestimated lifetime of 200 ns. However, due to the longer lifetime and stronger PL intensity, the OMR data for undoped samples could be collected at the two orders of magnitude lower excitation level (Figures 2.18 and 2.19). The lowest excess carrier concentration for the direct lifetime measurements was estimated to be $7x10^{14}$ cm^{-3}. At this excitation level the minority carrier lifetime in the undoped samples was found to be independent of excitation. The measurements resulted in the same lifetime constant of 450 ns at T = 77 K for both undoped samples.

(a)

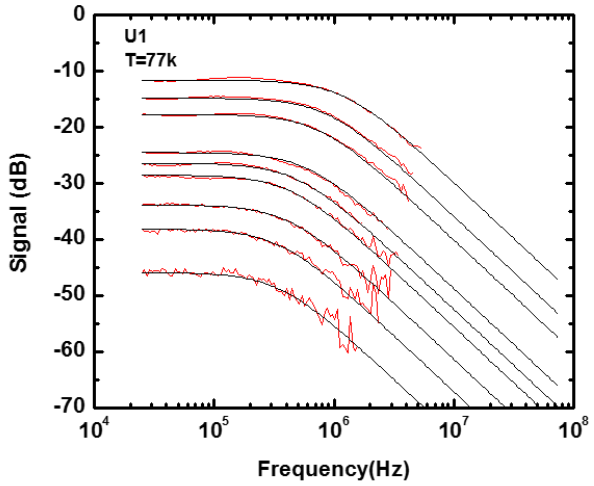

(b)

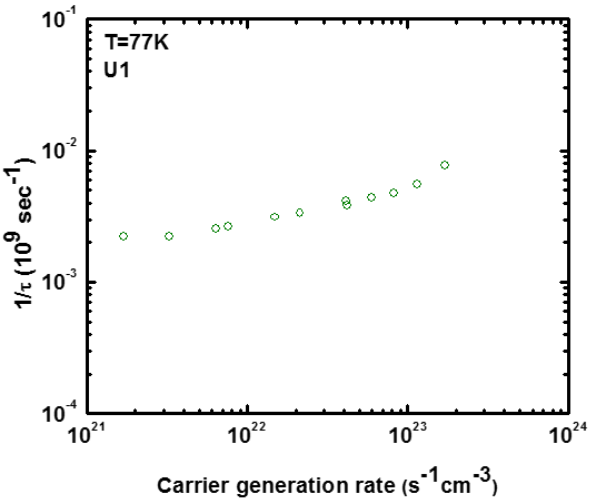

Figure 2.18. (a) The OMR data for the Ga-free SLS with Sb composition of 23.5%, and without a AlSb barrier at different excitation levels (black lines). The red lines show the fit with the response of the 1st order low-pass filter. (b) The dependence of the PL response time constant on carrier excitation rate. The excitation power densities were 0.02, 0.04, 0.08, 0.09, 0.19, 0.27, 0.53, 0.54, 0.75, 1.05, 1.6, 2.2 W/cm^2.

(a)

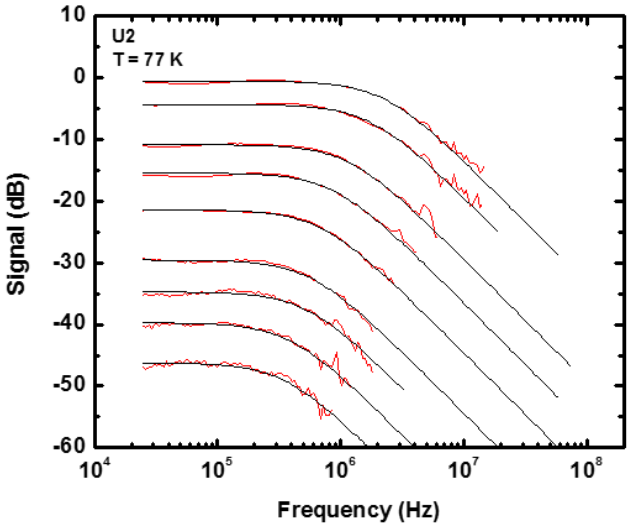

(b)

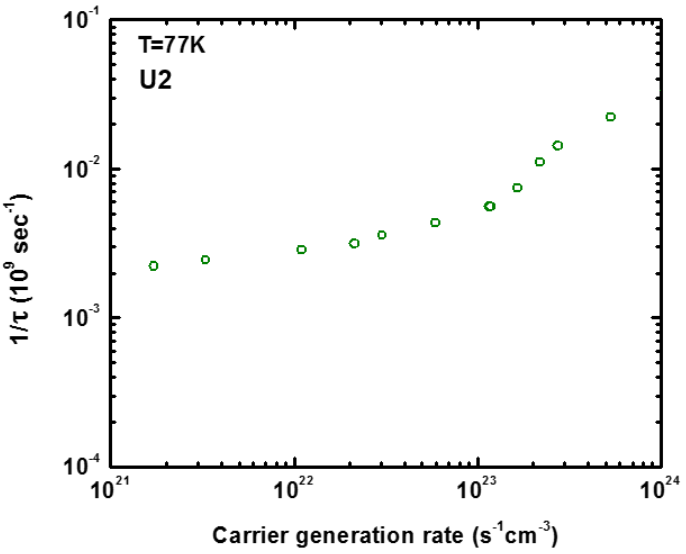

Figure 2.19. (a) The OMR data for InAs/InAsSb SLs with Sb composition of 23.5%, with AlSb cap at different excitation levels (black lines). The red lines show the fit with the response of the 1st order low-pass filter. (b) The dependence of the PL response time constant on carrier excitation rate. The excitation power densities were 0.02, 0.04, 0.14, 0.27, 0.38, 0.75, 1.6, 2.2, 2.8, 3.5, 6.8 W/cm^2.

Electron lifetime values of 45 ns and 8 ns were measured at T =77 K in Ga-free InAs/InAsSb SLS structures, p-doped to the levels of 6x10^{16} cm^{-3} and 3x10^{17} cm^{-3}, respectively. Very good agreement was found between the target doping levels and the numbers derived from TRPL.

The product of the carrier lifetime and the carrier concentration at T =77K was found to be nearly constant, which implies the minor role of Auger recombination in a InAs/InAsSb SLS with energy gap of 0.165 eV and for hole concentrations up to the mid 10^{17} cm^{-3} level. The decrease of the lifetime with doping is likely attributed to an increase of Be-derived Shockley–Read-Hall recombination centers, since the radiative lifetimes are expected to be much longer than the measured data.

In this section we compare InAs/InAsSb and InAs/GaSb SLS structures with similar energy gaps (corresponding to wavelengths around 8 μm) and similar electron lifetimes of 45 ns, and conclude that such lifetimes can be achieved at considerably higher doping concentrations for the Ga-free structure. Specifically, the same lifetime was achieved for doping levels of $6x10^{16}$ cm^{-3} in InAs/InAsSb SLs compared to the reported $1x10^{16}$ cm^{-3} doping level in the InAs/GaSb SLs. This suggests that photodetectors with p-doped InAs/InAsSb absorbers may exhibit lower dark currents due to a smaller diffusion component than those made with InAs/GaSb absorbers.

2.6 Summary

We conclude that growing compositionally graded buffers (Ga(Al)InSb on GaSb substrates) with a strained but unrelaxed top layer allows the fabrication of bulk $InAs_{1-x}Sb_x$ layers (0.5~3 μm thick). The bulk materials have characteristics that are promising for the development of IR detectors operating within the spectral range from 5 to 12 μm. However, the electrical properties such as mobility, effective mass have not been studied thoroughly. Due to the low valance band position of InAsSb, it is difficult to find a material to have a good confinement for holes, which may cause leakage in hole measurement. In such a case, special method would be used to characterize the electrical properties of unrelaxed bulk InAsSb. On the other hand, the further growth optimization is required to obtain thick (> 5 μm) and unrelaxed active layer.

Chapter 3

Heterostructures for photo-detectors based on unrelaxed InAsSb alloys

3.1 Introduction

Efficient photodetectors for the spectral range from 8 μm to 14 μm are required for a variety of applications, such as tele-comunication, IR image sensing, and gas detecting. In the last decades, researchers find out ways to develop the detectors in this region. Quantum well infrared photodetector (QWIP) was developed for the LWIR.[18] It has the advantage of low dark current, and the absorption edge could be tailored accurately by adjusting the thickness of the quantum well. However, QWIP was limited by operation temperature, and the cooling system. Also due to the quantum mechanics selection rules, the absorption of QWIP is low compared with bulk materials as discussed in introduction. As one of the competitors, HgCdTe based photodetector is suitable for LWIR detection. [49] Since it is bulk materials, the absorption coefficient is quite larger than that of QWIP. By tuning the Te composition, the bandgap could be narrowed down below 0.1 eV. However, the weakness of HgCdTe is the inhomogeneous of the materials, which results in big bandgap fluctuation. It is quiet demanding on the materials quality, which increases profit of the devices. Recently, the GaSb/InAs SLs was demonstrated to have a type-II band alignment. By adjusting layer thickness, the bandgap of SLs could be extended below 0.04 eV. [50]. However, in tradition pin design, type ii superlattice was still limited by SRH recombination, which is proportional to the band gap. Especially for naroow band gap materials, the dark current in pin photodiode is quiet high, showing G-R limited recombination. [51]

With the demonstrated advantage of the barrier detectors [52-53], the mid-wave infrared detector industry's interest has turned toward heterostructure detectors with bulk InAsSb absorbers and AlSb-based barriers. These structures can outperform InSb homojunction photodetectors operating at elevated temperatures. Compared with LWIR InAs/GaSb SLs, undoped InAsSb bulk materials have a longer minority carrier lifetime [54]. In addition, bulk materials have higher absorption coefficients, resulting in higher quantum efficiency. Therefore, InAsSb-based materials are also gaining attention for the development of long-wave infrared (LWIR) photodetectors [55-56].

In this chapter, the operation principles of nBn detectors would be introduced as well as the fabrication procedure of the InAsSb based nBn heterostructures. The performance of nBn detector with cutoff 10 μm will be discussed. The role of AlIn(As)Sb barrier was investigated. In order to obtain, larger quantum efficiency, the InAsSb0.5 based detectors with thicker active layers were grown. It showed that QE increased with the thickness of active layers, demonstrating that the diffusion length might be more than 3 um. To optimize the dark current, structures with different doping profiles will be discussed. A new method to characterize the mobility, and lifetime of the LWIR materials will be introduced. The lifetime of different doping levels will be investigated. It shows a compatible value compared with HgCdTe in terms of Auger recombination coefficient.

3.2 Design and fabrication of barrier detectors based on InAsSb alloys

As shown in Figure 3.1, the nBn heterostructure consists of 3 components, namely the active layer, the undoped barrier, and the contact layer. Different from conventional pin photodiode, [57] where the bias is applied on active layer, the bias

is mainly applied on the barrier layer in nBn heterostructures. The band structure resembles to that of MOSFET. Once the gate for minority holes is open, the photo-generated carriers could diffuse to the contact layers. Compared with conventional pin photodetectors, the advantage of nBn heterostructure lies in reduction of dark current especially for active layer with narrow bandgap materials. For the pin photodiode, the dominant mechanism of dark current comes from generation-recombination (G-R) current, due to the different quasi-fermi level of electrons and holes. [58] The G-R current density in the depletion region could be expressed as:

$$J_{GR} = \frac{qWn_i}{2\tau}, \tag{3.1}$$

where the W is the depletion with, ni is the intrinsic carrier concentration and τ is the lifetime of carriers. The intrinsic carrier concentration is proportional to exp(-Eg/2kT), making GR dark current sensitive to temperature in narrow gap materials. On the contrary, for nBn photodiode, since most of the voltage is applied wide band gap materials (barrier layer), the dominant dark current comes from diffusion current from the active layer, which could be expressed as:

$$J_{diff} = \frac{qWn_i^2}{N\tau}, \tag{3.2}$$

where W is the thickness of active layer, N is the background concentration of majority carriers, and τ is lifetime of minority carriers. The square of intrinsic carrier is proportional to exp(-Eg/kT). Compared with GR current, the diffusion-dominant mechanism results in significantly reduction of dark current at low temperatures. In addition, the tunneling current also contributes when voltage is applied on active layer. [rogalski's book] It could be effectively suppressed in nBn heterostructures where only small portion of active layer is depleted. In the following sections, methods to suppress the depletion region in nBn heterostructure will be discussed.

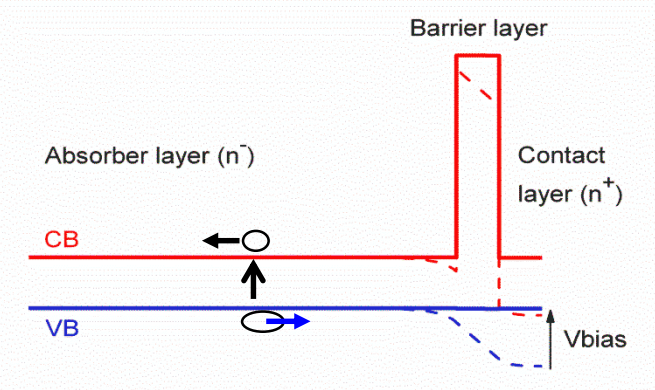

Figure 3.1. The schematic energy band diagram of nBn heterostructures. The conduction band is shown in red, and valance band is plotted in blue. The flat band condition is shown in solid line, and the condition without bias is plotted in dash line.

As was shown in prevision sections, the nBn heterostructures require a electron barrier, whose conduction band offset should be ~ 1 eV higher than that of active layer, so that the majority carriers could be effectively impeded. In the InAsSb materials system, AlIn(As)Sb is suitable for the design, meanwhile its lattice constant could be tuned to be lattice matched to that of virtual substrate. In the actual design, an unstrained and unrelaxed $InAs_{0.6}Sb_{0.4}$ 1-um-thick bulk layer was gown by MBE on a 3 um thick GaInSb compositionally graded buffer layer and a 500 nm $Ga_{0.66}In_{0.34}Sb$ virtual substrate. We utilized this layer as the absorber section of the barrier photodetector. This nominally undoped alloy section demonstrated an absorption edge near 9.5 μm at 77K. Figure 3.2(a) is a schematic band diagram of the barrier photodetector heterostructure under flat band condition. The InAsSb absorber was grown undoped. Our assumption about the n-type of InAsSb is based on its similarity to InAs. The background electron concentration in this layer cannot be high (probably below 10^{16} cm^{-3}) since we did not observe the Burstein-Moss shift between the detector cut-off wavelength and the low energy edge of the photoluminescence spectra of the absorber. For the barrier layer we selected an

$Al_{0.6}In_{0.4}As_{0.1}Sb$ alloy that was lattice matched to $InAs_{0.6}Sb_{0.4}$. The calculation predicted that the large band offset in conduction band between the InAsSb absorber and the AlInSb barrier should suppress the electron transport from the absorber to the n InAsSb contact layer.

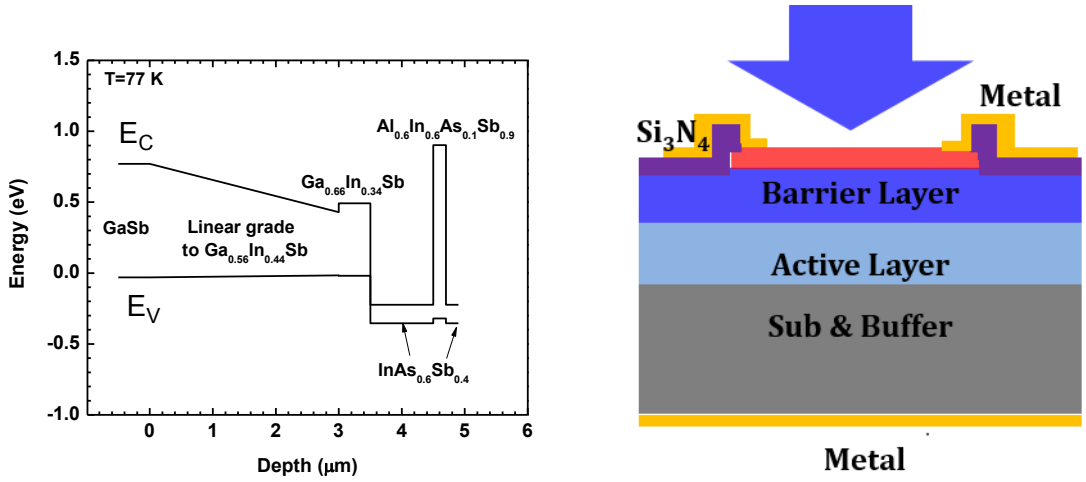

(a) (b)

Figure 3.2. (a) The schematic band diagram for the heterostructure with a bulk InAsSb absorber with 44 % of Sb composition. The AlInSb barrier was lattice-matched to the InAsSb absorber layer. The top contact layer was doped with Tellurium to a level of n= 1×10^{18} cm^{-3}. (b) The schematic cross-section of the processed heterostructures for LWIR detector with top illumination.

The valence band edges can be expected to be nearly aligned between InAsSb and AlInSb; hence, the photo and thermally generated holes can reach the top contact.

The wafers were processed into front side illuminated devices (Figure 3.2(b)). We used an inductively coupled H2/CH4/Ar plasma reactive ion etching process to define the top contacts into square mesas with sides 300 um. A silicon nitride mask was used for mesa definition, and the etching process was stopped in the top half of the barrier layer as confirmed by the Scanning Electron Microscopy (SEM). The mesas were covered by a 300-nm-thick silicon nitride layer followed by the

deposition of Ti/Pt/Au contacts. Square optical windows with sides of 250 um were opened on the front side on mesas with side lengths of 300 um, respectively. The external quantum efficiency (EQE) was measured with illumination from the epi-side. No antireflection coating was applied. The backside contact consisted of an annealed Ni/Au/Ge/Ni/Au layer and a Ti/Pt/a) Au final metallization.

3.3 Heterostructures with quaternary barriers

The nBn requires negative DC bias applied to the top of the epi-layer contact to suppress the AlInAsSb barrier for holes. The QE was increasing with bias until it reaches a constant level for a bias of -0.4 V. The QE spectra in Figure 3.3 (a). are presented for the bias voltage of - 0.4 V for the temperatures from 80 to 150 K. The distortion of the QE spectra between $\lambda = 5.5$ and 8 μm are explained by atmospheric absorption. The QE increases monotonically with photon energy from $\lambda = 10$ μm at T = 80 K and from $\lambda = 11$ μm at T = 150 K. The absolute values of QE in the long wave infrared range are relatively high considering the incomplete absorption in the relatively thin absorber. An increase of QE with temperature from T= 80 to 150 K at a particular wavelength is likely due to the red shift of the energy gap with temperature. It showed that the carrier lifetime is not limited by Auger recombination, in addition the diffusion length is sufficiently large compared to the absorber thickness and the QE is not limited by hole transport. It was concluded that QE for the long-wave infrared photodetectors based on the bulk InAsSb layers should benefit from an increase of the absorber thickness.

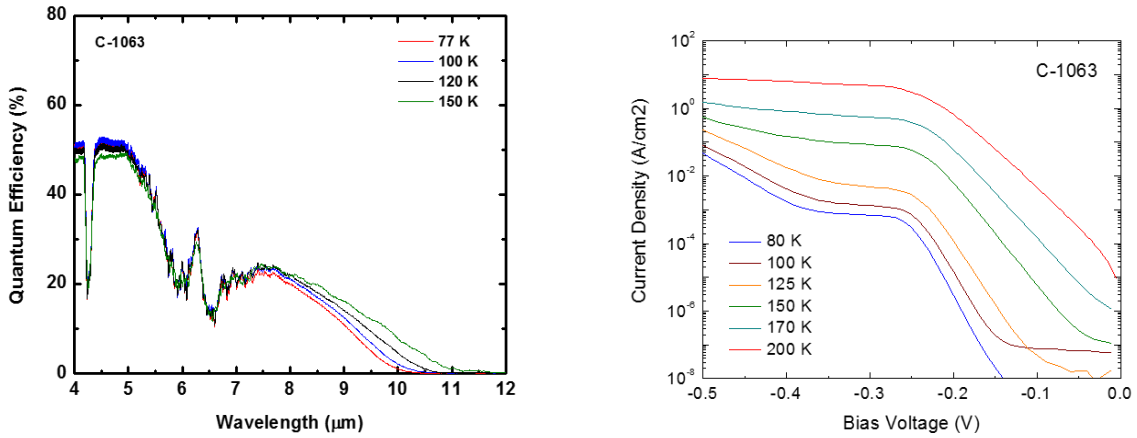

(a) (b)

Figure 3.3. The spectra of external quantum efficiency obtained for the heterostructures with a 1-μm-thick InAsSb layers with Sb composition of 40 % at the temperatures of 77 K, 100 K, 120 K, and 150 K, respectively. (b). The IV characteristics obtained for heterostructures with a 1-μm-thick InAsSb layers with Sb composition of 40 % at different temperatures ranging from 80 K to 200 K.

The IV characteristics of InAsSb heterostrucutres measured from 80 K to 200 K under dark conditions are shown in Figure 33 (b). The bias was defined with respect to top epi-layer contact. The IV characteristics show that the dark current was nearly constant from -0.25 V to -0.4 V, in which region the QE increases and saturates. This could be explained by the dark current being diffusion limited. Once the barrier for minority holes was suppressed, holes in the active layer could diffuse to the top contact. This IV behavior is a little bit different from what we observed before [55]. In the previous case, the current didn't show such saturation behavior, maybe it is due to the fact that there is a still remaining band valance band offset between InAsSb and AlInSb, so some bias may drop in this inter-face resulting in depletion region in the active region. It also indicates good valance band alignment between the absorber and barrier layer, by using the AlInAsSb barrier layer, which lowed the valance band.

We can conclude that the barrier heterostructures with a 1-µm-thick bulk InAsSb0.4 layer showed adequate light absorption and transport of minority holes across the absorber. The QE should benefit from increased absorber layer thicknesses. In order to prove that and get larger quantum efficiency, similar heterostructures with thicker InAsSb0.5 absorber layer were grown and fabricated. Figure 3.4 shows QE measurements for different active layer thickness at 77K. With a $InAsSb_{0.5}$ absorber layer, the cutoff wavelength extends to 11 µm for all three devices. QE at 8 µm increases from 23% to 39%, with the absorber thickness increasing from 1 µm to 3 µm. We assume the photo-generated carriers in the active layer were proportional to I_0 (1-exp(-αL), where I_0 is the incident light intensity, α is the absorption coefficient at certain wavelength, and L is the thickness of active layer. The data presented indicates an absorption coefficient of 3000 cm-1 at λ= 8 µm. Meanwhile it shows that the diffusion length is larger than 3 µm, and the InAsSb based LWIR detector could potentially have increased QE for thicker absorber layers.

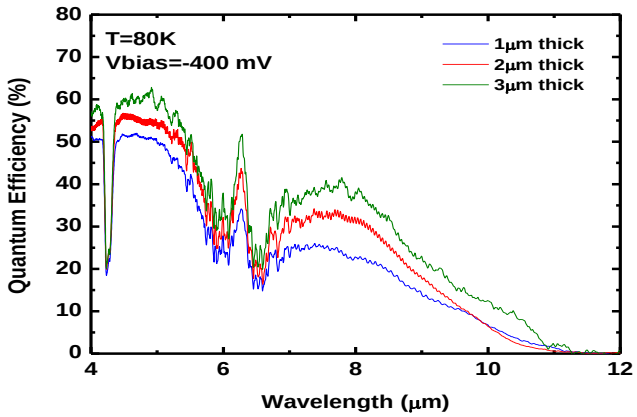

Figure 3.4. The spectra of external quantum efficiency obtained for the heterostructures of $InAsSb_{0.5}$ layers at 77 K with different active layer thickness. 1 µm (blue line), 2 µm (red line), 3 µm (green line).

The characterization data obtained for unoptimized heterostructures suggests sufficiently large absorption and carrier lifetimes (long diffusion length) suitable for

the development of infrared. The carrier transport, including the transport of minority holes, is adequate for the development of detectors and emitters with increased active layer thickness.

3.4 Effect of active layer doping

The dark current shown in undoped active layer from previous section is around 1e-3 A/cm^2 at V=-0.4 V. Assuming dark current is diffusion limited, the minority carrier concentration is in the level of 10^{13} cm^{-2}, which is way too far from reasonable value. It implies that the dark current is not diffusion limited. It contains the contribution from GR and tunneling. In order to decrease the dark current, several optimization schemes are tried. Among them, the doping in the active layer effectively reduce the dark current. In the rest of this section, the performance of 1e16 cm^{-3} n-type doped active layer will be shown. And from the comparison with undoped structure, the mechanism to suppress depletion will be discussed.

The heterostructure consisted of the following sequence of layers: a 3-μm-thick GaInSb buffer with the In composition linearly graded from 0 to 44 %, a 200-nm-thick GaInSb virtual substrate with 34 % In composition (unstrained layer), a 1-□m-thick InAsSb0.4 absorber, a 20-nm-thick AlIn0.4As0.1Sb barrier and a 20-nm InAsSb0.4 top contact layer. The buffer, the virtual substrate and the top contact layers were Te-doped to a level of 10^{18} cm^{-3}. The AlInAsSb barrier was undoped. Another heterostructure was grown with an undoped absorber. For similarly grown undoped InAsSb with 40 % Sb, a background electron concentration of 1.5*10^{15} cm^{-3} was reported in [59]. Another heterostructure was grown with the absorber doped with Tellurium to a nominal level of 1016 cm-3.The wafer were processed in the same way as shown in previous section.

(a)

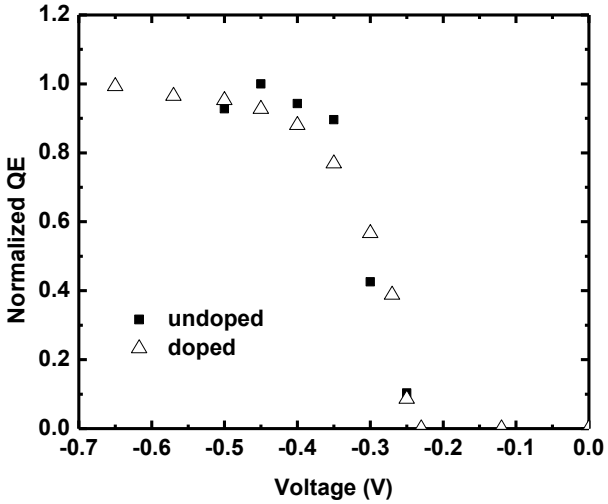

(b)

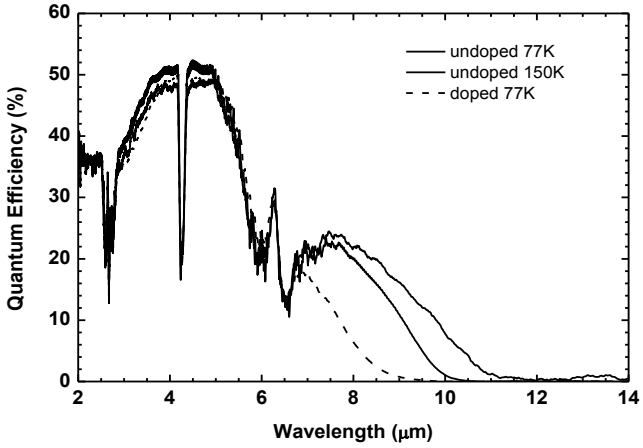

Figure 3.5. (a) Dependences of the integrated QE on bias voltage for the nBn photodetectors with undoped and doped $InAsSb_{0.4}$ absorbers at T = 77 K; (b) The QE spectra for the nBn photodetectors with undoped absorber at T = 77 K and 150 K (solid and dotted lines, respectively) and for one with doped absorber at T = 77 K (dashed line). The spectra were measured at the bias voltage of - 0.4V.

The nBn devices operated with a negative DC bias necessary for suppression of the barrier for minority hole transport to the top contact. Figure 3.5 (a) shows the dependences of the QE on bias for the devices with undoped and doped absorber regions. For all devices a rapid increase of the QE with bias was observed in the range from -0.25 to -0.4 V. The measurements of QE spectra were conducted for the

top-side illuminated devices at a bias voltage of -0.4 V with a spectral resolution of 4 cm-1 (Figure 3.5 (b)). For the long wavelength emission the heavily doped top contact was essentially transparent. From the long wavelength side the QE increased monotonically with photon energy up to 0.3 eV (λ = 4 μm). The distortions in the region between λ = 5.5 and 7.5 μm resulted from averaging the peaks of atmospheric absorption. The red shift of the QE edge from λ = 10 μm at T = 77 K to λ = 11 μm at T = 150 K is explained by the decrease of the energy gap of InAsSb with temperature and consistent with the Varshni parameters determined in Chapter 2. The absorber doping resulted in a blue shift of the QE edge from λ = 10 μm to 8.3 μm at T = 77 K. Considering reflection losses from the surface of the uncoated devices, and using the absorption coefficient estimate of 1.5*104 cm-1, and a 50 % QE in the range λ = 4 - 5 μm we find that most of the excess holes generated at T= 77 – 150 K in the 1 μm thick absorber reached the contacts. Therefore, we conclude that the minority hole lifetime in InAsSb0.4 was significantly greater than the hole transport time across the device in the temperature range up to 150 K and with n-doping of the absorber up to the level of 10^{16} cm^{-3}. A 22 % QE at λ = 8 μm for 1-μm thick InAsSb0.4 implies an absorption coefficient of $3*10^3$ cm-1, consistent with available experimental data.

No contribution of the surface leakage current was observed as the dark current was scaled with the mesa area. The dependences of the dark current density on voltage for the devices with undoped and doped absorbers are shown in Figures 6a and 6b, respectively. A rapid increase of current in the range of -0.15 - -0.25 V was attributed to suppression of the barrier for minority holes due to the difference in doping levels between the absorber and the contact regions. As mentioned, the QE data suggested that most minority holes were collected by the contact at the bias

voltage of -0.4 V. At this bias the devices with undoped and doped absorbers showed dark current densities of 10^{-3} and 10^{-5} A/cm^2, respectively.

(a)

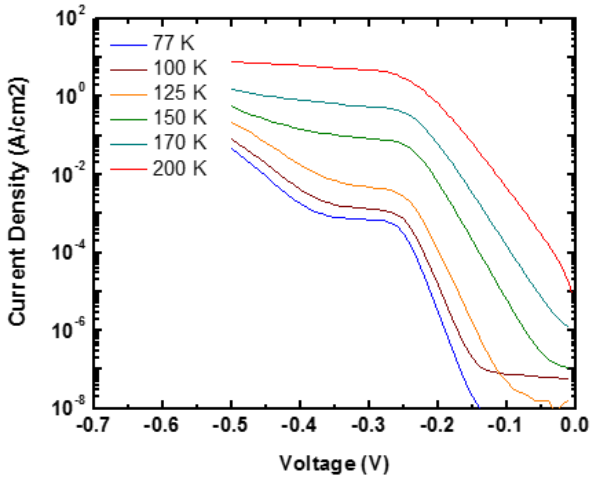

(b)

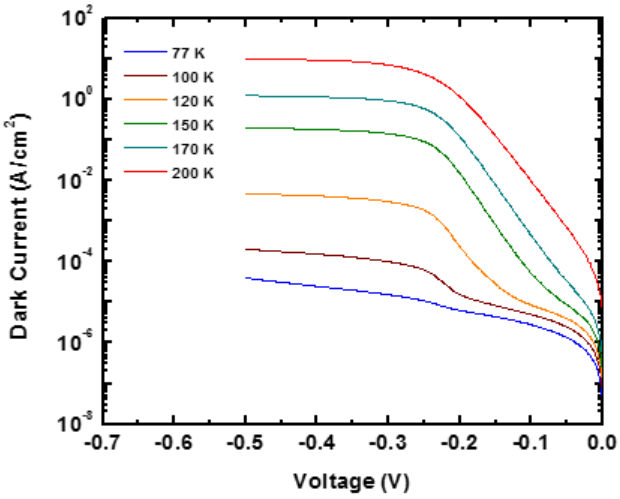

Figure 3.6. The current-voltage characteristics of the nBn devices with undoped (a) and doped (b) InAsSb0.4 absorbers at different temperatures.

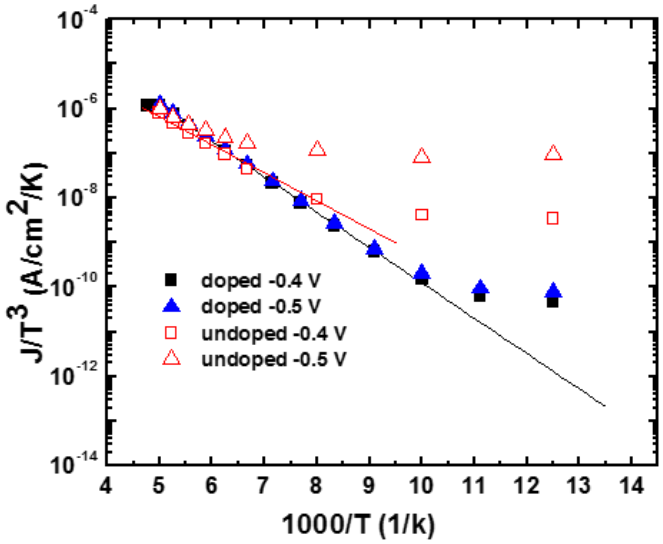

Figure 3.6. (c) The temperature dependences of the dark current densities taken at a bias voltage of -0.4 V and -0.5 V for undoped and doped devices respectively.

Figure 3.6c shows the temperature dependences of the dark current for both devices at the bias voltages of -0.4 and -0.5 V. The pre-factor T^3 accounts for temperature dependence of the density of states. Once can see that for the devices with undoped absorbers the dark current increases with changes of the bias voltage from -0.4 to -0.5 V. Such behavior can be explained by depletion of a considerable part of the absorber adjacent to the barrier which leads to domination of the generation-recombination (G-R) and perhaps tunneling components at T= 77 K. The depletion of the absorber resulted from the high bias necessary for suppression of the barrier for hole transport due to the valence band offset at the interface of the absorber and the barrier. At T=200 K the dark current in the device with the undoped absorber was dominated by diffusion as the relative change of the current with bias was small. For the devices with the doped absorber the width of the depleted region was significantly reduced which resulted in independence of the dark current on bias in the temperature range above T= 110 K. The activation energy of 153 meV

determined from the slope in the temperature range T= 110-200 K is comparable to the energy gap. The difference can be explained by population of states in the conduction band with doping and the band non-parabolicity. Accounting for the latter was beyond the scope of this work.

It should be noted that in the devices cooled to T =77 K the actual photocurrent was significantly greater than the dark current due to exposure to both room temperature background illumination and the attenuated laser emission. Under the experimental conditions the photocurrent was independent of bias and therefore exhibited the diffusion behavior. Thus, the vertical hole transport in both transient and frequency response measurements was dominated by diffusion.

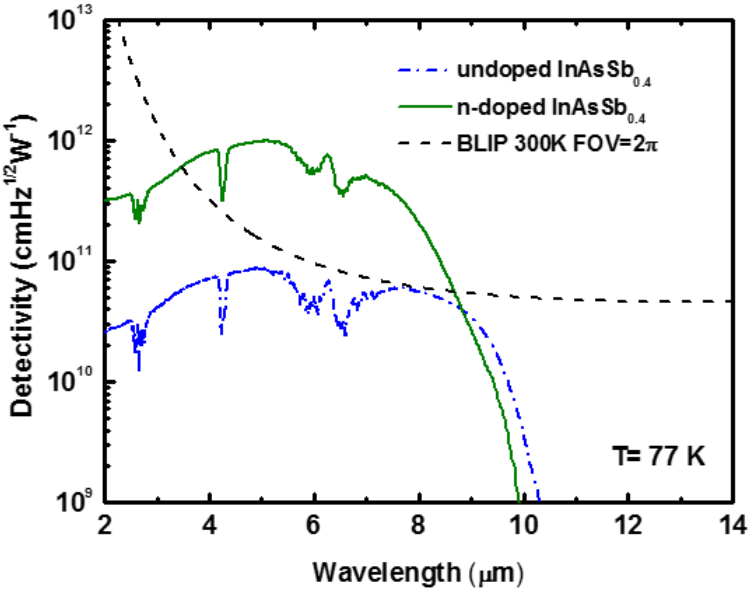

Figure 3.7. The specific detectivity spectra of the barrier detectors with 1-μm-thick $InAsSb_{0.4}$ absorbers at T = 77 K Solid and dashed lines correspond to the devices with doped and undoped absorbers, respectively. The dotted line shows the 300 K background limit for a 2π acceptance angle.

For assessment of the material properties related to infrared detection, the specific detectivity spectra (Figure 6) were calculated for both devices at T =77 K with the following equation [60].

$$D^* = (e\lambda/hc\ QE)/\sqrt{(2eJ + 4k_BT/RA)}\ , \qquad (3.3)$$

The dark current and the differential resistance were taken at a bias of -0.4 V. The non-optimized devices with 1-m-thick absorbers showed a performance exceeding the 300 K background limit in a 2π acceptance angle [60] and demonstrated a D* = $2*10^{11}$ cm/$Hz^{1/2}$/W at $\lambda = 8$ μm in spite of the significant blue shift of the absorption edge with doping. For the doped structure, the temperature dependence of detectivity spectra is plotted in Figure 3.8. It shows that the device has BLIP at least up to 100 K. Further optimization is required to improve the performance of device in even higher temperatures.

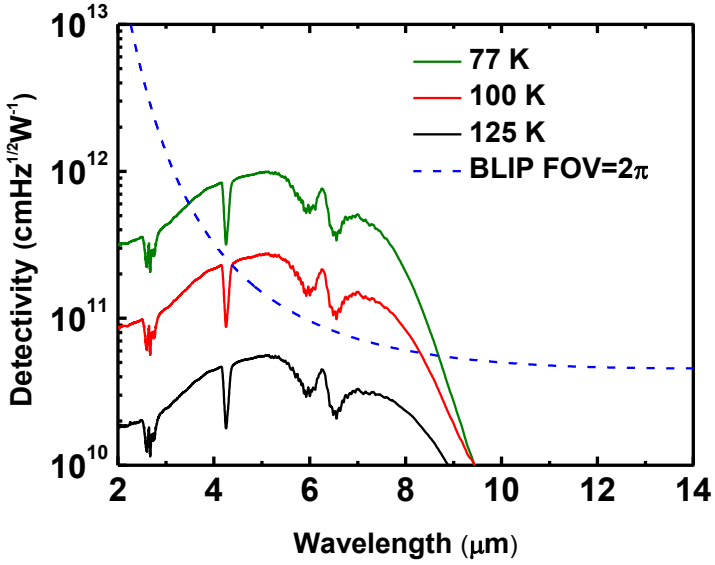

Figure 3.8. The specific detectivity spectra of 1e16 doped structure at different temperatures, and the comparison with background limited performance (blue dotted line).

3.5 Transient Response of InAsSb barrier heterostructures

The carrier lifetime in the absorber materials was determined using specially grown epitaxial structures containing barriers for carrier confinement.As mentioned in the previous section, the nBn structure has no depletion region in the active layer. In this case, the absence of the depletion region in the absorber allows obtaining the minority carrier lifetime and mobility in the isotropic narrow gap absorbers from the direct measurements of the detector transient response. In this section we characterize the LWIR nBn photodetectors consisted of bulk unrelaxed InAsSb absorbers with 40 % Sb composition, the lattice-matched AlInAsSb barriers with 10 % As composition followed by Te-doped InAsSb contact layer. The lattice constant difference between the bulk InAsSb and GaSb substrate was accommodated with compositionally-graded GaInSb buffer. The device I-V characteristics contained a region with a nearly constant current indicating that in this range of bias voltages the absorber had no area impeding the hole transport as mentioned in the previous section.

The diffusion length of minority holes was measured using the set of structures with various contact areas. The absorber was illuminated through the substrate. The illuminated area exceeded the contact area. The photo-generated carriers were collected by the contacts due to both vertical hole transport and the lateral diffusion of holes along the isotropic absorber layer. Since the absorber thickness was small compared to the diffusion length, the component of the detector time response caused by lateral carrier transport was slower compared to the transition time of holes in the vertical direction. The time response due to the lateral component was used to determine the minority hole lifetime. The hole mobility was calculated from the diffusion length and the carrier lifetime.

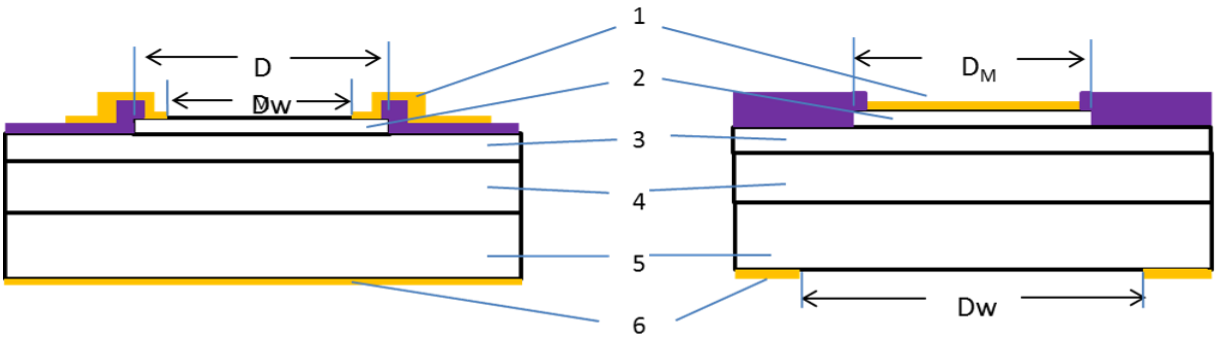

Figure 3.9. (a) The schematic presentation of the structure epi-side illuminated detectors. (b) The schematic presentation of the back-side illuminated detectors structure. DW and DM are the optical window and contact sizes, respectively. 1- top metal contact, 2- mesa contact layer, 3- barrier, 4- absorber, 5- substrate, 6- backside metal contact.

The structure discussed here was exactly the same as previous section, but it was fabricated into back illumination devices so that we could investigate the behavior of lateral diffusion. The heterostructure was processed into the epi-side (Figure 3.9a) and the back-side (Figure 3.9b) illuminated devices. The contacts of square shape were etched to the barrier layer. The processing procedure was identical to that described in previous section. Quantum Efficiency (QE), dark current and frequency response were measured for the epi-side illuminated devices. The contact and window dimensions were DM=300 μm and DW=250 μm, respectively. Diffusion length and lifetime of minority carriers were determined from the transient response of the back-side illuminated devices. The contact dimensions were DM= 50, 100, 150, 200, and 500 μm. The optical window was DW= 500μm for all back-side illuminated devices.

The device responses in domains was measured with λ=3.2 μm InGaAsSb/AlInGaAsSb/GaSb type-I quantum well diode laser. The light absorption in the buffer and virtual substrate layers was insufficient. From the direct

transparency measurements the absorption coefficient of the absorber was found to be 13,000 cm-1 at λ=3.2 μm. It suggests that most of the excess holes were generated in the absorber region for both epi-side and back-side illuminated devices.

The time responses of the devices were measured at the trailing edge of the laser pulse. The laser was biased near the threshold. The modulation pulses had the fall time of 5 ns, the pulse width of 50 μs and the repetition rate of 10 kHz. The devices were loaded with 50 Ohm. The preamplifier bandwidth was 80 MHz. The frequency responses were measured with a sinwave-modulated excitation. The laser modulation bandwidth was determined to be 90 MHz.

The transient responses were measured under the bias voltage of -0.4 V. Figure 3.10a shows the transient responses of the backside illuminated devices at T=77 K. Each response consisted of a fast component (F) of the amplitude followed the system response and a slow component (S). The fast component resulted from the collection of minority holes generated in the absorber area under the contact. The slow component was attributed to collection of minority holes around of the contact perimeter from the area limited by the minority carrier diffusion length. Figure 3.10b shows that with change of the contact side DM, the fast and slow components were scaled as the second and the first power of DM, respectively. The contributions of two components to the response become equal at $D_M = 4L_D$. The hole diffusion length determined from the intersection point of these dependences was found to be L_D= 9 μm.

(a)

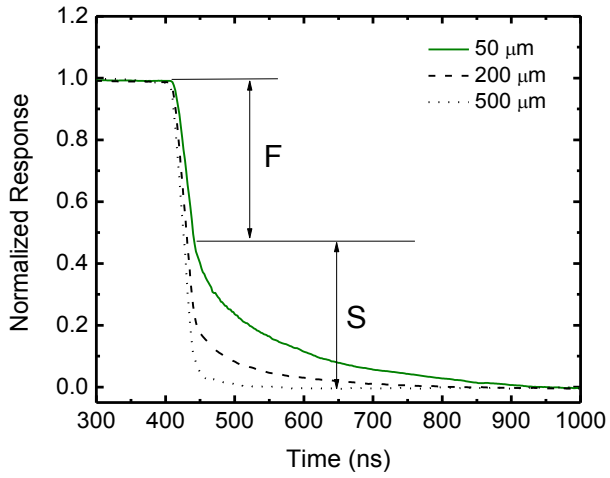

(b)

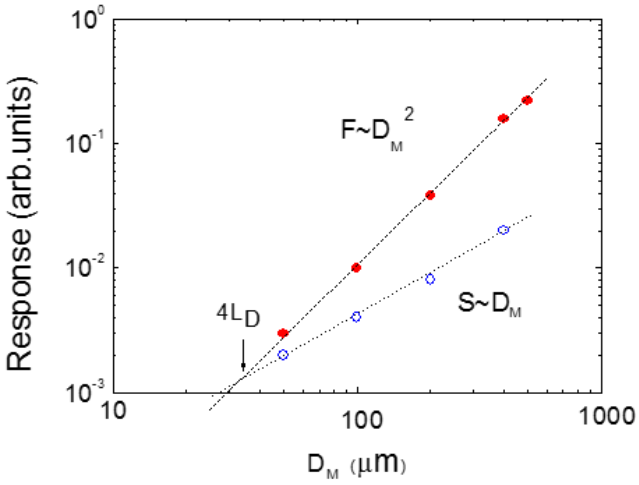

Figure 3.10. (a) The transient responses of the devices with different contact sizes (50x50, 200x200, and 500x500 μm^2) at T= 77 K at the bias voltage -0.4 V. F and S denote the fast and slow components of the response amplitude caused vertical and the lateral transport of by minority holes respectively. (b) The dependences of the amplitudes of the fast and slow components of the response on contact size DM.

The minority carrier lifetime was determined from the decay of the slow component of the response. Figure 4a shows the transient responses for the devices with the contact sides D_M= 50 and 200 μm. The analysis of the transient response was done solving the diffusion equation with generation of excess carrier over the

extended region in approximation $L_D >> W$, where W is the absorber thickness. The solution combined the decay of the minority carrier due to both diffusion of carriers from the extended area and carrier recombination [61]. The expression was similar to one obtained in Ref. 61. The number of carriers at the edge of the contact was found to be proportional to the following expression:

$$\int_0^{(D_W - D_M)/2} \frac{\exp(-t/\tau_{p0})}{\sqrt{4\pi D_p t}} \exp(-\frac{x_0^2}{4D_p t}) dx_0 = \exp(-t/\tau_{p0}) Erf((D_W - D_M)/2\sqrt{4D_p t}), \quad (3.4)$$

where τ_p and D_p are the lifetime and the diffusion coefficient of the minority carriers, and Erf is the error function. Fitting the data in Figure 3.11 with Eq (1) resulted in the time constant of 165 ns

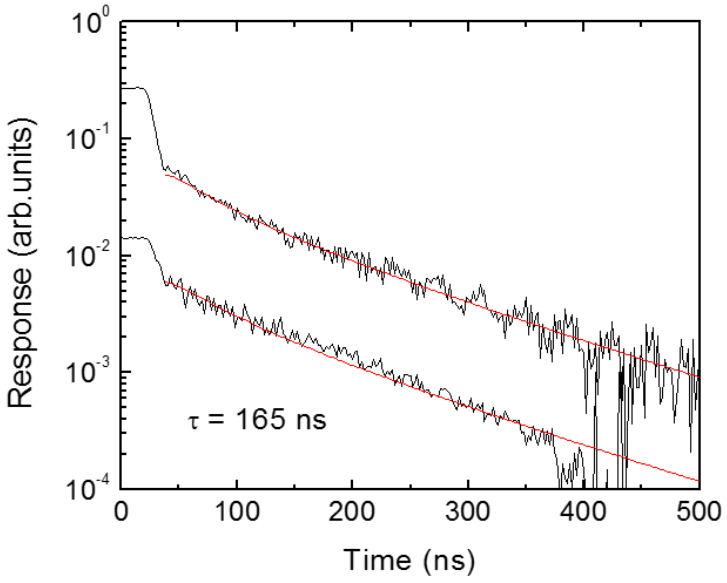

Figure 3.11. The transient responses for the devices with the contact sizes of DM= 50 and 200 um.

. Consequently, the mobility of minority holes at 77 K was calculated to be 800 cm2/Vs. The vertical transport time of minority holes by diffusion across the absorber with the thickness of 1 μm was estimated to be of 2 ns. Measurements of transient responses of the devices with different contact areas allowed determining

the minority hole diffusion length of 9 μm and the minority carrier lifetime of 165 ns. The proposed characterization method can be used for measurements of the minority carrier lifetime in anisotropic materials including strained layer superlattices.

3.6 Study on Auger Recombination in InAsSb alloys

In the section, the lifetime measurements were performed in similar materials with an extended range of Tellurium doping up to $4x10^{16}$ cm^{-3} to investigate the Auger recombination rate. The upper limit for the Auger-1 recombination (CHCC) for InAsSb with 40 % Sb composition at T = 77K was determined from the dependence of the minority carrier lifetime on the background concentration in the InAsSb device structures.

The heterostructures were grown on *n*-doped *GaSb* substrates by a solid-source molecular beam epitaxy (MBE). The layer sequence was as follows: a 3 μm thick compositionally graded $Ga_{1-x}In_xSb$ buffer, a 500 nm $Ga_{0.66}In_{0.34}Sb$ virtual substrate, a 1-μm-thick bulk $InAs_{0.6}Sb_{0.4}$ layer, a 200-nm-thick $Al_{0.6}In_{0.4}As_{0.1}Sb_{0.9}$ barrier, and a 200-nm-thick $InAs_{0.6}Sb_{0.4}$ top contact. The buffer, the virtual substrate and the top contact were doped with Tellurium to a level of $1x10^{18}$ cm^{-3}.. One sample was grown with undoped InAsSb absorber. Other 3 samples were grown with various levels of Te-doping of the absorber. undoped (~$1.5x10^{15}$ cm^{-3}), $1x10^{16}$ cm^{-3}, $2x10^{16}$ cm^{-3} and $4x10^{16}$ cm^{-3} n-doped respectively. The AlInAsSb barrier layers were undoped. The heterostructures were processed into epi-side and backside illuminated devices. Square-shaped contacts were etched into the barrier layer. The processing procedure was identical to that described in previous sections. The Quantum Efficiency (QE) measurement was done with Fourier Transform Infrared Spectroscope (FTIR), and with calibrated blackbody radiation source. Lifetime

measurement for different doping devices was done with transient response technique.

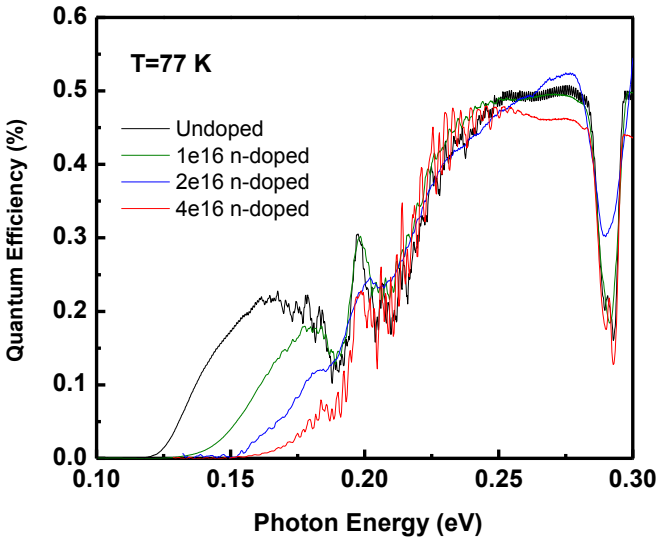

Figure 3.12. The photoresponse of samples with different doping, undoped (black), $1x10^{16}$ cm^{-3}(green), $2x10^{16}$ cm^{-3} (blue) and $4x10^{16}$ cm^{-3} (red), respectively.

Figure 3.12 shows the quantum efficiency results for four different doping devices at 77 K at V=-0.4 V. With doping increased, there is a strong Burstein-Moss shift from the absorption edge of undoped device. This may result from the small effective mass of electron in conduction band. According to [62] effective mass of electron at the bottom of conduction band is estimated to be 0.011 m_0 by cyclotron resonance measurement. It also indicates the efficient doping in active layers.

The dark current density-voltage characteristics at 77 K for undoped and doped devices are shown in Figure 3.13 (a). At V=-0.4 V, where QE started to saturate, the dark current density decreases from $1x10^{-3}$ A/cm^2 to $1.6x10^{-6}$ A/cm^2

(a)

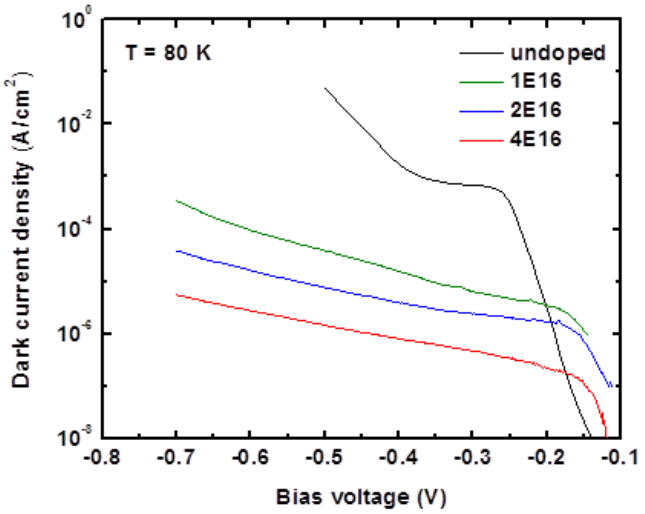

(b)

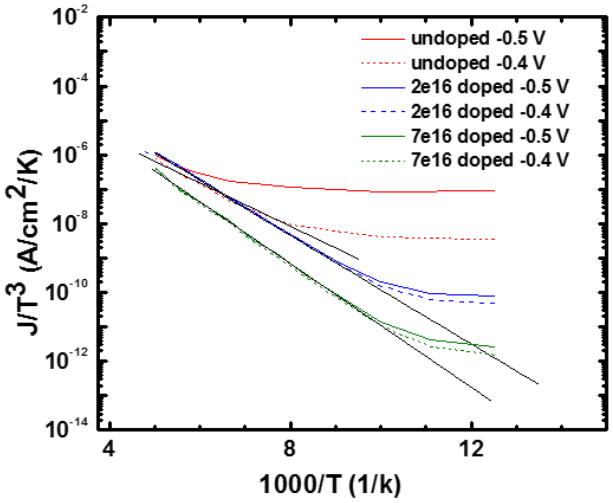

Figure 3.13. (a). Dark current density-voltage characteristics measured at 77 K for samples with different doping, undoped (black), $1x10^{16}$ cm^{-3}(green), $2x10^{16}$ cm^{-3} (blue) and $4x10^{16}$ cm^{-3} (red), respectively. (b). The temperature dependence of dark current density at different bias for samples with different doping. Red dot undoped at -0.4 V, blue dot $1x10^{16}$ cm^{-3} at -0.4 V, and green dot $4x10^{16}$ cm^{-3} at -0.4 V, respectively. Red solid undoped at -0.5 V, blue solid $1x10^{16}$ cm^{-3} at -0.5 V, and green solid $4x10^{16}$ cm^{-3} at -0.5 V, respectively.

with doping increased from undoped to $4x10^{16}$ cm^{-3}. As shown in previous section, the significant reduction of dark current in doped devices mainly results from suppression of depletion region in the active layer. The further reduction of dark current with increase of doping could be mainly attributed to decreased

concentration of minority holes. Meanwhile, since increase of doping causes Burstein-Moss shifts in QE measurements, the decrease of dark current may result from the decrease of intrinsic carrier concentration. [63] The temperature dependence of dark current density for the undoped and doped devices at bias -0.4 V and -0.5 V are shown in Figure 3.13 (b). The activation energy is determined from the slope in the temperature range 100-200 K. The activation energy is 126 meV, 153 meV and 177 meV for undoped, $1x10^{16}$ cm^{-3} and $4x10^{16}$ cm^{-3} doped devices, respectively. The increase of the activation energy in $1x10^{16}$ cm^{-3} doped devices is close to the values of Fermi level shifts (32 meV). The discrepancy for heavily doped devices ($4x10^{16}$ cm^{-3}) may come from the properties of band non-parabolicity, which is beyond the scope of this work. Different from undoped device, with increase of bias from -0.4 V to -0.5 V, the activation energy doesn't change in doped devices above 100 K. This could be explained by the fact that the dark current is diffusion dominant which is independent of applied bias. It also indicates that the doping in the active layer prevents depletion.

The effect of doping on the lifetime is investigated by transient response measurement. It should be noted that in the devices cooled to T =77 K the actual photocurrent was significantly greater than the dark current. This is due to exposure to both room temperature background illumination and the attenuated laser emission. In Figure 3.13 (a) the dots show the lifetime of 3 doped samples. The lifetime is 185 ns, 100 ns and 80 ns for 1e16, 2e16 and 4e16 doped devices, taking accounts of the lifetime of undoped devices reported (185 ns). The lifetime of materials could be expressed as: [64]

$$\frac{1}{\tau} = \frac{1}{\tau_{Auger}} + \frac{1}{\tau_{SRH}} \tag{3.5}$$

where τ_{SRH} is the Shockley-Read-Hall lifetime and τ_{Auger} is the Auger lifetime. The radiative lifetime contribution is not considered, due to the condition where carriers

are extracted from the devices and the radiative process may be suppressed. Results show that $InAsSb_{0.4}$ is SRH limited (185 ns) below doping level of 1e16. With increase of doping levels, the lifetime gradually dominated by Auger recombination. As we have demonstrated from result of QE and of dark current density dependence on temperature, Fermi level may ping well above the conduction band under high background doping. It may be in-accurate to express the Auger recomibination in quadratic terms of carrier concentration for the degenerate materials. Accroding to Ref. [65-66], the Auger recombination showed weaker dependence on doping in n-type degenerate HgCdTe. The reason comes from the fact that Auger recombination rate is closely related with threshold energy, which is a function of background doping in degenerate materials. Hence increase of doping will raise threshold energy, decreasing the Auger recombination rate. In our case, the recombination rate shows a weak dependence of lifetime on carrier concentration. As shown in Figure 3.14 (b), the dash line represents a linear dependence of carrier concentration. Therefore, assuming the doping doesn't change the SRH lifetime, we determine the Auger lifetime for the heavily doped (4e16 cm^{-3}) device to be 140 ns.

The dark currents of doped devices are diffusion dominated as discussed. Assuming the classical fitting for Auger recombination, the diffusion components of dark current could be expressed as: [64]

$$J_{diff} = \frac{qWn_i^2}{N\tau}, \tag{3.6}$$

where *W* is the active layer thickness.The Figure 3 (c) shows the experimental results of dark current density dependence on doping, at V=-0.4 V. ni is estimated to be 1.7x10^{13} cm^{-3} at 77 K. The estimation of intrinsic concentration is based on $n_i = \sqrt{N_v N_c}\exp(-\frac{E_g}{2kT})$, where N_v and N_c is the band edge density of state for valance band and conduction band respectively. For verification, the diffusion limited dark current density is calculated based on the lifetime measured for each device. Results

are shown as green dots in Figure 3.14 (c). It shows a good match for the most heavily doped device. The discrepancy between experimental results and calculated diffusion limited dark current in 1e16 and 2e16 cm^{-3} devices may be attributed to the residual depletion region at the interface, or the tunneling current. From lifetime and dark current measurement, we conclude a weak dependence of Auger recombination rate on the doping level in degenerate InAsSb. It also indicate a long intrinsic Auger lifetime for undoped structure.

(a)

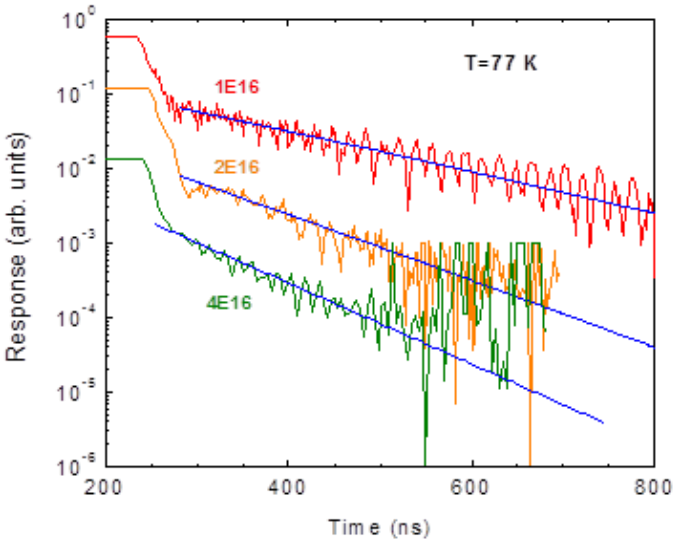

(b)

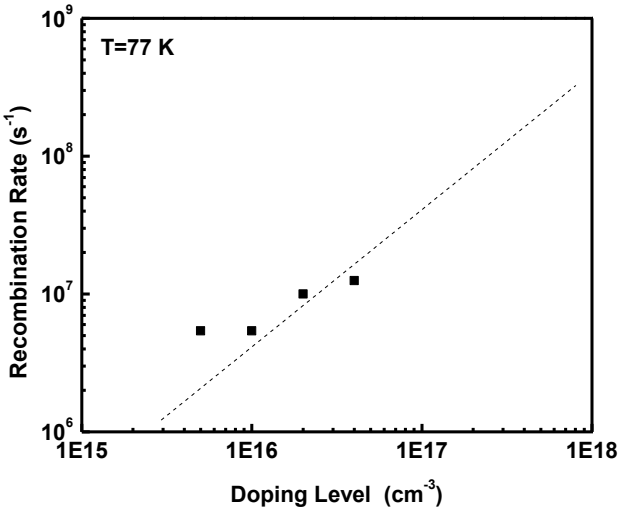

(c)

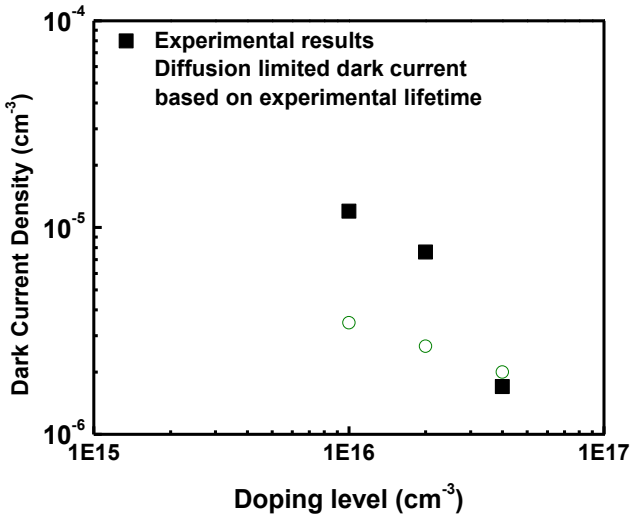

Figure 3.14 (a). Transient response of samples with different doping, $1x10^{16}$ cm^{-3}(red), $2x10^{16}$ cm^{-3} (yellow) and $4x10^{16}$ cm^{-3} (green). (b). Dependence of recombination rate on doping levels from experimental result (dot), dash line represents a linear dependence on carrier concentration(c). Dependence of dark current density on doping levels from experimental result (black dot), and calculation of diffusion limited dark current from experimental lifetime (green dot)

With small Auger recombination coefficient, high doping levels may be allowed for devices working at low temperature to reduce the concentration of minority hole carriers without penalty of dark current. Materials with high intrinsic Auger1 lifetime have advantage in higher temperature operations, where device performance is limited by the Auger lifetime. At 77K, lifetime of InAsSb is limited by SRH recombination as demonstrated. Compared with HgCdTe, lifetime is order magnitude smaller. [49] Although devices were doped to reduce the minority carrier concentration, cutoff wavelength suffers from Burstein Moss shift to shorter wavelength due to low effective mass of electrons (Figure 1a). However, with temperature increased, lifetime decreases and becomes limited by Auger recombination. The device with undoped absorber would benefit from relative smaller Auger recombination rate.

3.7 Frequency Response of barrier heterostructures

In order to test how fast the structure could response to intensity modulated signal, frequency response of the heterostructures were measured. The detail for the setup and measurement is introduced in Appendix III. The frequency responses of the epi-side illuminated devices (D_M=300 μm) and the back-side illuminated devices with D_M=500 μm are shown in Figure 3.7. Since the contact area was larger than the absorber area from which the carriers were drawn due to lateral diffusion and the window area was of the same size or smaller than the contact size, the fast component of the response dominated. The inset shows that the transient responses for both devices were identical. The devices with contact area of 500x500 μm^2, demonstrated -3 dB bandwidth of 27 MHz.. Figure 3.14 shows frequency responses for the epi-side and the back-side illuminated devices with the contact sizes of 300 and 500 μm, respectively. The devices were loaded with 50 Ohm. The inset shows transient responses for both devices dominated by the fast component of the response.

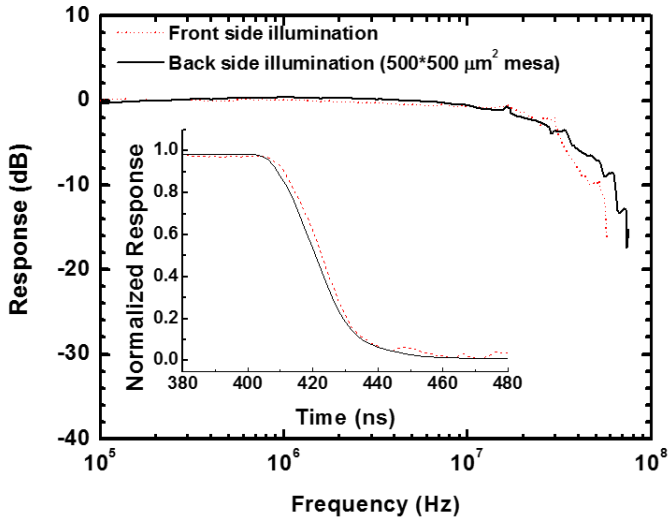

Figure 3.14. Frequency responses for the epi-side and the backside illuminated devices with contact lengths of 300 and 500 μm, respectively. The devices were loaded with a 50 Ohm input resistance of the preamplifier. The inset shows transient responses for both devices dominated by the fast component of the response.

For frequency response, since the structure is not optimized, the capacitor limiting the response could be reduced. For example, the area of the mesa sizes could be reduced so the contact capacitance could be smaller. On the other hand, the operation temperature could be elevated, so that the diffusion coefficient would be larger. As a consequence, the time constant could be reduced. In order to improve the frequency response, same structure with smaller mesa size was fabricated. The devices with the mesa contact width of DM =100 μm were illuminated from the epi-side through a window in the top metal with dimensions of 50*50 m^2. Since the windows were smaller than the dimensions of the mesa contacts, the response time was defined by the vertical hole transport time and the device time constants. A cut-off frequency of 50 MHz at a level of -3 dB was obtained. It was concluded that the cut-off frequency was limited by the time constant formed by a 63 pF capacitance of the device and input network and a 50 Ohm preamplifier input resistance.

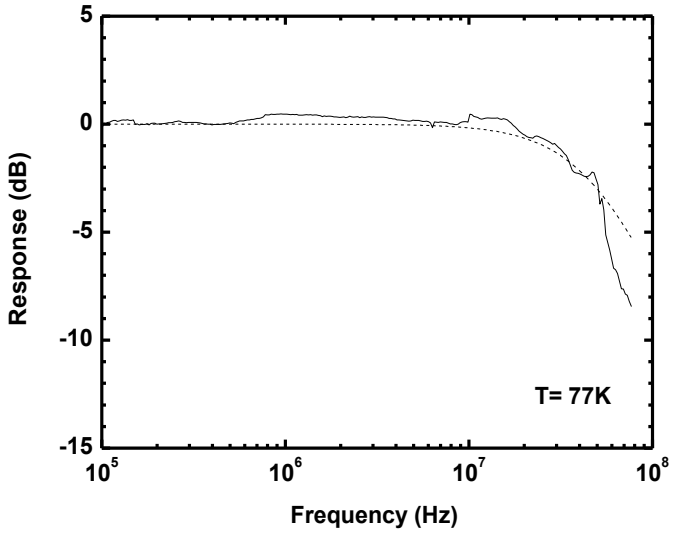

Figure 3.15 The frequency response of 100 um2 mesa (solid line). Dot line shows the approximation from 1st order low pass filter equation.

3.8 Summary

In summary, long-wave infrared nBn photodetectors with bulk, unrelaxed $InAs_{0.6}Sb_{0.4}$ absorbers and AlInAsSb barriers grown on compositionally graded GaInSb buffers on GaSb substrates were fabricated by molecular beam epitaxy and characterized. The heterostructures with 1-um-thick absorbers demonstrated external quantum efficiencies of 22% at 8 lm at a bias voltage of 0.4 V and temperatures of T=77K. From QE dependence on thickness we found out that，till 3 um, the QE of device was still limited by thickness. In terms of improving the QE, we could further increase the thickness of the active layers.

In optimization structure, the background limited performance has been demonstrated at operation temperature up to 100K in the devices with $1x10^{16}$ cm^{-3} doping. And from the study of Auger recombination in degenerate materials, it shows the Auger lifetime has weaker dependence on doping concentrations. Therefore, for low temperature operation, an appropriate level of n-type doping may be necessary to suppress the depletion region in the active layer. On the contrary, for elevated temperature operation, p-type doping is needed to compensate the high background concentration in the undoped structures. Meanwhile, through the characterization, it shows that InAsSb has a small Auger recombination rate, which will benefit high temperature operations.

In terms of the frequency response of detectors, we demonstrated the potential for fast detector based on InAsSb nBn structure. In order to further optimize the structure, in the first place, we need to have a detailed analysis of the capacitance in the device, for example C-V measurement, so that we can find out the limitation factors. We may try to decrease the mesa sizes so that the contact capacitance would decrease, which may result in fast response. Meanwhile, we may study the effect of thickness of barrier on the capacitance, since the thinner the barrier, the faster the

carrier may dissipate out of the device. On the hand, the increase of operation temperature would increase the bandwidth, on the sacrifice of larger dark current. So as discussed above, in order the increase the operation temperature, the active layer might be doped to balance dark current increasing.

Chapter 4

$InAsSb_x/InAsSb_y$ strained layer superlattices with ultra-thin periods

4.1 Introduction

In previous chapters it showed that utilizing the metamorphic buffer and virtual substrate allows fabricating bulk unstrained $InAsSb_x$ ($0<x<0.6$) with minimum band gap of 90 meV at T=77K . In this chapter it will demonstrate that the periodical variation of the Sb content in $InAsSb_x$ leads to the formation of controllable ordering of the layers with well-regulated band alignment. The diagram in Figure 4.1 shows that the energies of the conduction and the valence bands of InAsSb vary continuously with Sb composition displaying significant bowing of the band gap. Periodical variation of the Sb content in InAsSb leads to formation of controllable ordering of the layers. The modulation period is determined by the thicknesses of the strain compensated $InAsSb_x/InAsSb_y$ pairs grown on a virtual $GaIn_zSb$ substrate with a given lattice constant. The choice of the lattice parameter of the $GaIn_zSb$ virtual substrate, the compositions of $InAsSb_x/InAsSb_y$ layers as well as their thicknesses stipulates the effective band gap of the ordered alloy. In this paper a set of strain compensated $InAsSb_{0.31}/InAsSb_{0.61}$ layers were grown on $Ga_{0.59}In_{0.41}Sb$ virtual substrate to validate the correctness of the proposed approach.

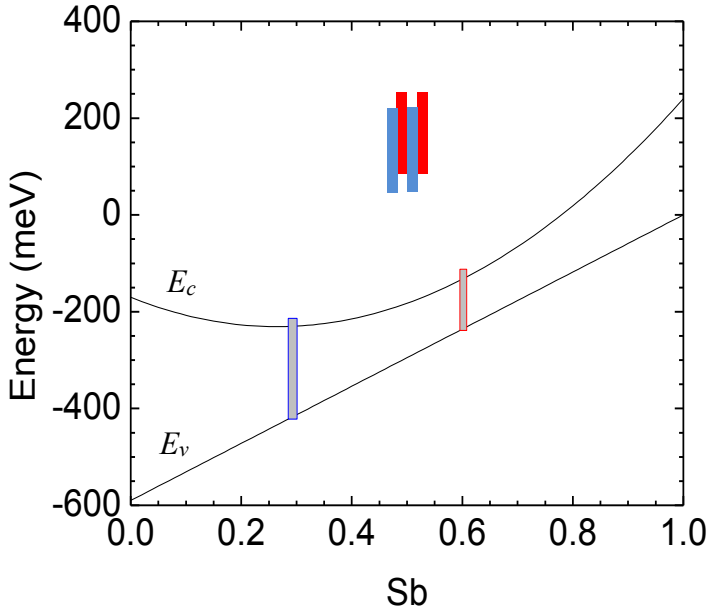

Figure. 4.1. The conduction Ec and valence Ev bands on Sb compositions for bulk InAsSb. Ev was taken to be -0.59 eV for InAs and 0.0 eV for InSb [3]. The bowing in the conduction band was taken to be C= 0.87 eV [2]. The valence band bowing was neglected. The inset shows the band alignments for $InAsSb_x/InAsSb_y$ structure.

High resolution x-ray diffraction (HRXRD) 004 omega-2theta scans contained features related to compositionally graded GaInSb buffer, constant composition GaInSb virtual substrate and to InAsSb layers with periodically modulated group V composition. The HRXRD from InAsSb demonstrated clearly distinguishable features of zero, first and, when measured in a wide enough angular range, second diffraction orders confirming the translational symmetry and allowing for experimental determination of the corresponding period in nm. At 20K and 77K all structures are characterized by photoluminescence within the spectra region 12-20 μm. The experiment showed that the variation of the modulation period from ~2.3 nm to ~5.5 nm leads to the shift of the maximum of 20 K photoluminescence from

12.4 μm to 19.6 μm. Thus the approach of developing strain compensated $InAsSb_x/InAsSb_y$ grown on a metamorphic virtual substrate allows developing narrow bandgap III-V materials with various bandgap energies.

4.2 XRD and PL characterization results

The structures were grown by solid-source molecular beam epitaxy on Te-doped GaSb substrates using the growth rate of about 1 μm/hour. The metamorphic GaInSb buffer had its group III elemental composition graded nearly linearly from GaSb to $Ga_{0.50}In_{0.50}Sb$ over the thickness of about 2.8 μm. This corresponds to a mismatch ramp of about 1.07 % per micron.

A high resolution x-ray diffraction (HRXRD) analysis (Figure 4.2) estimated the in-plane lattice parameter on top of the graded buffer to be ~ 2.5% bigger than that of GaSb. The $Ga_{0.59}In_{0.41}Sb$ layer (thickness ~ 500 nm) with matched lattice parameter served as a virtual substrate for subsequent heterostructure growth. Structures intended for photoluminescence studies were nominally undoped and contained 2 μm of a $InAsSb_{0.31}/InAsSb_{0.61}$ layer grown on top of the virtual substrate. For the photoconductivity spectrum measurements the structures contained an n-doped (Te, 10^{18} cm^{-3}) graded buffer and virtual substrate layers, a nominally undoped 1-μm-thick $InAsSb_{0.31}/InAsSb_{0.61}$ layer, a p-doped (Be,$10^{16}cm^{-3}$) AlGaInSb 200-nm-thick compositionally graded electron barrier and finally heavily p-doped $Ga_{0.59}In_{0.41}Sb$ contact layers. Each period of InAsSb contained two layers with nominal Sb fractions of 61 and 31 atomic percent corresponding to ~1% of the compressive and tensile strains relative to the virtual substrate. The modulation period ranged from ~2.3 to ~5.5 nm as determined by the HRXRD analysis from the separation of the higher order diffraction peaks in 004 omega-2theta scans. The strain balance between the layers was nearly perfect and the only slight adjustment of the layer thickness was performed (the $InAs_{0.39}Sb_{0.61}$ layer was made thicker by ~

1.5 monolayer than the $InAs_{0.59}Sb_{0.31}$ layer) to match the structure zero reflex in omega-2theta scan to that of virtual substrate (Fig. 4.2).

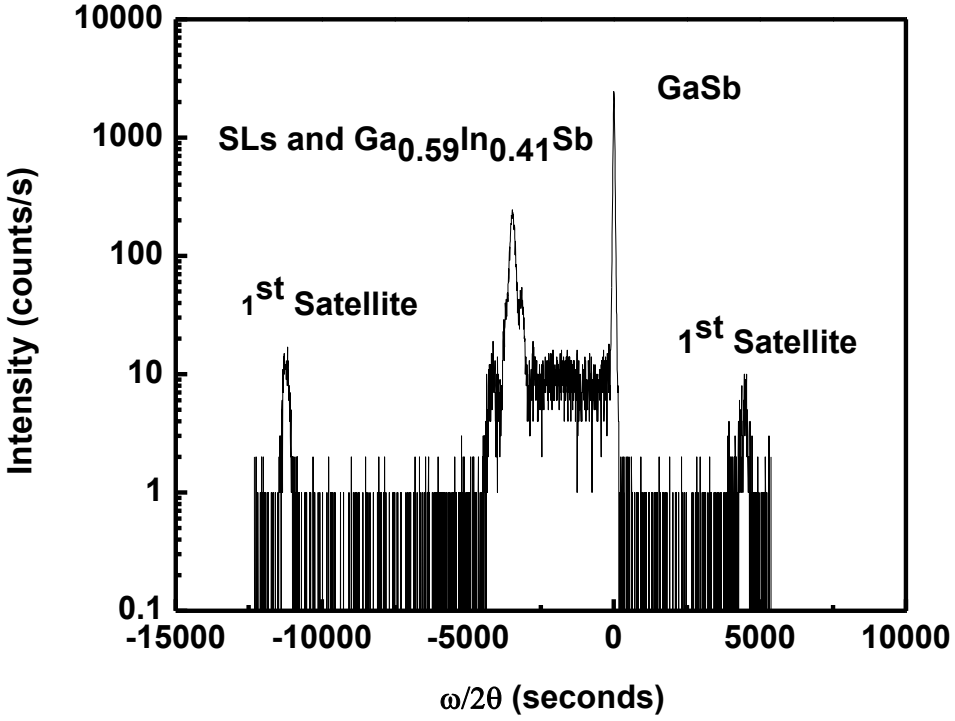

Figure 4.2. HRXRD spectrum of $InAsSb_x/InAsSb_y$ structure with the cell period of 2.33 nm.

The PL spectra of the epitaxial layers were measured with a Fourier-transform infrared (FTIR) spectrometer equipped with a HgCdTe detector with a 22 μm cut-off wavelength. The PL was excited by a 1064 nm solid-state laser with the power of 500 mW. The excitation area was 1.2×10^{-3} cm^2. Fig. 3 shows the normalized PL spectra of the heterostructures with different periods measured at T = 20 K. At this temperature the full width at half maxima of the PL peaks (FWHM) was under 20 meV which indicates good crystalline material quality. A greater FHWM value for

these materials compared to the previously reported FWHM 15 meV for similarly grown bulk $InAsSb_{0.4}$ alloys was observed.

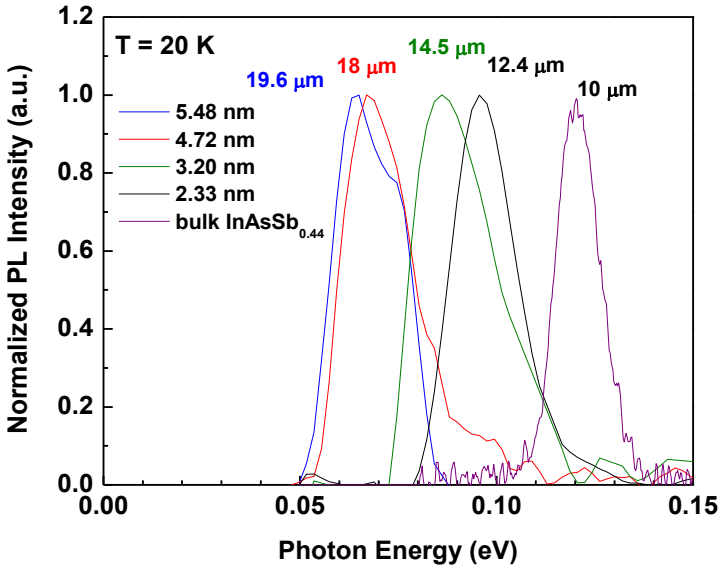

Figure 4.3. PL spectra in the ordered InAsSb alloys with the cell period in the range from 2.33 to 5.48 nm obtained at T =20 K.

The photoconductivity (PC) spectra (Fig. 4.4) were obtained at T =77 K with illumination from a glow bar source. The PL spectra from the same heterostructures at T= 77 K are shown for comparison. One can see matching the long-wavelength edges of the PL and PC spectra and increasing broadening of the PL spectra with temperature. The background carrier concentration in the materials can be assumed to be of n-type similar to that in undoped bulk InAsSb.

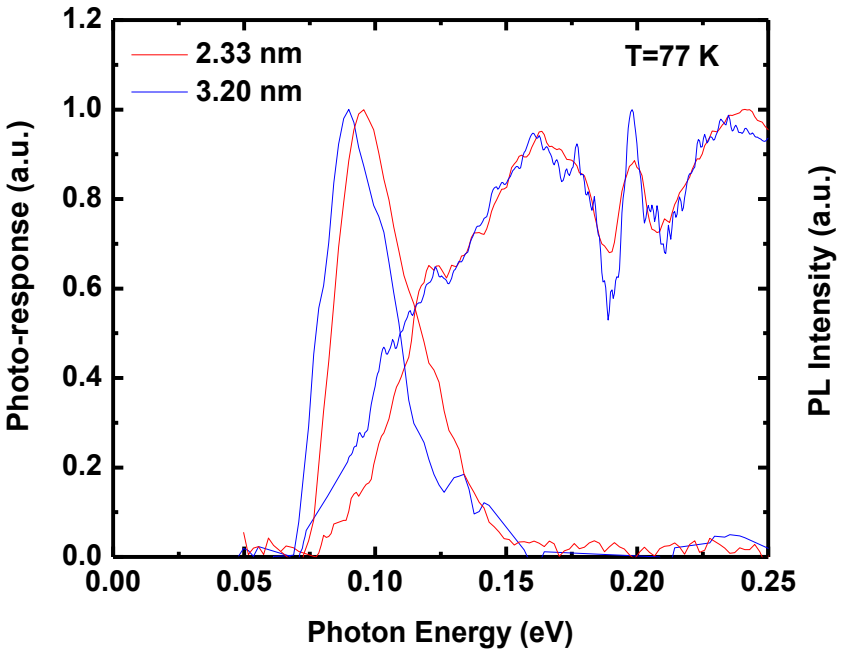

Figure 4.4. PL and photoconductivity spectra of the barrier heterostructure with a 2.3 nm and 3.2 nm period measured at T=77 K

As demonstrated in Chapter 2, the smallest energy gap (Eg) in bulk InAsSb alloys at low temperatures was found to be close to 0.1 eV (~12 μm). In this work we demonstrate that growing InAsSb alloys with enforced group V ordering leads to development of materials with Eg down to the value of 60 meV at low temperatures. Since the effective Eg of the modulated alloy is determined by the choice of the lattice parameter of $GaIn_zSb$, the compositions of $InAsSb_x/InAsSb_y$ layers and their thicknesses the data in Fig. 1 allows to anticipate the development of new modulated InAsSb alloys with a wide range of band gaps (60 meV < Eg < 100 meV). Utilization of thin (1-3 nm) layers of $InAsSb_{x,y}$ allows expecting that the value of the fundamental optical absorption in these alloys will be similar to bulk InAsSb and the hole transport will be unimpeded. These factors can be important for

development of detectors and light emitting diodes operating within the spectra region at 10 μm and above which is used for imaging as well as sensing applications [67]. The growth of Ga free InAs/ InAsSb superlattice (the best candidate today among III-V materials for the design of this type of devices) requires the utilization of thick layers of InAs [41].The latter suppresses the interband optical coefficient and impedes hole transport along the growth direction [68]. Thus we demonstrate that the periodical variation of the Sb content in $InAsSb_x$ leads to formation of controllable ordering of the InAsSb layers and allows developing a novel class of III-V materials with a band gap smaller than in bulk InAsSb. The obtained results open new prospects for development of optoelectronic devices on virtual substrates [69].

4.3 Fundamental absorption in $InAsSb_x/InAsSb_y$ SLs

Utilizing the virtual substrate, it enables to releases the constraint of lattice constant while designing the strain balanced structures. The transition energy and the miniband width of heavy holes for structures in previous sections are approximated by Kronig-Penny Model. Results are plotted in Figure 4.5. It shows the minband width of heavy holes decreases around 130 meV down to around 3 meV, when the period increases from 2.3 to 5.4 nm. It is known that the transport properties of superlattice are closely related to dispersion of mini-band of heavy holes. Compared with conventional InAs/GaSb of same energy gap, the ultrathin superlattice has a much wider miniband of heavy holes. We expect to benefit from the ultrathin superlattice in terms of bulk like absorption properties.

The absorption coefficients of the superlattice were determined from the transmission measurement at 77K. The effect of multiple reflections was taken into

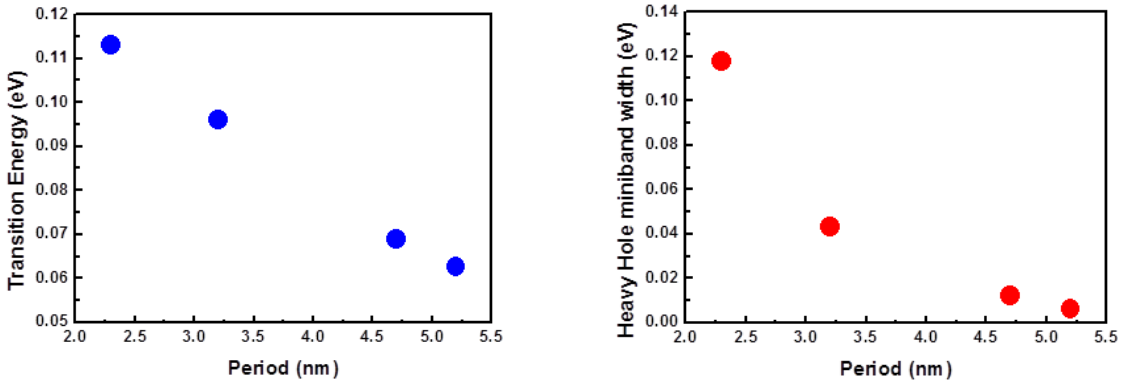

(a) (b)

Figure 4,5. (a) The energy gaps dependence on the period thickness. (b) Dependence of Miniband width of heavy holes on the period thickness based on the structures of $InAsSb_{0.3}/InAsSb_{0.6}$ grown on $GaIn_{0.4}Sb$ virtual substrate.

account. The absorption spectrum of superlattice with period 3.2 nm is shown in Figure 4.6. The absorption of bulk $InAsSb_{0.4}$ is also shown as reference. Meanwhile, the absorption properties were also investigated by 8 band kp method. [70] The absorption spectra obtained from calculation is also shown in Figure 4.6. Results show a good agreement between the experiment and calculation result in most of the spectral region. And it shows the evidence of extension of energy gap to longer wavelength in superlattice structures. In mid-wavelength region, the main difference between superlattice and bulk materials mainly comes from the difference in density of state. According to the calculation, the overlap between electrons and holes wavefunction in one period is 95%. The close-to-unity wavefunction overlap demonstrates the bulk-like properties of superlattice.

In order to further investigate the transport properties, quantum efficiency of the heterostructures with 1μm-thick active layer based on nBn scheme was measured. The sample was processed into a front illumination structure with fabrication procedures discussed in previous chapter. The quantum efficiency results of superlattice based structure and bulk based structure are shown in Figure 4.7. The

result matches that from absorption spectra. There is an extension of the absorption edge in superlattice structure. It shows demonstrates an efficient signal collection in the superlattice structure from QE result, which implies a good hole transport in the superlattice.

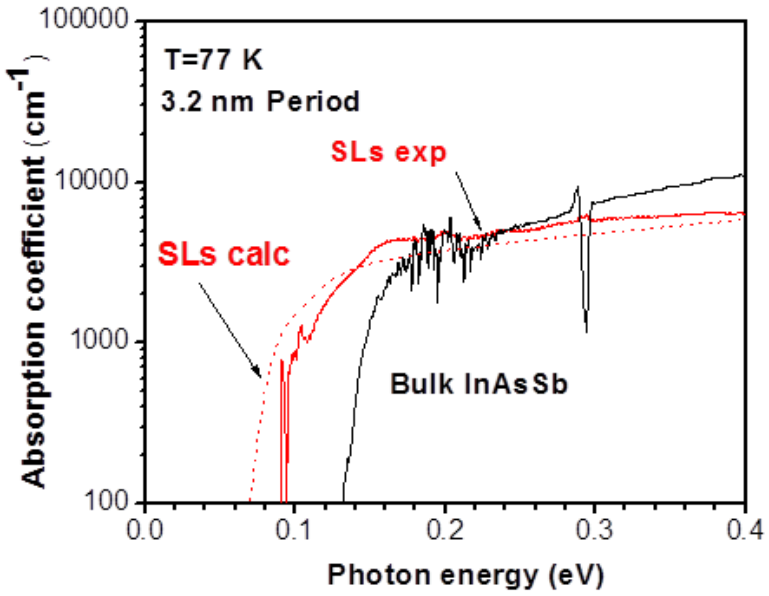

Figure 4.6. The absorption spectra of $InAsSb_{0.3}/InAsSb_{0.6}$ with period 3.2 nm obtained from experiment (red solid), calculation (red dot). The The absorption spectrum of bulk $InAsSb_{0.4}$ alloy (black solid).

The calculations and measurements show quite similar values of theabsorption coefficient in bulk InAsSb and HgCdTe on the one hand and the short-period $InAsSb_x/InAsSb_y$ SLs grown on metamorphic buffers on the other hand near the band edge of the LWIR absorber structures. This finding is expected based on the bulk-like value of the electron hole overlap (matrix element) in these structures and stands in stark contrast to the absorption coefficients in the SLs with large periods grown strain balanced on the GaSb substrate. Furthermore, the hole transport

characteristics are expected to be greatly improved in the short period SLs with very thin hole barriers.

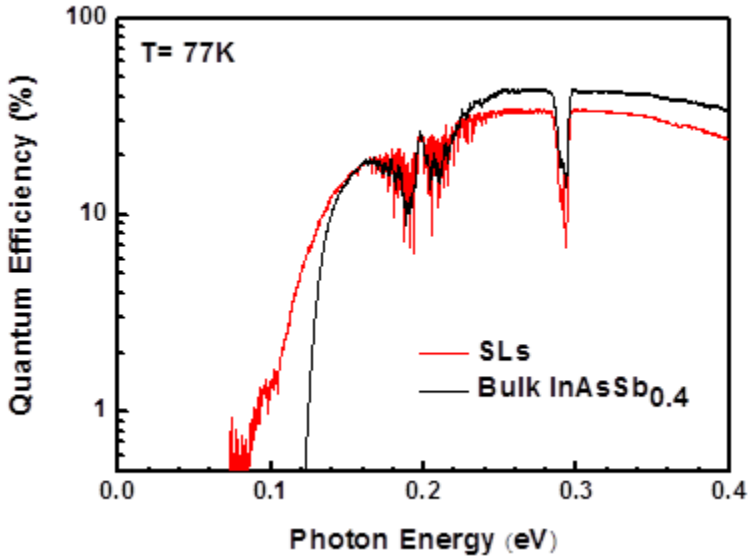

Figure 4.7. The quantum Efficiency spectra of heterostructures based on $InAsSb_{0.3}/InAsSb_{0.6}$ with the period of 3.2 nm (red), and bulk $InAsSb_{0.4}$ alloy

4.4 Summary

The new materials system, strain balanced ultrathin $InAsSb_x/InAsSb_y$ shows potential for the LWIR and VLWIR optoelectronic applications. This materials release the constraint from lattice constant, making it as a design parameter instead. It helps the optimization of the materials. Compared with conventional LWIR superlattice, the bulk like properties in the ultrathin superlattice is attractive and important in optoelectronic design. Further characterizations, such as lifetime, mobility, diffusion length measurements are needed to investigate the novel materials.

Summary of the most important results

In this work it was demonstrated that the bulk InAsSb materials free of group-V ordering grown on metamorphic buffers are capable of encompassing the long wave infrared range at low temperatures. The longest PL peak wavelength of group III-V alloys (12.4 μm) at 77 K was shown. Through optical measurement, bowing parameters, conduction and valence band positions were determined, which will be very useful for devices design. The characterization data obtained for un-optimized heterostructures suggests sufficiently large absorption and carrier lifetimes (long diffusion length) suitable for the development of infrared. The carrier transport, including the transport of minority holes, is adequate for the development of detectors and emitters with increased active layer thickness.

The InAsSb based nBn heterostructures were designed and fabricated. With optimizations, the background limited performance was demonstrated in photodetectors with cutoff wavelength 9.6 μm at 77K. It also shows the potential of InAsSb as an alternative material to replace HgCdTe. Using the transient response from photoconductivity spectra in time domain, the excess carriers lifetime and diffusion length of minority carriers were extracted.

In order to extend the energy gap into even longer wavelength, the ultrathin $InAsSb_x/InAsSb_y$ superlattice based on the virtual substrate technique were developed. Given the unique band alignment of InAsSb systems, it was demonstrated that the energy gap could be as narrow as 0.06 eV. The limitation for even narrower bandgap comes from measurement setup rather than materials design. The ultrathin superlattice also demonstrated bulk-like properties, which benefit LWIR and VLWIR optoelectronic devices, due to grater absorption and efficient

minority hole transport compared to those devices based on InAs/InAsSb SLS grown lattice matched to GaSb.

References

[1]. G. A. Sai-Halasz, R. Tsu, and L. Esaki, “A new semiconductor superlattice”. Appl. Phys. Lett. 30, 651 (1977).

[2]. R. Tsu and L. Esaki, “Tunneling in a finite superlattice”. Appl. Phys. Lett. 22, 562 (1973).

[3]. The transmission spectra was calculated with HITRAN2012 data base power by spectralcalc.com. The author has subscribed the usage of the plot.

[4]. J. Tersoff, “Dislocations and strain relief in compositionally graded layers”. Appl. Phys. Lett. 62, 693 (1993).

[5]. E. O. Kane, “Band Structure of Indium Antimonide”. J. Phys. Chem. Sol. 1, 82 (1956).

[6]. J. M. Luttinger, W. Kohn,” Motion of Electrons and Holes in Perturbed Periodic Fields”. Phys. Rev. 97, 869 (1955).

[7]. W. Kohn, L. J. Sham, "Self-Consistent Equations Including Exchange and Correlation Effects". Phys. Rev. 140, A1133 (1965).

[8]. C. Kittel, “Quantum Theory of Solids (Second Revised Printing ed.)”. New York, Wiley. ISBN 0-471-62412-8, (1986).

[9]. The band structures were calculated using open-source software nextnano, from www.nextnano.com.

[10]. W. A. Harrison, “Electronic structure and the properties of solids”. New York, DOVER PUBLICATIONS, INC. ISBN-13:978-0-486-66021-9, (1989).

[11]. C. Herring, “A new Method for Calculating Wave Functions in Crystals”. Phys. Rev. 57, 1169 (1940).

[12]. P. Y. Yu, M. Cardona, “Fundamentals of Semiconductors (Fourth Edition)”. New York, Springer, ISBN 1868-4513, (2010).

[13]. T. Miyakawa and D. L. Dexter, “Phonon Sidebands, Multiphonon Relaxation of Excited States, and Phonon-Assisted Energy Transfer between Ions in Solids”. Phys. Rev. B. 1, 2961 (1970).

[14]. L.C. Chiu, J.S. Smith, S. Margalit, A. Yariv, A.Y. Cho, "Application of internal photoemission from quantum-well and heterojunction superlattices to infrared photodetectors". Infrared Phys. 23, 93 (1983).

[15]. S. L. Chuang, "Physics of Optoelectronics, 2nd edition". New York, Wiley, ISBN: 978-0-470-29319-5, (2009).

[16]. L. C. West and S. J. Eglash, "First observation of an extremely large - dipole infrared transition within the conduction band of a GaAs quantum well". Appl. Phys. Lett. 46, 1156 (1985).

[17]. C. Chang, Y. D. Sharma, Y. Kim, J. A. Bur, R. V. Shenoi, S. Krishna, D. Huang and S. Lin, "A Surface Plasmon Enhanced Infrared Photodetector Based on InAs Quantum Dots" . Nano Lett. 10, 1704 (2010).

[18]. B. F. Levine, "Quantum Well Infrared Detector". J. Appl. Phys. 74, R1, (1993).

[19]. J. Faist, F. Capasso, D. L. Sivco, C. Sirtori, A. L. Hutchinson, A. Y. Cho, "Quantum cascade laser", Science 264, 553 (1994).

[20]. C. H. Grein, M. E. Flatté, J. T. Olesberg, S. A. Anson, L. Zhang and T. F. Boggess, "Auger recombination in narrow-gap semiconductor superlattices incorporating antimony". J. Appl. Phys. 92, 7311 (2002).

[21]. C. Waschke, H. G. Roskos, R. Schwedler, K. Leo, H. Kurz, and K. Köhler, "Coherent submillimeter-wave emission from Bloch oscillations in a semiconductor superlattice". Phys. Rev. Lett. 70, 3319 (1993).

[22]. L. C. L. Y. Voon, M. Willatzen, "The kp Method". New York, Springer, ISBN 978-3-642-10090-1, (2010).

[23]. Y. Livneh, P. C. Klipstein, O. Klin, N. Snapi, S. Grossman, A. Glozman, and E. Weiss, "k·p model for the energy dispersions and absorption spectra of InAs/GaSb type-II superlattices". Phys. Rev. B. 86, 235311 (2012).

[24]. B.Nguyen, D. Hoffman, Y. Wei, P. Delaunay, A. Hood and M. Razeghi, "Very high quantum efficiency in type-II InAs/GaSbInAs/GaSb superlattice photodiode with cutoff of 12 μ m". Appl. Phys. Lett. 90, 231108 (2007).

[23]. Osbourn G. C.," InAsSb strained - layer superlattices for long wavelength detector applications". J. Vac. Sci. Technol. B, 2, 176 (1984).

[24]. Lee G. S., Lo Y., Lin Y. F., Bedair S. M., and Laidig W. D., “Growth of InAs1−x Sb x (0<x<1) and InSb - InAsSb superlattices by molecular beam epitaxy”. Appl. Phys. Lett., 47, 1219 (1985).

[25].Yen M. Y., People R., Wecht K. W., and Cho A. Y., “Long - wavelength photoluminescence of InAs1−x Sb x (0<x<1) grown by molecular beam epitaxy on (100) InAs”. Appl. Phys. Lett., 52, 489 (1988).

[26].Yen M. Y., People R., and Wecht K. W., J. Appl. Phys., 64, 952 (1988).

[27]. Tsukamoto S., Bhattacharya P., Chen Y. C., and Kim J. H., “Transport properties of InAs x Sb1−x (0≤x≤0.55) on InP grown by molecular - beam epitaxy”. J. Appl. Phys., 67, 6819 (1990).

[28]. Bethea C. G., Levine B. F., Yen M. Y., Cho A. Y., “Photoconductance measurements on InAs0.22Sb0.78/GaAs grown using molecular beam epitaxy”. Appl. Phys. Lett., 53, 291 (1988).

[29]. Yen M. Y., Levine B. F., Bethea C. G., Choi K. K., and Cho A. Y., “Molecular beam epitaxial growth and optical properties of InAs1−x Sb x in 8–12 μm wavelength range”. Appl. Phys. Lett., 50, 927 (1987).

[30].Fang Z. M., Ma K. Y., Jaw D. H., Cohen R. M., and Stringfellow G. B., “Photoluminescence of InSb, InAs, and InAsSb grown by organometallic vapor phase epitaxy”. J. Appl. Phys., 67, 7034 (1990).

[31]. Zhang Y.-H., Lew A., Yu E., Chen Y., “Microstructural properties of Full-size image (<1 K) superlattices and InAsxSb1 − x ordered alloys grown by modulated molecular beam epitaxy”. J. Crystal Growth, 175/176, 833 (1997).

[32]. Besikci C., Ozer S., Van Hoof C., Zimmermann L., John J., and Merken, P., "Characteristics of InAs0.8Sb0.2 photodetectors on GaAs substrates". Semicond. Sci. Technol., 16, 992 (2001).

[33] L. R. Dawson, "Summary Abstract: Molecular beam epitaxial growth of InAsSb alloys and superlattices". J. Vac. Sci. Techn. B, 4(2), 598 (1986).

[34] S. R. Kurtz, G. C. Osbourn, R. M. Biefeld, L. R. Dawson, and H. J. Stein, "Extended infrared response of InAsSb strained‐layer superlattices". Appl. Phys. Lett. 52, 831 (1988)

[35] H. R. Jen, K. Y. Ma, and G. B. Stringfellow, "Long‐range order in InAsSb". Appl. Phys. Lett., 54, 1154 (1989).

[36]. 7. S. R. Kurtz, L. R. Dawson, R. M. Biefeld, D. M. Follstaedt, and B. L. Doyle, "Ordering-induced band-gap reduction in InAs1−xSbx (x≅0.4) alloys and superlattices". Phys. Rev. B, 46, 1909 (1992).

[37]. I. Vurgaftman, J. R. Meyer and L. R. Ram-Mohan, "Band parameters for III–V compound semiconductors and their alloys". J. Appl. Phys. 89, 5815 (2001).

[38]. H. B. Bebb and E. W. Williams, in Semiconductors and Semimetals, edited by R. K. Willardson and A. C. Beer (Academic, New York, London,1972), Vol. 8, Ch. 4, p. 238.

[39]. A. T. Hunter and T. C. McGill, "Luminescence from HgCdTe alloys". J. Appl. Phys., 52, 5779 (1982).

[40]. Y. P. Varshni, "Temperature dependence of the energy gap in semiconductors". Physica. 34, 149 (1967).

[41]. E. H. Steenbergen, Y. Huang, J.H. Ryou, R. D. Dupuis, K. Nunna, D. L. Huffaker, and Y.-H. Zhang., Optical Properties of Strainbalanced InAs/InAs1-xSbx Type-II Superlattices, AIP Conf. Proc. 1416, 122 (2011).

[42]. S.-H. Wei and A. Zunger, Phys. Rev. B. 52, 12039 (1995).

[43]. D. Lackner, O. J. Pitts, M. Steger, A. Yang, M. L. W. Thewalt and S. P. Watkins, Appl. Phys. Lett. 95, 081906 (2009).

[44]. P.-W. Liu, G. Tsai, H. H. Lin, A. Krier, Q. D. Zhuang, and M. Stone, Appl. Phys. Lett. 89, 201115 (2006).

[45]. B. V. Olson, E. A. Shaner, J. K. Kim, J. F. Klem, S. D. Hawkins, L. M. Murray, J. P. Prineas, M. E. Flatt，and T. F. Boggess, Time-resolved optical measurements of minority carrier recombination in a mid-wave infrared InAsSb alloy and InAs/InAsSb superlattice, Appl. Phys. Lett., 101, 092109 (2012).

[46]. E. H. Steenbergen, B. C. Connelly, G. D. Metcalfe, H. Shen, M. Wraback, D. Lubyshev,, Y. Qiu, J. M. Fastenau, A. W. K. Liu, S. Elhamri, O. O. Cellek, and Y.-H. Zhang. Significantly improved minority carrier lifetime observed in a longwavelength infrared III-V type-II superlattice comprised of InAs/InAsSb, Appl. Phys. Lett., 99, 251110 (2011).

[47]. H. S. Kim, O. O. Cellek, Z. Lin, Z. He, X. Zhao, S. Liu, H. Li, and Y Zhang, “Long-wave infrared nBn photodetectors based on InAs/InAsSb type-II superlattices”. Appl. Phys. Lett., 101, 161114 (2012).

[48]. D. Donetsky, S. P. Svensson, L. E. Vorobjev, G. Belenky, Carrier lifetime measurements in short-period InAs/GaSb Strained Layer Superlattice Structures, Appl. Phys. Lett., 95, 212104 (2009).

[49]. A Rogalski, “HgCdTe infrared detector material: history, status and outlook”. Rep. Prog. Phys. 68, 2267 (2005).

[50]. Y. Wei, A. Gin, M. Razeghi and G. J. Brown, “Advanced InAs/GaSb superlattice photovoltaic detectors for very long wavelength infrared applications”. Appl. Phys. Lett. 80, 3262 (2002).

[51]. D. Donetsky, G. Belenky, S. Svensson, S. Suchalkin, "Minority carrier lifetime in type-2 InAs–GaSb strained-layer superlattices and bulk HgCdTe materials". Appl. Phys. Lett. 97, 052108 (2010).

[52]. S. Maimon and G. W. Wicks, "nBn detector, an infrared detector with reduced dark current and higher operating temperature", Appl. Phys. Lett., 89, 151109 (2006).

[53]. P. C. Klipstein, "xBn barrier photodetectors for high sensitivity and high operating temperature infrared sensors", Infrared Technology and Applications, XXXIV, ed. by B. J. Andresen, G. F. Fulop, P. R. Norton, Proc. of SPIE, 6940, 694002U (2008).

[54]. G. Belenky, D. Donetsky, G. Kipshidze, D. Wang, L. Shterengas, W. L. Sarney, and S. P. Svensson, "Properties of unrelaxed InAs1−XSbX alloys grown on compositionally graded buffers". Appl. Phys. Lett. 99, 141116 (2011).

[55]. D. Wang, D. Donetsky, G. Kipshidze, Y. Lin, L. Shterengas, G. Belenky, W. L. Sarney, S. P. Svensson, "Metamorphic InAsSb-based barrier photodetectors for the long wave infrared region", Appl. Phys. Lett., 103, 051120 (2013).

[56]. G. Belenky, D. Wang, Y. Lin, D. Donetsky, G. Kipshidze, L. Shterengas, D. Westerfeld, W. L. Sarney, S. P. Svensson, "Metamorphic InAsSb/AlInAsSb heterostructures for optoelectronic applications". Appl. Phys. Lett. 102, 111108 (2013).

[57]. Simon M. Sze, Kwok K. Ng, "Physics of Semiconductor Devices, 3rd edition". Wiley, New York, ISBN-13: 9780471143239, (2006).

[58]. W. Shockley and W. T. Read, Jr., "Statistics of the Recombinations of Holes and Electrons". Phys. Rev. 87, 835 (1952).

[59]. S. P. Svensson, F. Crowne, H. Hier, W. L. Sarney, W. Beck, Y. Lin, D. Donetski, S. Suchalkin, G.; Belenky, "Background and Interface Electron Populations in InAs0.58Sb0.42", Semic. Sci. and Technol. 30, 035018 (2015).

[60]. A. Rogalski, "Infrared Detectors, 2nd edition". Taylor & Francis, Boca Raton (2010).

[61]. J. S. Schaffner and J. J. Suran, "Transient Response of the Grounded Base Transistor Amplifier with Small Load Impedance". J. Appl. Phys. 24, 1355 (1953).

[62]. S. Suchalkin, J. Ludwig, G. Belenky, B. Laikhtman, G. Kipshidze1, Y. Lin, L. Shterengas, D. Smirnov, S. Luryi, W. L. Sarney, "Electronic properties of unstrained

unrelaxed narrow gap InAs x Sb1−x alloys", J. Phys. D: Appl. Phys. 49 105101 (2016).

[63]. Philip Klipstein, "Depletion-less photodiode with suppressed dark current and method for producing the same". US patent 20100295095 A1, issued 2010.

[64]. M. A. Kinch, F. Aqariden, D. Chandra, P-K Liao, H. F. Schaake, H. D. Shih, "Minority carrier lifetime in p-HgCdTe", J. Electron. Mater., 34, 880 (2005).

[65]. T, N, Casselman, "Calculation of the Auger lifetime in degenerate n-type HgCdTe". Physics of Narrow Gap Semiconductors, 152, 147 (1982).

[66]. T.N. Casselman, P.E. Petersen, "Calculation of the carrier concentration dependence of the Auger lifetime in degenerate n-type (Hg, Cd)Te". Solid State Comm., 39, 1117 (1981).

[67]. A Rogalski, J Antoszewski, L Faraone, 'Third-generation infrared photodetector arrays'. J. Appl. Phys., 105, 091101 (2009).

[68]. P. Klipstein, Y. Livneh, A. Glozman, S. Grossman, O.Klin, N. Snapi, E. Weiss, 'Modeling InAs/GaSb and InAs/InAsSb superlattice infrared detectors'. J. of Electron. Mater., 43, 2984 (2014).

[69]. G.Belenky, L. Shterengas, D. Westerfeld, 'Compound semiconductor device on virtual substrate', US patent 9065000, issued 2015.

[70]. I. Vurgaftman, G. Belenky,Y. Lin, D. Donetsky, L. Shterengas, G. Kipshidze, W. L. Sarney and S.P. Svensson, "Interband absorption strength in long-wave infrared type-II superlattices with small and large superlattice periods". Appl. Phys. Lett. (2016). *submitted*

Appendix I

Photoluminescence measurement

The photoluminescence measurement is based on reflective optics. The photoluminescence of sample under test is excited by Nd:YAG solid state laser (1064 nm). The photons are collected by the reflective objective lens (1 inch focus length). The schematic setup is shown below in Figure A1.1. Alignment is required to overlap the focus point of lens, laser spot and sample position. It is worthy to

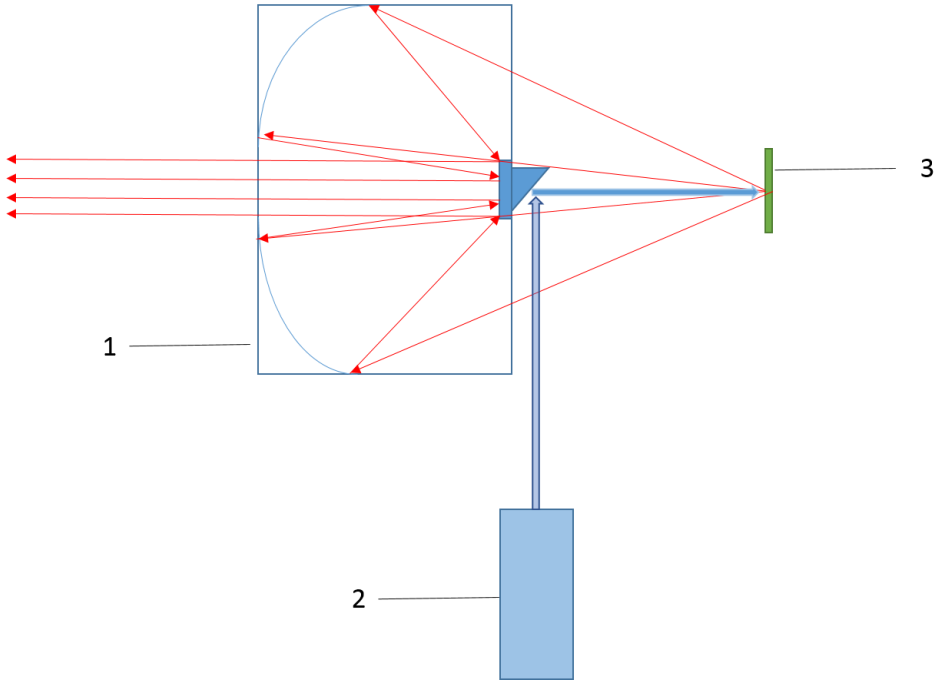

Figure A1.1. The schematic setup for photon collection system in PL measurements. 1. The reflective objective lens with a prism. 2. The Nd:YAG solid state laser (1064 nm). 3. Sample under test.

note that for measurement below room temperature cryostat should be used. The sample is mounted on Cu block attached to cold finger in the cryostat. Depending on the wavelength of PL, different types of window should be used. The transmission spectra of different windows used in our lab could be found on Janis website. The KRS5 window is toxic, care must be taken while using it.

The collected photons were sent to FTIR (Nicolet 670) for signal processing. Depending on PL wavelength, different detectors are selected. The Nicolet 670 is capable of using external photodetectors. Usually, the continuous scanning mode is enough for most of mid-wavelength infrared emitting sample. For wavelength longer

than 7 μm, the step-scan mode scanning mode is required due to thermal background radiation noise. The step-scan mode scanning is working with the standard lock-in technique. The flow chart of setup is shown in figure A1.2.

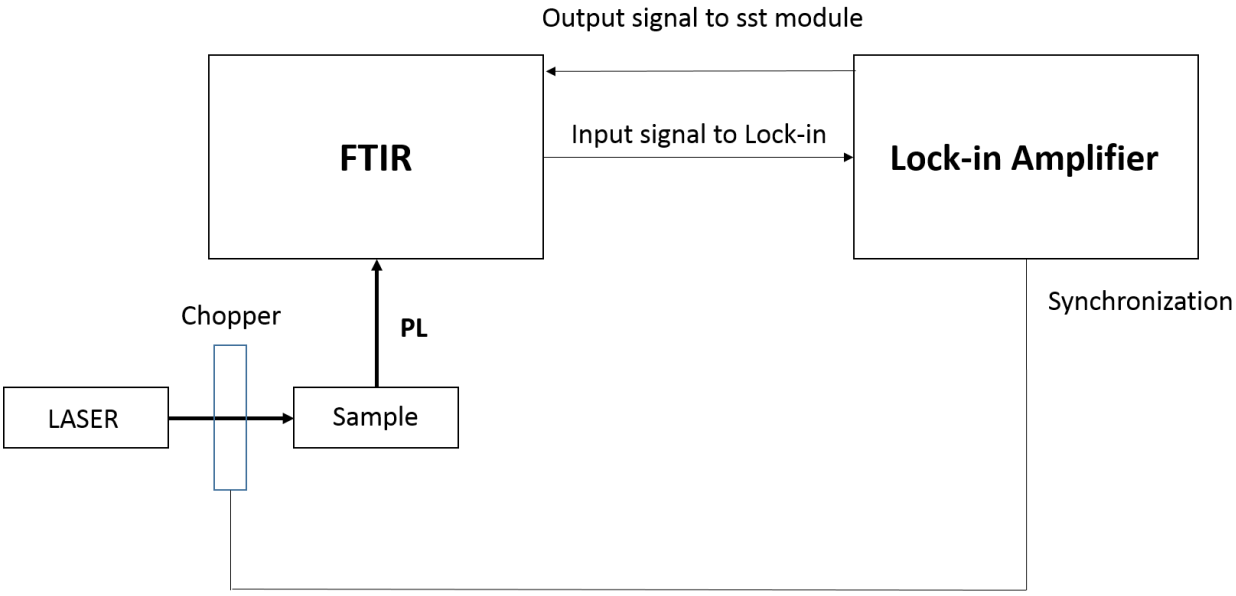

Figure A1.2. The flow chart of PL measurement using FTIR operating in the step-scan mode

The photon signal is modulated by mechanical chopper (~1 kHz), and synchronized with lock-in amplifier. And lock-in amplifier sends back the amplified signal to FTIR. The step scan provides a much higher sensitivity compared with continuous scan. It can detect small signal in the level of hundreds of nW based on the system in our lab.

Appendix II

Quantum Efficiency measurement

The quantum efficiency (QE) is an important parameter in characterizing the absorption and transport properties of photodetector or related heterostructures. Determination of QE consists of 2 measurements, namely photo-response measurement, and responsivity measurement. The photo-response measurement is setup is shown in Figure A2.1

Figure A2.1. The flow chart of the setup for photo-response measurement.

The device under test is used as an external detector of the FTIR. Since the goal of photo-response measurement is to obtain the response spectrum of heterostructure, a well-calibrated blackbody radiation source is required. In this measurement, the Boston Electronics IR blackbody source is used. The photocurrent generated from light in a spectral range from hv to hv +dhv is:

$$dI = S(hv) * R(hv) * dhv \quad \text{A2.1}$$

where S(hv) is the blackbody radiation spectra depicted by Plank equation, and R is the responsivity spectrum which is unknown. From the photo-response measurement, the normalized responsivity spectrum could be obtained as shown in Figure A2.2.Using blackbody as a light source, the total current can be expressed as:

$$I = P * R_0 \int S_N(hv) * R_{N1}(hv) * dhv \quad \text{A2.2}$$

where P is total power incident on surface of detector, R_0 is peak value of responsivity spectrum, S_n is normalized spectrum of blackbody radiation to the whole spectrum range, and R_{N1} is the normalized responsivity spectrum to the peak value. The normalized responsivity spectrum R_{N1} could be determined from the

photo-response measurement. If the incident power and corresponding photo-current are known, the peak value of responsivity could be calculated according to Eq. (A2.2). The responsivity spectrum could be determined to be:

$$R(hv) = R_0 * R_{N1}(hv), \quad \text{A2.3}$$

Therefore, the quantum efficiency could be determined as:

$$QE(hv) = hv * R(hv), \quad \text{A2.4}$$

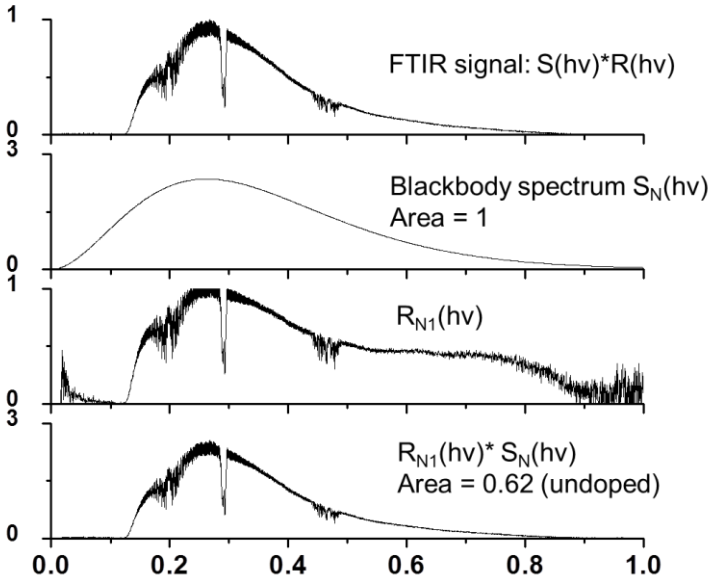

Figure A2.2. The data processing procedures to determine quantum efficiency.

The responsivity measurement is required to determine the relationship between incident power and corresponding photo-current. The measurement setup is shown in Figure A3.2.

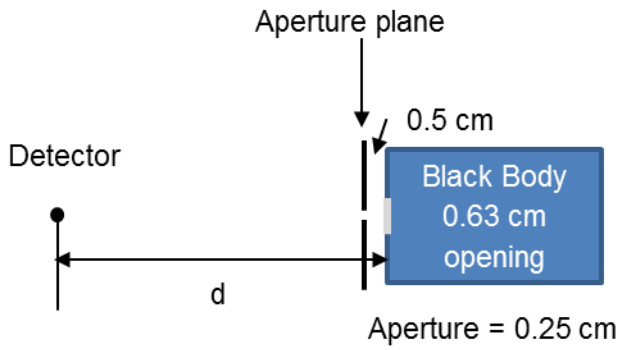

Figure A2.3 The schematic setup for responsivity measurement

In Figure A3.2, the detector receives photons from the blackbody radiation which should operate at the same temperature as it does in photo-response measurement. The photocurrent is amplified and read by scope. The power incident on detector window is estimated by geometric factors listed in Figure A2.3, and it could be estimated as:

$$P_{bb} = \varepsilon\sigma A\left(T^4 - {T_0}^4\right), \qquad \text{A2.5}$$

$$P = T_{cryostat\,window} * P_{bb} * \frac{A_D}{\pi d^2},$$

where P_{bb} is the power from radiation source of area A at temperature T, σ is Stefan coefficient, ε is emissivity which is 1 for blackbody, T_0 is room temperature 300K, $T_{cryostat}$ is the transmission coefficient of cryostat window, A_d is the area of detector,

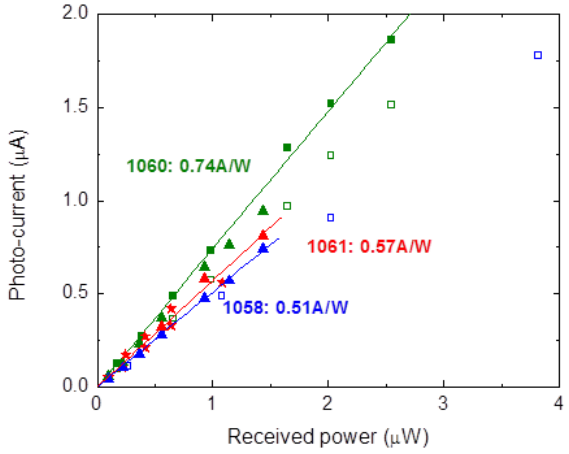

Figure A2.4. The power-photocurrent relationship in responsivity measurement

and d is the distance between detector and blackbody source. Since the approximation is based on the spherical wave estimation, it is only valid when distance is much larger compared with the aperture. In order to have an accurate estimation of responsivity, distance between them is changed to average the measurement error. An example of power-photocurrent relationship is shown in Figure A2.3. It shows a linear relationship between photocurrent and power which is consistent with Eq. A2.2. From the slope the peak value of responsivity could be determined.

Appendix III

The frequency response measurement

The schematic setup of frequency response measurement is shown in Figure A3.1. It consists of two parts, namely the emitter and the detector. The diode laser is working on continuous wave mode above threshold, modulated by small ac signal. The ac and dc electrical part is connected by bias T. The detector is mounted in Dewar cooled down to 77 K. The photo-current signal is amplified by pre-amplifier. The amplified signal is then sent to lock-in amplifier, which is synchronized with modulated frequency. Eventually, the data is recorded by LABVIEW program.

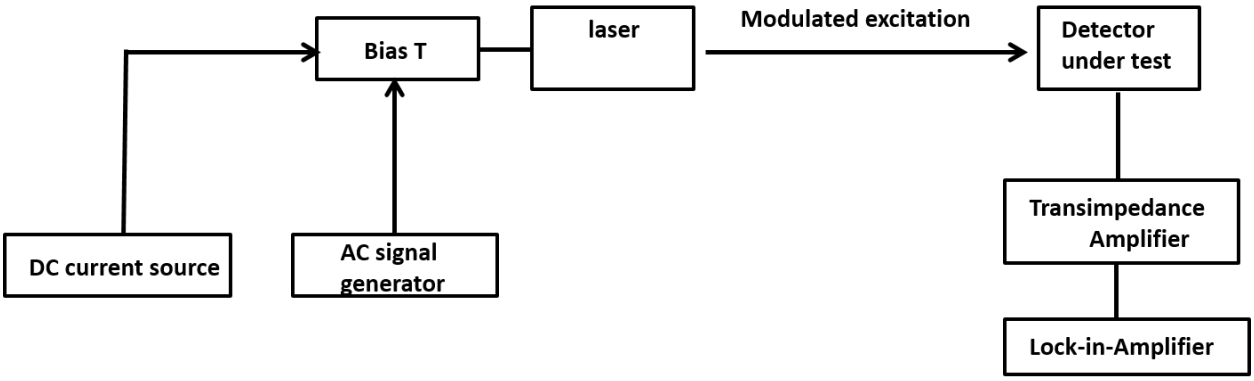

Figure A3.1. The flow chart of the setup for frequency response measurement.

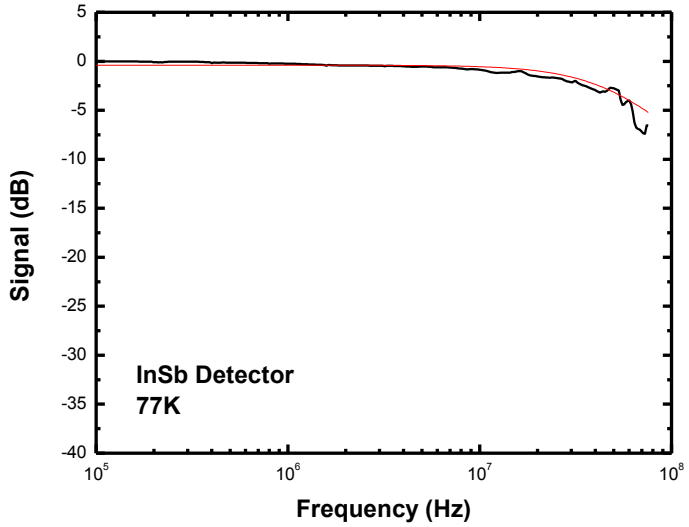

Figure A3.2. The frequency response of InSb detector at 77 K used as a reference.

In order to verify the system is fast enough to characterize the frequency response of detectors, frequency response of fast InSb detector is used to calibrate the system. The transport time of InSb is less than 2 ns, corresponding to -3dB cutoff frequency larger than 50 MHz. Figure A3.2 shows an example of frequency response of InSb detector. It shows a -3dB cutoff frequency around 55 MHz. It matches the data provided by manufacturer. As it shown in Figure A3.2, the experimental result is fitted with 1^{st} order RC equation, it shows the same bandwidth of 55 MHz.